

**Investigation and Development of Ferrofluid Enabled Micro-Electro-Mechanical
Systems**

by

Babak Assadsangabi

B.Sc., Shiraz University, Iran, 2006

M.A.Sc., Shiraz University, Iran, 2009

A THESIS SUBMITTED IN PARTIAL FULFILLMENT OF
THE REQUIREMENTS FOR THE DEGREE OF

DOCTOR OF PHILOSOPHY

in

THE FACULTY OF GRADUATE AND POSTDOCTORAL STUDIES
(Electrical and Computer Engineering)

THE UNIVERSITY OF BRITISH COLUMBIA

(Vancouver)

September 2014

© Babak Assadsangabi, 2014

Abstract

Ferrofluids are magnetic fluids that can be manipulated using magnetic field. Ferrofluids have unique properties that have led to various interesting applications. Although, currently they are being used in few commercial products in macro-scale domain, there has been limited success in their applications in micro- devices and microactuators in specific.

Literature review shows various efforts to develop ferrofluid-based microactuators however, most of them have utilized non-integrated means (e.g. external magnets or solenoids) to provide the necessary magnetic field for ferrofluid manipulation that inherently limit their application as a micro-device. Moreover, previous ferrofluid-based microactuators with integrated solutions (e. g. microfabricated coils) could only provide unidirectional forces which limited their application range.

In the present thesis, development of integrated ferrofluid-based microactuators is investigated. A new actuation method that uses planar spiral coils with bias fields is proposed to enable bidirectional ferrofluid manipulation. To demonstrate the potentials of the proposed actuation method, two proof-of-concept devices were developed. Active mirror cells with variable reflectivity were demonstrated as the first device and then a variable planar inductor with ferrofluid as a moving magnetic core was developed and characterized.

Another interesting application of ferrofluids in passive levitation of permanent magnets is also investigated for moving magnet based microactuators. Using this levitation mechanism a structurally simple and reliable microbearing is demonstrated. In order to demonstrate the effectiveness of such microbearing, a linear micromotor is first characterized and demonstrated. Also, frictional force and load carrying capacity of such microbearing is investigated showing very low frictional forces with good load bearing capabilities.

Given the promising results in the developed linear micromotor, a rotary micromotor with small axial size is developed for minimally invasive endoscopy applications. The characterization of developed prototype shows its potential to be used for real time medical imaging.

Preface

This thesis is based on the contributions that have been reported in the following papers:

Journal papers:

1. **B. Assadsangabi**, M. H. Tee, and K. Takahata, “Electromagnetic Microactuator Realized by Ferrofluid-Assisted Levitation Mechanism”, *Journal of Microelectromechanical Systems*, (Published online on Feb 26th 2014: DOI: 10.1109/JMEMS.2014.2305112).
2. **B. Assadsangabi**, M.S. Mohamed Ali, and K. Takahata, “Planar Variable Inductor Controlled by Ferrofluid Actuation,” *IEEE Transactions on Magnetics*, vol. 49, no. 4, pp. 1402-1406, 2013.
3. **B. Assadsangabi**, M.S. Mohamed Ali, and K. Takahata, “Bidirectional Actuation of Ferrofluid Using Micropatterned Planar Coils Assisted by Bias Magnetic Fields,” *Sensors and Actuators A: Physical*, vol. 173, no. 1, pp. 219-226, 2012.
4. **B. Assadsangabi**, X. Chen, D. Brox, and K. Takahata, “Ferrofluid Sacrificial Microfabrication of Capacitive Pressure Sensors,” *IEEE Sensors Journal*, vol. 14, no. 10, pp. 3442 – 3447, 2014.

Conference papers:

1. **B. Assadsangabi**, M. H. Tee, S. Wu, and K. Takahata, “Ferrofluid-assited micro rotary motor for minimally invasive endoscopy applications”, *27th IEEE Int'l Conf. Micro Electro Mechanical Systems (MEMS 2014)*, San Francisco, Jan. 26-30, 2014, pp. 200-203. (Podium presentation with 6% acceptance rate)

2. **B. Assadsangabi**, M.H. Tee, and K. Takahata, "Ferrofluid-Assisted Levitation Mechanism for Micromotor Applications," *17th IEEE Int'l Conf. on Solid-State Sensors, Actuators and Microsystems (Transducers 2013)*, Barcelona, Spain, June 2013, pp. 2720-2723. (Oral Presentation)
3. **B. Assadsangabi**, X. Chen, D. Brox, and K. Takahata, "Microfabrication of Capacitive Pressure Sensors using Ferrofluid Sacrificial Layers," *IEEE Sensors*, Baltimore, USA, November 2013, pp. 1-4. (Winner of Best Student paper award in Track)
4. **B. Assadsangabi**, M.S. Mohamed Ali, K. Takahata, "Ferrofluid-Based Variable Inductor," *25th IEEE Int'l Conf. Micro Electro Mechanical Systems (MEMS 2012)*, Paris, France, January 2012, pp. 1121-1124.

In addition, exact quotations from Journal papers appear in this thesis. Necessary permission has been obtained from the respective publishers to reproduce the reported results in this thesis. Here, I clarify that I am the principle researcher and main author in all the above mentioned publications and I conducted the literature survey, design, simulations, process development and fabrication. I also prepared the experimental setup and performed all of the measurements. The "Ferrofluid Sacrificial Microfabrication of Capacitive Pressure Sensor" paper in Appendix A, although related to ferrofluid application in MEMS, it was not placed in the main section of the thesis since it was not about ferrofluid-enabled microactuators which was the main focus of my research. Also, Dr. Kenichi Takahata and I filed a US provisional patent based on the research results presented in paper No. 1 in the journal publications as well as papers No. 1 and 2 in conference publications. All the manuscripts were co-authored

by my supervisor, Dr. Kenichi Takahata who has guided me in each and every aspect of my research. He provided me with the general idea for my research, and with guidance and continuous input and feedback throughout the research period. He also assisted me in writing the manuscripts.

Table of Contents

Abstract.....	ii
Prefaceiv	
Table of Contents	vii
List of Tables	ix
List of Figures.....	xi
Acknowledgements	xviii
Dedication.....	xix
Chapter 1: Introduction.....	1
1.1 MEMS Actuators.....	1
1.2 Ferrofluids	3
1.3 Ferrofluid Applications in Macro-devices.....	4
1.4 Ferrofluid-Enabled Microactuators	6
1.4.1 Microactuators With Ferrofluid as the Operating Medium	6
1.4.2 Microactuators Based on Ferrofluid Bearing	8
1.5 Research Objectives	9
1.6 Potential Impact of the Research	10
1.7 Research Methodology.....	11
1.8 Thesis Overview.....	14
Chapter 2: Ferrofluid Actuation Using Micropatterned Planar Coils Assisted by Bias	
Magnetic Fields	15
2.1 Introduction	15

2.2	Working Principle and Analysis.....	15
2.3	Ferrofluid Surface Displacement Measurement.....	22
2.4	Application: Active Mirror Arrays.....	25
2.4.1	Device Principle, Design, and Fabrication.....	25
2.4.2	Experimental Results and Discussion.....	28
2.4.2.1	Temporal Response.....	29
2.4.2.2	Dependence of Exposed Cell Area on Driving Current.....	31
2.4.2.3	Operation of Multiple Cells.....	32
2.5	Conclusions.....	36
Chapter 3: Planar Variable Inductor Controlled by Ferrofluid Actuation.....		37
3.1	Introduction.....	37
3.2	Device Design and Fabrication.....	39
3.3	Experimental Results and Discussions.....	41
3.4	Conclusion.....	49
Chapter 4: Electromagnetic Microactuator Realized by Ferrofluid-Assisted Levitation		
Mechanism.....		51
4.1	Introduction.....	51
4.2	Working Principle and Analysis.....	52
4.3	Design and Fabrication.....	57
4.4	Experimental Results and Discussion.....	59
4.4.1	Frictional and Levitation Force of Ferrofluid Bearing.....	59
4.4.2	Actuation Force.....	61
4.4.3	Actuation on a Single Coil.....	62

4.4.4	Continuous Actuation on the Coil Array	68
4.4.5	Position Control Between Two Coils	69
4.5	Conclusion	71
Chapter 5: Ferrofluid-assisted Micro Rotary Motor for Minimally invasive endoscopy		
	Applications	73
5.1	Introduction	73
5.2	Micromotor Design and Operation	75
5.3	Fabrication Process	78
5.4	Experimental Results and Discussion	80
5.4.1	Rotational Speed Characterization	80
5.4.2	Stator Thermal Characterization	85
5.4.3	Discussion	87
5.5	Conclusion	87
Chapter 6: Conclusion		
6.1	Contributions	89
6.2	Future Works	92
Bibliography		
Appendices		
Appendix A Ferrofluid Sacrificial Microfabrication of Capacitive Pressure Sensors		
A.1	Introduction	105
A.2	Design and Fabrication	107
A.3	Experimental Results	114
A.4	Conclusion	117

List of Tables

Table 1-1: Summary of benefits and drawback for various actuation mechanisms used in microactuators	2
Table 1-2: The physical and magnetic properties of three types of ferrofluids	3
Table 2-1: Specifications for the finite element model of the planar spiral coil with a bias field.	18
Table 4-1: Specifications for the finite element model of the planar spiral coil	55
Table 4-2: Material properties and tilt test results for two type of ferrofluids	60

List of Figures

Figure 1.1 Ferrofluid	4
Figure 1.2: Ferrofluidic seal typical configuration.....	5
Figure 2.1: Distribution of B at a distance of 100 μm from the substrate of the coil produced with the same amount of driving current in opposite directions for the forward (upper) and reverse (lower) modes: (a) without a bias field, the overall peak of B is always at the center of the coil with opposite polarities; (b) with a bias field, B is always positive and its overall peak is at either the center or the outer edge of the coil, depending on the direction of current flow; a slight curve present in the bias profile is due to the non-uniformity in the field provided by the permanent magnet modeled. A cross-sectional view of the ferrofluid's response in each case is also illustrated.	20
Figure 2.2: Experimental setup used to measure ferrofluid surface displacement at the coil center point. Schematic of ferrofluid surface profile in (a) forward mode and (b) reverse mode	22
Figure 2.4: Ferrofluid surface displacement in reverse activation mode at coil central point as a function of time with 100 mA of applied current	24
Figure 2.5: Ferrofluid surface displacement in reverse activation mode at coil central point as a function of time with 400 mA of applied current	25
Figure 2.6: Schematic representation of the ferrofluid-based active mirror device: (a) inactive state of the device where most of the incident light is absorbed by the fluid; (b) active state of the device where most of the incident light is reflected on the mirror surface exposed by the actuation of the ferrofluid.	26

Figure 2.7: Sample designs of the active mirror arrays and their fabrication processes: (a) design of 3×1 array of the planar coil with the aluminum mirror (the dimensions indicated are as follows: $W = 100 \mu\text{m}$; $S = 150 \mu\text{m}$; $L_i = 1.2 \text{ mm}$; $L_o = 2.9 \text{ mm}$); (b) design of 3×3 array of the planar coil with the copper-clad mirror; (c) fabrication process steps for the device in (a); (d) fabrication process steps for the device in (b). 27

Figure 2.8: Fabricated devices with 3×1 and 3×3 arrays of mirror-coil cell. 28

Figure 2.9: Experimental setup used for device characterization. 29

Figure 2.10: Measured temporal response of the ferrofluid with the single coil-mirror cell: (a) captured frames at different times (white spots indicated with arrows are due to light reflection on the deformed fluid surface); (b) measured brightness (average of three separate measurements) in the center region of the cell (normalized to the maximum value) vs. activation time. 30

Figure 2.11: Removal of the ferrofluid on the single cell with varying driving current: (a) captured frames at three different levels of the current; (b) averaged and normalized plots of three low-pass-filtered brightness profiles measured along the three lines (A-A') at the three current levels. that the observed effect was associated with F_m that increased with the current (along with F_{th}), resulting in increased fluid volumes removed from the cell's surface. 32

Figure 2.12: Enhanced ferrofluid actuation using adjacent cells: (a) ferrofluid condition when only the middle cell is activated in the reverse mode; (b) the condition when the two side cells are additionally activated in the forward mode; (c) averaged and normalized plots of three low-pass-filtered brightness profiles measure along the three lines (A-A') on the middle cell shown in (a) and (b) under the two conditions; (d) effect of the level of forward-mode driving current to the side cells on the exposed area of the middle cell in the reverse mode. 33

Figure 2.13: Simultaneous activation of multiple cells in the arrayed devices: (a) ferrofluid actuated on all the cells in the reverse mode in the 3×1 device; (b) averaged and normalized plots of three low-pass-filtered brightness profiles measured along the three lines (A-A') shown in (a); (c) effect of the level of reverse-mode driving current to the side cells on the exposed area of the middle cell in the reverse mode; (d) demonstration of letter ("T") formation using the 3×3 device.	35
Figure 3.1: Configuration of the ferrofluid-based variable-inductor device.	38
Figure 3.3: Fabrication process.	41
Figure 3.4: A sample of the fabricated device (prior to ferrofluid injection).	41
Figure 3.5: Inductance changes measured at 10 MHz and 100 MHz for the operations in the forward and reverse modes.	42
Figure 3.6: Optical images of the variable inductor operated in the reverse mode at different driving currents showing varying displacements of the ferrofluid and exposed areas of the inductor.	44
Figure 3.7 Measured temporal response of inductance (at 10 MHz) of the device operated in (a) forward and (b) reverse mode at different driving currents.	46
Figure 3.8: Measured frequency dependence of (a) inductance and (b) Q factor of the device operated in the reverse mode at different driving currents.	47
Figure 3.9: Wirelessly measured resonances of the L-C tank formed using the fabricated variable inductor, showing (a) the frequency modulation with the driving current in the reverse mode, and (b) the resonant frequency vs. the driving current.	48
Figure 4.1: Schematic diagram of the electromagnetic linear micromotor based on the ferrofluid bearing.	52

Figure 4.2: Ferrofluid-levitated magnet in (a) attracting and (b) repelling modes.....	54
Figure 4.3: Normal component of the magnetic field generated by the planar coil at different elevations from the coil along the A-A' line indicated in the inset showing the coil pattern. .	56
Figure 4.4: Top view of the device design, showing the levitated magnet (PM) located on an array of the planar coils with its linear guide.	57
Figure 4.5: Fabrication process for the electromagnetic rail track.	58
Figure 4.6: (a) Fabricated sample device and (b) NdFeB magnet without ferrofluid (upper) and with the fluid (bottom) showing a levitation gap of $\sim 500 \mu\text{m}$	58
Figure 4.7: Levitation force generated with the ferrofluid bearing measured as a function of vertical displacement	60
Figure 4.8: Actuation force vs. driving current with an inset showing the measurement method.	61
Figure 4.9: Experimental set-up used to characterize dynamic responses of the sliders.....	63
Figure 4.10: Temporal response of the levitated 3.0 mm magnet slider to (a) 200 mA square-wave current, (b) 100 mA sine-wave current at 1 Hz, and (c) 100 mA sine wave current at 5 Hz (the zero-displacement location in (b) and (c) corresponds to the halfway point between the coil center and periphery); (d) fast Fourier transformation of the slider response at the current frequency of 5 Hz.....	64
Figure 4.11: Frequency responses of oscillated actuations at different driving currents for (a) the 3 mm magnet and (b) the 1.6 mm magnet, showing corresponding resonant frequencies.	65
Figure 4.12: Oscillation amplitude vs. driving current at 0.5 Hz frequency for the 3 mm and 1.6 mm magnets.....	67

Figure 4.13: Continuous actuation of the slider on its rail track; (a) logic used for the actuation; (b) measured average velocities of the 1.6 mm magnet slider with varying switching times; variations in the velocity levels (observed through three sets of measurements) are smaller than the marker used. 68

Figure 4.14: Measured step-mode displacements of the magnet slider actuated between two adjacent coils by varying current distribution to the coils. 70

Figure 5.1: Conceptual diagram of the developed micro rotary motor and its application to microendoscopic catheters. 74

Figure 5.2: Design of the planar stator component, showing two driving coils patterned on opposing sides of the flexible substrate, and their connections with the current controller. 76

Figure 5.3: Activation logic used to produce a 360° rotation. 78

Figure 5.4: Optical images of (a) μ EDMed magnet and nickel shaft tip , (b) the rotor assemblies with the magnet, prism mirror, and coupling shaft, (c) the ferrofluid-levitated magnet rotor in the stator tube and (d) side view of the completed proof-of-concept devices. 79

Figure 5.5: Experimental set-up used for (a) characterization of the fabricated rotary motor device and (b) preliminary test of endoscopic optical imaging through rotating mirror performed in a test tube with a color band. The image shown after the camera is an optical image of the actual mirror under rotation. 80

Figure 5.6: Angular scanning of laser beam (directed onto the inner wall of a plastic ring) by the rotating mirror showing the beam spot captured at each 90° step of one full rotation. 81

Figure 5.7: Rotation speed vs. driving current. Inset graph shows photodiode readings for the case of 8-ms switching time corresponding to the max speed recorded for the 1.6 mm rotor. 82

Figure 5.8: Photodiode readings for 6 ms switching time corresponding to the maximum recorded speed in water for the device with 1.6 mm rotor magnet	83
Figure 5.9: Endoscopic imaging test: (a) Rotating mirror at each 90° step detecting four different colors defined on the inner wall of the test tube; (b) detection of the green color component from the optical signals collected through the rotating mirror.	84
Figure 5.10: Stator temperature at different driving current for the device with 1.6 mm rotor. At each driving current, stator temperature is given for two cases (i.e. with and without rotor present in the device)	86
Figure 5.11: Stator temperature at different driving current for the device with 500 μm rotor. At each driving current, stator temperature is given for two cases (i.e. with and without rotor present in the device). Inset image shows the temperature distribution over the stator surface and measurement point taken by the infrared camera.	86
Figure A.1: A cross-sectional schematic of the capacitive pressure sensor.	106
Figure A.3: Fabrication process flow.	109
Figure A.4: SEM images of a sensor cavity filled with the ferrofluid A-300 acquired using Hitachi S3000N VP-SEM with its variable pressure mode (at 50 Pa).	110
Figure A.5: (a) Optical image of the device after coating Parylene-C on top of the ferrofluid filled in the cavity of the stainless-steel chip, (b) SEM images of the device after depositing titanium electrode on the Parylene-C film, and (c) membrane profile before ferrofluid removal measured along A-A' line shown in (b).	111
Figure A.6: A completed sensor chip placed on a Canadian penny	112
Figure A.7: Optical profilometer measurement results: (a) 2-dimensional surface profile (top) and the depth profile along the B-B' line (bottom) measured on the released membrane created	

with a 10- μm -deep cavity sensor, and (b) a measured depth profile of the released membrane created with a 30- μm -deep cavity sensor (Fig. A.5). 113

Figure A.8: Experimental set-up used to characterize the fabricated sensors. 114

Figure A.9: Measured capacitive response of the fabricated sensors to applied pressure at room temperature. 115

Figure A.10: Measured base capacitance of the developed sensor vs. ambient temperature. 116

Acknowledgements

I would like to express my utmost gratitude towards my supervisor, Dr. Kenichi Takahata, who gave me the opportunity to work on this fascinating project. I am truly honored to have had the chance to work so closely with such a brilliant researcher. He gave me the encouragement and freedom to try out my ideas and patiently guided me through this journey. This work would have never been possible without his support and guidance. He was always accessible for discussions and advice.

Sincere thanks to my qualifying, departmental and university exam committee members:

Professors Shuo Tang, Edmund Cretu, Boris Stoeber, Shahriar Mirabbasi, Alireza Nojeh, John Madden and Ryozo Nagamune.

I would like to extend my appreciation to my friends and colleagues in Dr. Takahata's Lab: Masoud Dahmardeh, Xing Chen, Dan Brox, , Min Hian Tee, Zhiming Xiao, Akio Taniguchi, Mohamed Sultan Mohamed Ali, Mirza Saquib us Sarwa, Jeffrey Fong, Simon Wu, Reza Rashidi and Anas Bsoul. Thank you for sharing with me your useful ideas and support during this time.

Dedication

To My Family

Chapter 1: Introduction

Over the past two decades, there has been a growing interest in micro-electro-mechanical systems (MEMS) which has transformed it from only a research concept into a multibillion dollar industry [1]. Microactuators are a large category of MEMS alongside microsensors. They have been successfully applied to a wide range of applications from consumer electronics [2] to medical devices [3].

In this chapter, various actuation mechanisms in MEMS are first discussed, including their advantages and disadvantages. Then, given the subject of present dissertation on ferrofluid-based MEMS, ferrofluid along its applications is briefly reviewed. A more detailed literature review on the current state of the art in ferrofluid-based microactuators is then presented, pointing out the areas that are going to be investigated during the present effort. At the end of this chapter, the research objectives, methodology and overview of this thesis are discussed.

1.1 MEMS Actuators

Various actuation schemes such as electrostatic, magnetic, thermal and piezoelectric actuations have been utilized in microactuators. Table 1-1 summarizes some of the strengths and shortcomings of the abovementioned actuation mechanisms.

Electrostatic actuators have been the preferred choice for small displacements in the micrometer range compared to other actuation mechanisms due to its compatibility with integrated circuit processes and structural simplicity [4]. However, the need for high voltages in electrostatic actuation has been the limiting factor for most microactuators based on this mechanism. Thermal actuators have the advantage of generating large forces while high power consumption and slow response time are their weak points [5]. The piezoelectric actuators provide large forces and fast

response times with low input powers and operating voltages [6]. However, piezoelectric actuators generally have limited deflection ranges resulting from the small strains in the piezoelectric films. Magnetic actuators compared to other actuation principles in microscale have the advantage of producing large forces (hundreds of μN) and large displacements (tens to hundreds of μm). However, the devices based on magnetic actuation generally suffer from scaling effects as the available magnetic force is proportional to the volume of the magnetic material and magnetic actuation is considered advantageous above a certain range (e.g. 1 to 10 μm) [7]. Ferrofluids are attractive alternative magnetic materials, as a large volume of the fluid can be easily injected into a cavity instead of micromachining solid-state magnetic materials.

Table 1-1: Summary of benefits and drawback for various actuation mechanisms used in microactuators

Actuation mechanism	Benefits	Drawbacks
Electrostatic	<ul style="list-style-type: none"> • Compatibility with IC fabrication processes • Low power consumption 	<ul style="list-style-type: none"> • Need for high voltages (tens to hundreds volts) • Small displacement output (few micrometers)
Thermal	<ul style="list-style-type: none"> • Large forces • Low voltages 	<ul style="list-style-type: none"> • High power consumption • Slow response time
Piezoelectric	<ul style="list-style-type: none"> • Large forces with fast response time • Low power consumption 	<ul style="list-style-type: none"> • Limited displacement output
Magnetic	<ul style="list-style-type: none"> • Large forces and displacements with fast response time • Large working distance 	<ul style="list-style-type: none"> • Unfavorable scaling at smaller dimensions • Complicated fabrication process

1.2 Ferrofluids

Ferrofluids are stable biphasic suspensions of magnetic nanoparticles in a carrier liquid, which can be either aquatic or organic solvent; a surfactant is coated on the nanoparticles to prevent agglomeration by overcoming the attractive van der Waals forces between the nanoparticles [8]. Thermal agitation (i.e. Brownian motion) keeps the particles suspended and coatings prevent them from sticking. The suspended nanoparticles are made of materials such as iron oxide with diameters on the order of 10-20 nm. The particles are small enough that the ferrofluid maintains its liquid characteristics under magnetic field influence, and at same time magnetic forces on the nanoparticles can induce fluid motion. Ferrofluids can be manipulated by applying spatially-varying external magnetic fields. Table 1-2 shows the physical and magnetic properties of three types of commercial ferrofluids with three different carrier fluids.

Table 1-2: The physical and magnetic properties of three types of ferrofluids

Properties	EFH-1	EMG-807	A-300
Carrier fluid	Light Hydrocarbon	Water	Alkylnaphthalene
Viscosity (cP)	6	<5	300
Saturation of magnetization (mT)	44	11	34
Density (g/cm ³)	1.21	1.1	1.26

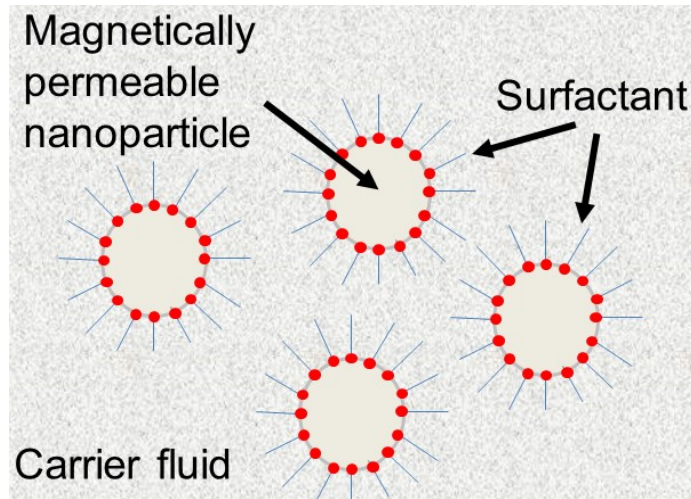


Figure 1.1 Ferrofluid

1.3 Ferrofluid Applications in Macro-devices

Ferrofluids have unique properties and their response under magnetic field influence can be exploited in variety of interesting applications ranging from inertia dampers [9] to medical applications [10]. In this section two examples of such applications are briefly presented:

I. Ferrofluidic Seal

Ferrofluids are widely used to provide sealing as a rotary feed-through sealing solution in high vacuum environments [11]. Figure 1.2 schematically shows the ferrofluidic seal typical configuration. As the result of permanent magnet field, ferrofluid is concentrated between the shaft and the pole piece in a rotary feed-through. The magnetic fluid maintained in the gap by the magnetic force, performs like an O-ring, keeping fluid from escaping even in the presence of a pressure differential. In typical commercial vacuum feed-throughs, a single stage can sustain a differential pressure of 200 mbar.

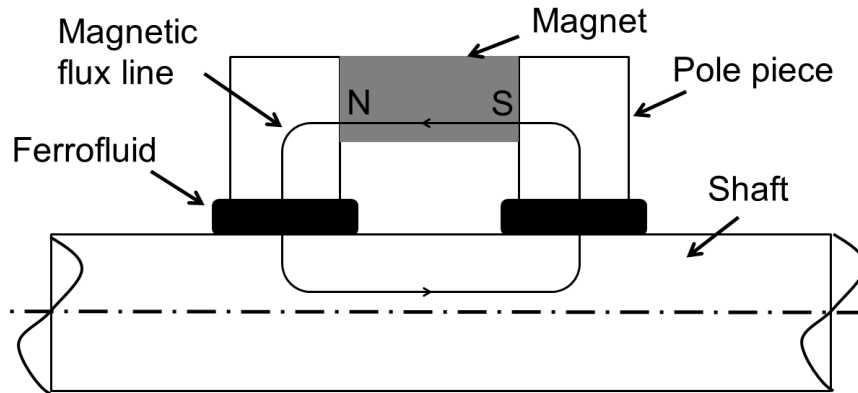


Figure 1.2: Ferrofluidic seal typical configuration

A direct application of the ferrofluidic seals can be found in the equipment used in the integrated circuits fabrication process, which requires a contaminant free environment. For example, a robot arm with a ferrofluid seal can be used for wafer transportation.

II. Ferrofluid as Heat Sink in Speakers

Overheating in a speaker voice coil can lead to speaker failure. The failure is due to the expansion in the voice coil that scrapes the top plate of the loudspeaker. In ferrofluid-based speakers, voice coils are immersed in the fluid and the heat is dissipated from the coil much faster therefore improving the efficiency and speaker lifetime. Figure 1.3 schematically shows a typical configuration of a speaker based on ferrofluid cooling.

As ferrofluid temperature rises, it becomes less magnetic, therefore the magnet placed near the voice coil will attract cold ferrofluid more than hot ferrofluid thus heated ferrofluid will move away from the voice coil, resulting in effective cooling of voice coil region.

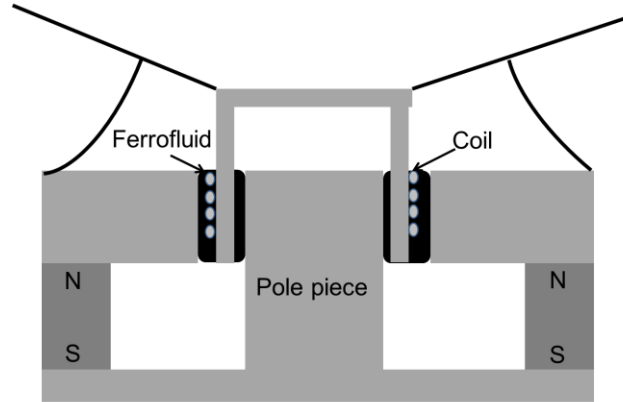


Figure 1.3: Ferrofluid as a heat sink in a speaker

1.4 Ferrofluid-Enabled Microactuators

The use of ferrofluids for microactuator applications can be grouped into two main categories. The first category includes the devices that utilize ferrofluids as the working medium to perform the intended task in the device such as pumping, mixing, light intensity modulation, etc. One distinctive advantage of using ferrofluids over other magnetic materials (e.g. permalloy, SmCo and NdFeB) in such devices is the simplicity of ferrofluid introduction into the device which can be done by fluid injection into a reservoir without the need for extra microfabrication processes such as thin film deposition and/or electroplating. In the second category, ferrofluids are used as a bearing to levitate permanent magnets and reduce the friction between rotor and stator in moving magnet microactuators. In this section, a brief introduction is given on each category to provide some background on the ferrofluid actuation methods.

1.4.1 Microactuators With Ferrofluid as the Operating Medium

Ferrofluid-based actuators have been extensively studied [12]–[16]. The efforts have led to various attempts for micro-electro-mechanical systems (MEMS) and microfluidic applications of the ferrofluid actuation [13]–[21]. One of the common manipulation methods has been to physically move permanent magnets over ferrofluid surfaces [12]–[16], [22]. However, this

approach requires macro-scale positioning mechanisms to move the magnets, thus the overall systems become large and complex. External solenoid-type electromagnets were also utilized to actuate ferrofluid for various applications [23]–[25], [17], [18]; however, these electromagnets tend to be bulky and large in order to generate the field strength sufficient to implement controlled actuation of the fluid thus pose inherent issues in the integration and packaging of the devices. MEMS-based devices that incorporated planar microcoils to generate magnetic fields for ferrofluid manipulation were developed to address the integration issue [19]–[21]. This approach is potentially beneficial for the miniaturization of ferrofluid-based actuators as planar coils can generate high magnetic-field gradients and fluxes [26]. The studies reported in [13] and [14] showed the manipulation of a ferrofluid droplet inside silicone oil. In this operation, silicone oil is necessary to suspend the droplet as well as to dissipate heat produced by the planar coils. Another study reported a light modulator based on ferrofluid actuation with planar microcoils [21]. In this device, the ferrofluid that is stored in the microchannels created around the coil is attracted to the center portion of the coil where the peak of the magnetic field strength appears when a current is passed through the coil. Upon the removal of the current, the fluid returns to the initial state due to the surface tension force in a passive manner. Despite the fast response, the optical modulation is limited to part of the device area, creating unresponsive regions in the device. The operation of the device is also hindered by the thermocapillary force caused by a surface-tension gradient that moves the fluid from a high-temperature site to a low-temperature site [27], i.e., from the coil region that produces Joule heat to the surrounding region, effectively damping the magnetic actuation in the device. This condition limits the level of the driving current that can be used; increasing the current raises the field strength or magnetic force but also produces more heat in the coil so that the undesired thermal effect becomes the dominant factor

in the fluid motion. This represents a fundamental constraint in the approach that uses planar coils for magnetic actuation of ferrofluid. Another constraint is that the magnetic fluid actuation is only available in the single direction, from the periphery to the center of the coil, which limits the application range of the approach.

1.4.2 Microactuators Based on Ferrofluid Bearing

Micromotors are key elements that enable a broad range of microdevice applications, e.g., microfluidics [28], microrobotics [29], micro-scale stages [30], and biomedical devices [31] including intelligent implants. One of the main challenges in realizing practical rotational/linear micromotors is the friction between the stator and the rotor/slider [32], [33]. For electromagnetic micromotors, frictions become a critical limiting factor in their miniaturization as electromagnetic forces depend on their volume whereas friction losses are determined by the surface area. In addition, large electromagnetic attraction forces between the stator and rotor/slider can further contribute to friction-related losses [34]. Various antifriction methods have been proposed in order to address these issues. Fluidic bearings have been incorporated to support the weight of a rotor while decreasing the friction in both active and passive manners. Active fluidic bearings [35] that require external pressurizing means inherently pose integration issues. Passive bearing action is typically achieved by creating specific fluidic or solid layers on micromotor structures [36]–[39]. Microball bearings are another passive approach that has been investigated [40]–[42]. However, the integration of these passive bearing structures with micromotors requires many microfabrication and packaging steps, leading to high complexity and high costs in their implementations. Although electromagnetic levitation based on the Lorentz force has also been utilized as another bearing mechanism to address the friction, the reported techniques not only require multi-layered coil configurations [32] or large device areas

[43], posing miniaturization and integration issues, but also suffer small load carrying capacities limited by their levitation forces and power consumptions.

As ferrofluid is applied onto a permanent magnet, due to strong magnetic fields on its poles, ferrofluid is accumulated on those areas. The accumulated layer of the fluid is subjected to an external pressure generated by the magnetic field and lifts the magnet up when positioned on its substrate, enabling fully passive levitation with zero power consumption. The ferrofluid layer essentially acts as a self-sustained lubricant and bearing that physically follows the magnet as it moves, realizing smooth motions of the magnet with minimal frictions. Although, the electromagnetic actuation of ferrofluid-levitated magnets has been demonstrated [44]–[46]; however, these studies only utilized large Helmholtz coils for actuation while presenting little or no information about the characteristics important for microactuator applications such as friction forces and load carrying capacities. Given the fact that one of the most challenging factors in realizing practical micromotors has been the friction, ferrofluid-based microbearing could be a simple and reliable solution that should be studied.

1.5 Research Objectives

As noted above, various efforts to incorporate ferrofluids in microactuators have been reported however, due to number of issues, the use of such fluids is still very limited in MEMS which suggests the need for further investigation of their applications in MEMS and microactuators in specific. The present research is aimed at investigating ferrofluids' potentials as enabling elements in microactuators as well as other microdevices that could benefit from unique properties of such smart fluids. More specifically, two main objectives have been defined for this research. The first objective was to identify the performance and limitations of ferrofluids in the operation of fully integrated ferrofluid-enabled microactuators using microfabricated coils and

the second goal was to investigate the potential applications of ferrofluids in various microactuator applications. In terms of having microactuators with integrated designs, microfabricated coils were chosen as the actuating element however since these coils imposed adverse thermal effects, research focus was to develop a method to minimize the thermal impact compared to magnetic effect of the microfabricated coils. In light of the abovementioned constraints, the objective was to design and fabricate microactuators that could benefit from both thermal and magnetic forces associated with ferrofluid actuation using planar coils. Another objective was set to study the use of ferrofluid bearing for micromotor applications. First focus of this part was to investigate the feasibility of this technology in providing a simple and reliable microbearing for micromotors and then the goal was to demonstrate an application which can uniquely benefit from this type of bearing.

1.6 Potential Impact of the Research

Given the ferrofluids' unique properties, numerous applications in areas such as microfluidics [13], [14], [16] and optofluidics [15], [21] in MEMS field can exploit these fluids. However, due to certain constraints, use of ferrofluids in microactuators is still very limited. One of the practical challenges faced in this field is the lack of miniaturization/integrated solutions for ferrofluid actuation therefore; most of the microactuators would rely on external macro coils or motors to operate. Planar microfabricated coils on the other hand can provide embedded actuation means however, Joule heating is the main restricting factor which also limits the maximum driving current and magnetic force for this type of coils. Another limitation associated with planar coils is that they can only provide actuation force in a single direction which also narrows down the application range of the designed microactuators based on these coils. As will be discussed in detail in Chapter 2, ferrofluid actuation using micropatterned planar coils assisted

by bias magnetic fields can greatly expand the range of applications that can utilize ferrofluids as an operating medium.

Another unexploited ferrofluid application is the use of ferrofluid bearings for moving magnet microactuators. One of the most challenging factors in realizing this type of microactuators has been the friction between the rotor/slider and the stator. In this dissertation, a novel approach based on passive levitation of permanent magnets using ferrofluids is demonstrated to be an effective bearing for microscale devices. This extremely simple, assembly-free ferrofluid micro bearing could be applied to a variety of microactuators for various applications in microfluidics and medical fields to enable high-reliability devices with low costs.

In summary, the results of current dissertation can be utilized to enable the development of integrated ferrofluid-based microdevices for wide range of applications in various fields.

1.7 Research Methodology

Consequent to the discussion in the previous sections, two types of integrated ferrofluid-enabled microactuators are investigated in the present thesis. Therefore, the research described in this dissertation can be divided into two main categories:

- a) Development of microactuators which rely on ferrofluids as a working medium to perform the intended task in the device (Sections A, B and C below).
- b) Development of microactuators which utilize ferrofluid-assisted levitation of permanent magnets as a bearing mechanism (Sections D and E below).

The following approach was carried out to achieve the research objectives in each abovementioned categories:

A. Magnetic Field Simulation of Integrated Actuation Scheme Based on Planar Coils Assisted by Bias Fields

As mentioned above, literature review shows certain limitations in ferrofluid actuation using planar microfabricated coils such as adverse thermal effects and unidirectional actuation possibility. In order to circumvent these constraints, a new actuation scheme using planar coils assisted by bias fields was proposed enabling bidirectional ferrofluid actuation at lower driving currents. In order to predict the ferrofluid response in the proposed scheme, magnetic field distribution over the planar coil surface was simulated using finite element method.

B. Experimental Verification of Ferrofluid Response to the Developed Actuation Scheme

Based on the acquired simulation results, the ferrofluid response to magnetic field generated by microfabricated planar coil biased by the field from a permanent magnet was experimentally verified. In this part, ferrofluid surface displacement was characterized to provide information on the displacement ranges that could be expected in similar device configurations.

C. Design, Fabrication and Characterization of Microdevices Based on Ferrofluid-Enabled Microactuation

Using the proposed actuation scheme, two proof-of-concept microactuators were developed in this section.

The first device was mirror cells with variable reflectance capability. Ferrofluid was used to cover the mirror surface in the off-state of the cell blocking most of the incident light to the mirror and then as the ferrofluid was removed from mirror surface due to the magnetic force from the planar coils, cell reflectivity was varied. A device with array of such cells was also fabricated and characterized for multiple cell actuation responses.

As the second proof-of-concept device, a variable inductor with ferrofluid as a moving magnetic core was developed and characterized. Ferrofluid in the reservoir created on the inductor was

displaced using magnetic-field gradients produced by another planar coil (actuation coil) that was aligned to the inductor. Experimental characterizations were performed to compare the device performance between the two (repelling and attraction) modes of ferrofluid actuation and it was found that repelling of ferrofluid from inductor surface which was uniquely enabled in the proposed actuation scheme, significantly enhanced the tuning range of the inductor compared to ferrofluid attraction toward inductor center.

D. Development of a Linear Microactuator Based on Ferrofluid Levitation of Permanent Magnets

As mentioned above, another objective of the present dissertation was to investigate the use of ferrofluid bearing for micromotor applications. Ferrofluid bearing load carrying capacity was first estimated using an analytical model and then experimentally verified. Frictional forces of the bearing were also characterized for two types of ferrofluid with different viscosities. Also, using an analytical formula together with a finite element analysis, dynamic response of the levitated magnet to magnetic field generated by planar spiral coils was predicted. Finally a linear micromotor prototype was fabricated and characterized showing the effectiveness of such microbearings.

E. Development of a Rotary Micromotor for Minimally Invasive Endoscopy Application

Given the promising results of Section D, the use of ferrofluid bearing in rotary micromotors for minimally invasive endoscopic applications was investigated. Two micromotor prototypes were fabricated and characterized to evaluate the performance of such devices for medical imaging applications. Preliminary demonstration was also performed to feasibility and effectiveness of such micromotors for various medical imaging modalities.

Also, as another ferrofluid application for MEMS, a new method was proposed based on ferrofluid sacrificial layer to fabricate suspended membranes in capacitive pressure sensors. To demonstrate the feasibility of such fabrication method, a pressure sensor was fabricated and characterized showing promising results for further development of the method for other applications.

1.8 Thesis Overview

This dissertation is divided into 6 chapters. The research background, objectives and research methodology are described in Chapter 1. Chapter 2 focuses on the ferrofluid actuation method based on magnetic field provided by planar coils biased by permanent magnets. At the end of Chapter 2 (Section 2.4 and 2.5), application of the proposed actuation method is demonstrated in active mirror cells providing variable optical reflectivity. Chapter 3 focuses on the design, fabrication and characterization of a variable inductor based on ferrofluid as a moving magnetic core. This chapter is also based on the integrated actuation method developed in Chapter 1. Chapter 4 describes the design, development and characterization of a linear micromotor enabled by ferrofluid-assisted levitation of permanent magnets. Also, the load carrying capacity and frictional force of ferrofluid microbearings are experimentally evaluated in this chapter. In Chapter 5, ferrofluid microbearing is utilized for the development of a rotary micromotor with the target application in minimally invasive endoscopic imaging. The last chapter, Chapter 6, discusses the findings and contributions and provides direction for future work in this research field. Mentioned in the appendix, an additional ferrofluid application as a liquid sacrificial layer in the fabrication of capacitive pressure sensors is presented.

Chapter 2: Ferrofluid Actuation Using Micropatterned Planar Coils Assisted by Bias Magnetic Fields¹

2.1 Introduction

In this chapter, a new method that uses planar spiral coils with bias fields for the ferrofluid actuation is discussed to circumvent the issues involved in ferrofluid actuation discussed in Chapter 1. A combinational use of a controlled magnetic field and a bias field is shown to provide lateral forces that attract or repel the ferrofluid to/from the coil depending on the direction of the current passed through the coil. The actuation principle is discussed in detail using finite element analysis (FEA) and experimentally demonstrated afterwards. As a proof-of-concept of the method, active mirror devices are then developed toward the application to imaging devices and optical switches. The planar devices lithographically fabricated to have arrays of mirror-coil cells are used to demonstrate activation/deactivation of individual cells enabled by the bidirectional radial motion of the ferrofluid layer with $\sim 100 \mu\text{m}$ thickness. The static and dynamic behaviors of the ferrofluid in the devices are characterized through an image processing approach. Multiple mirror cells are selectively and simultaneously operated to show enhanced ferrofluid control uniquely available with the two modes of the actuation as well as to demonstrate pattern generation with the arrays.

2.2 Working Principle and Analysis

To study ferrofluid response to magnetic fields, basic concepts in magnetism are first briefly explained.

¹ Part of this chapter appeared in the following publication:

B. Assadsangabi, M.S. Mohamed Ali, and K. Takahata, "Bidirectional Actuation of Ferrofluid Using Micropatterned Planar Coils Assisted by Bias Magnetic Fields," *Sensors and Actuators A: Physical*, vol. 173, no. 1, pp. 219-226, 2012.

Any material that is magnetized by magnetic field is considered as a magnetic material. Magnetic materials can be grouped into the following main groups based on their responses to external magnetic fields: ferromagnetic, ferromagnetic, paramagnetic, diamagnetic and superparamagnetic. Ferrofluids are superparamagnetic which means that an external magnetic field is able to magnetize the nanoparticles in the fluid, similar to paramagnetic materials. However, their magnetic susceptibility (χ , a constant that indicates the degree of magnetization of a material in response to an applied magnetic field) is much larger than paramagnetic materials which are only slightly magnetized by magnetic field.

Magnetic induction (B), magnetic field intensity (H) and magnetization (M) are related by:

$$B = \mu_0 (H + M) \quad (2.1)$$

where μ_0 is the free space magnetic permeability which shows the degree of magnetization that free space obtains in response to an applied magnetic field. For superparamagnetic materials M and H vectors are in the same direction and have the following relationship:

$$M = \chi H \quad (2.2)$$

The magnetic moment applied on ferrofluid is defined through the following equation:

$$m = VM \quad (2.3)$$

The magnetization M is the magnetic moment m per unit volume (V). Based on this definition, one can calculate the energy (U) due to magnetic interaction:

$$U = -(m \bullet B) \quad (2.4)$$

The magnetic force applied on ferrofluid can be obtained from (4) as:

$$F_m = -\nabla(m \bullet B) \quad (2.5)$$

By introducing the del (∇) operator:

$$\nabla = \frac{\partial}{\partial x} i + \frac{\partial}{\partial y} j + \frac{\partial}{\partial z} k \quad (2.6)$$

and using the following vector identities:

$$\nabla(m \bullet B) = (m \bullet \nabla)B + (B \bullet \nabla)m + m \times (\nabla \times B) + B \times (\nabla \times m) \quad (2.7)$$

$$\nabla(B \bullet B) = 2B \times (\nabla \times B) + 2(B \bullet \nabla)B \quad (2.8)$$

Noting that m is a constant vector and $(\nabla \times B) = 0$ (from Maxwell equations), the magnetic force F_m , that acts on the ferrofluid can be expressed as [19]:

$$F_m = \frac{V\Delta\chi}{\mu_0} (B \bullet \nabla)B = V\Delta\chi \nabla \left(\frac{B^2}{2\mu_0} \right) \quad (2.9)$$

Eq. (2.9) indicates that the magnitude of the magnetic force applied to ferrofluid depends directly on the magnetic flux density and its gradient, and also that the force is directed towards the regions with higher magnetic flux densities absolute values. In the proposed actuation method, the ferrofluid placed on top of a planar coil is controlled by the magnetic field produced by the coil which is superimposed on the bias field provided by the permanent magnet. In the investigated arrangement, the gradient is generated by the planar coil.

Another force that displaces ferrofluid is the thermocapillary force (F_{th}) caused by Joule heating of the coil as noted in Chapter 1. This force pushes the fluid on a coil towards the outside of the coil (where temperature is lower) thus dampens the magnetic force. In addition, ferrofluid experiences the force due to the viscosity of the fluid (F_v) which opposes the fluid motion.

It was experimentally observed that when the driving current was higher than 100 mA, F_{th} became the dominant force and the fluid was removed from the center of the coil to its periphery (this current level is identical to the upper limit of driving current reported in [21]). In order to magnetically control the ferrofluid motion, the magnitude of F_m should be larger than that of F_{th} .

One apparent approach to increase F_m may be to increase the number of turns in the coil so as to increase B in the center of the coil. For a solenoid-type coil, the magnetic field at the center of the coil proportionally increases with the number of turns. However, this is not the case for planar coils, as adding more turns to the periphery of the coil leads to the increase of the distance between the added turns and the center of the coil, resulting in less contribution of the added turns to increasing B at the coil's center. Moreover, adding more turns increases the overall size of the coil, undesirable in terms of device miniaturization. Another approach may be to decrease the thermocapillary effect by adding a thermal insulating layer between the coil and ferrofluid; however, this addition causes an increased distance between them which reduces F_m .

An alternative path to addressing the above constraints is to use a bias field so that the coil's current, or resultant Joule heat, necessary to achieve a certain level of B in the system can be much smaller than the case that the coil is the only source for the field production. For this biasing, a permanent magnet can be arranged so that the level of B at the location of ferrofluid is slightly smaller than the threshold level required to actuate the fluid, and that superimposing a small additional field provided by the coil is sufficient to trigger the actuation of the fluid. This

Table 2-1: Specifications for the finite element model of the planar spiral coil with a bias field.

Parameter	Value
Coil's wire width / spacing / thickness	100 μm / 150 μm / 20 μm
Number of turns	4
Coil's inner length / overall size	1.2 mm / 2.9 mm
Applied current	1 A
Permanent magnet remanent magnetization	7.5×10^5 A/m
Permanent magnet size	$3 \times 3 \times 3$ mm ³
Distance between coil and magnet	8 mm

approach may also permit the use of the coils with smaller numbers of turns, which will contribute to downsizing of the device. Another important feature enabled by the biasing is the ability to implement the bidirectional actuation of ferrofluid, unavailable with the non-biased case. This effect was investigated through FEA using COMSOL Multiphysics®. Table 2-1 shows the specifications of the model that is comprised of a planar spiral coil and a permanent magnet placed below the coil in air. The specifications were chosen according to the actual values used in the active mirror device and the experimental set-up (discussed in section 2.4.2). A relatively large current (1 A) was used to clearly visualize the effects in the simulation. The distance between the permanent magnet and the coil was set to make the magnetic flux density smaller than the critical value in ferrofluid that causes non-uniform patterns on the fluid's surface (so-called the normal-field instability) [8]. Figure 2.1(a) shows the simulation results of the profiles of B over the coil at a 100 μm distance from the coil's surface when the current is passed through the coil in opposing directions, defined as forward and reverse for counterclockwise and clockwise directions, respectively, and when no bias field is present. As can be seen, the two profiles are symmetric and have opposite polarities. In either case, the positive or negative peak of the overall profile appears at around the center of the coil. Because of the gradients (the magnitude of B increases toward the center of the coil), the ferrofluid will be attracted toward the center region if placed on the coil, regardless of the current direction. The situation will be different when a bias field is superimposed in the manner described earlier. Figure 2.1(b) shows the simulation results with the permanent magnet positioned below the coil activated by the current in the two directions. In the forward mode, the peak of the overall B is at the center of the coil, which is the same as the case without the bias, thus the ferrofluid will be attracted toward the center. In the reverse mode, however, the overall B has the peaks at the outer edges of the

coil, whereas the B is in the lowest level at the center region. This profile moves the ferrofluid from the center to the outer edges of the coil, opposite to the forward-mode case. Therefore, the bidirectional actuation of ferrofluid can be achieved by switching the direction of the driving

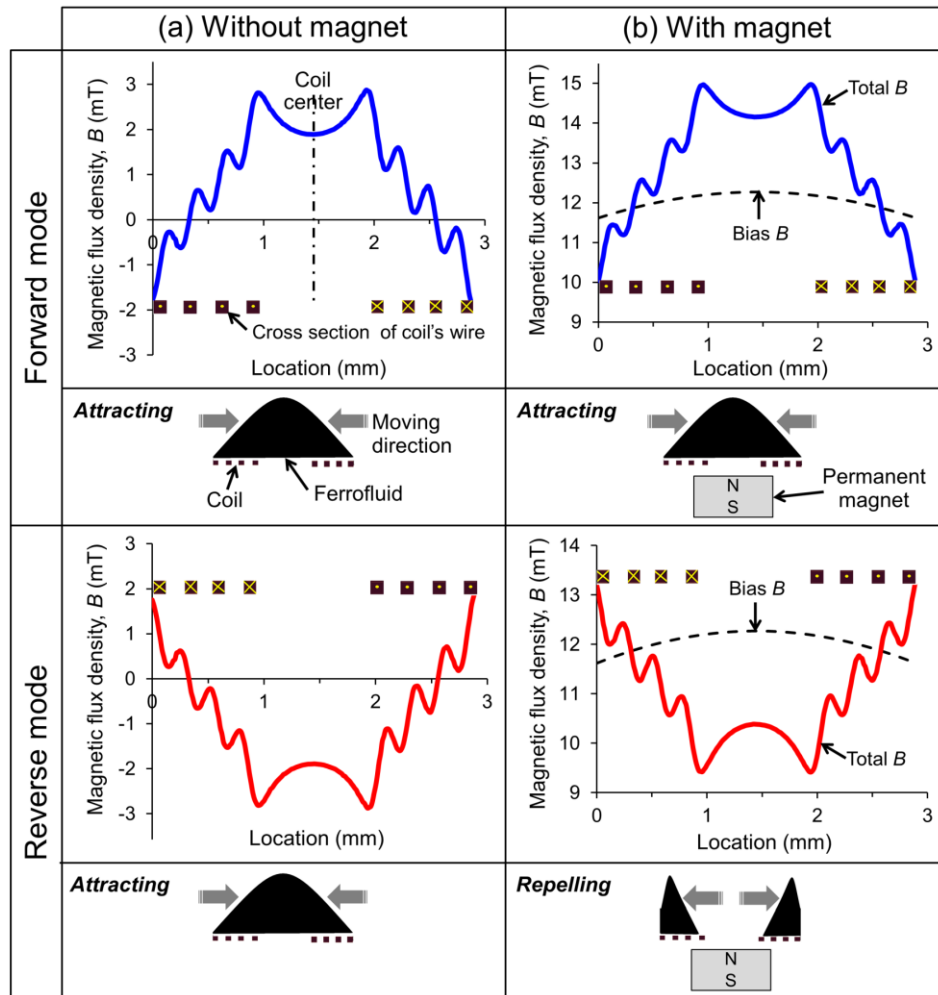


Figure 2.1: Distribution of B at a distance of $100\ \mu\text{m}$ from the substrate of the coil produced with the same amount of driving current in opposite directions for the forward (upper) and reverse (lower) modes: (a) without a bias field, the overall peak of B is always at the center of the coil with opposite polarities; (b) with a bias field, B is always positive and its overall peak is at either the center or the outer edge of the coil, depending on the direction of current flow; a slight curve present in the bias profile is due to the non-uniformity in the field provided by the permanent magnet modeled. A cross-sectional view of the ferrofluid's response in each case is also illustrated.

current. The thermocapillary force is still present so that it damps the ferrofluid actuation in the forward mode; however, this effect will be smaller because the current (or heat) can be substantially reduced due to the assist of the bias field as discussed earlier. Furthermore, in contrast to the forward-mode case, this thermal force enhances the fluid actuation in the reverse mode. These mean that the sign of F_{th} is opposite to that of F_m when operated in the forward mode but identical to it when operated in the reverse mode. In order to evaluate the effect of F_{th} in comparison with F_m , a control experiment was performed using the carrier fluid (hydrocarbon-based oil) of a commercially available ferrofluid (EFH1, Ferrotec Co., NH, USA, with saturation magnetization of 40 mT and viscosity of 6 cp) without magnetic particles so that the fluid does not produce F_m but F_{th} . The result was compared with the response of the original ferrofluid under the same conditions in the reverse mode. In this experiment, the same volume of each of the fluids (i.e., the carrier fluid and the original ferrofluid) was injected into a reservoir created above the coil area, and then a driving current was applied and increased until the coil's central area was first exposed. The minimum current to achieve this condition for the carrier fluid was measured to be 1.3 A, whereas the current for the ferrofluid case was 0.3 A, $\sim 4.3\times$ smaller than the carrier-fluid case. The response time to reach the above condition was 6 seconds for the carrier fluid, which was reduced to 1 second with the ferrofluid. These results clearly indicate a large dominance of F_m over F_{th} .

In summary, as explained in this section, ferrofluid actuation using planar coils is influenced by multiple competing forces such as magnetic (F_m), thermocapillary (F_{th}), viscous (F_v), surface tension and gravitational forces resulting in a complex system which is not straightforward to mathematically model. Therefore, in the present thesis, experimental investigation of ferrofluid

actuation was adopted as the research methodology enabling validation of the proposed actuation method based on bias fields.

2.3 Ferrofluid Surface Displacement Measurement

In order to measure ferrofluid surface response, experimental setup shown in Figure 2.2 was used. A laser displacement sensor (LK-G32, Keyence Co., ON, Canada) was placed vertically above a reservoir filled with EFH1 ferrofluid with the thickness of $\sim 270 \mu\text{m}$. Also, a magnet was placed under the reservoir with 4.5 mm distance to the reservoir bottom surface. This distance was the minimum distance before the instability happened on ferrofluid surface. A 9-turn spirally shaped planar coil was glued to the reservoir bottom surface and then activated in both forward and reverse modes and surface displacement was measured at different applied current. Coil center point was chosen as the measurement point where the maximum upward displacement occurs in forward mode case. The measurement point in the reverse mode was not changed to demonstrate the downward surface movement in this mode.

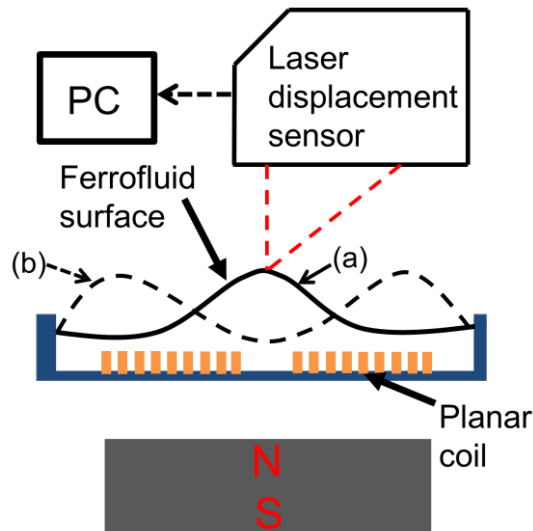


Figure 2.2: Experimental setup used to measure ferrofluid surface displacement at the coil center point.

Schematic of ferrofluid surface profile in (a) forward mode and (b) reverse mode

Figure 2.3 shows a typical response of the ferrofluid surface at coil center point when activated in forward mode. The results in Figure 2.3 is consistent with the predicted response in section 2.2. The displacement profile in Figure 2.3 shows an initial overshoot which is probably due to inertia as well as the transient overshoot in the applied current from the power supply (the current overshoot (e.g., ~ 0.6 A, when the target current was 0.1 A) was observed upon turning on the current with the particular supply used). The activation in the reverse mode has two regimes depending on the current level. Figure 2.4 and Figure 2.5 shows the displacement profile for the low and high current regimes, respectively. In low current regime (Figure 2.4) thermocapillary effect is still not visible in the response. The maximum current level for this regime is dictated by various design parameters such as ferrofluid volume and viscosity, cavity dimensions and actuating coil resistance. The displacement profile in Figure 2.4 confirms that ferrofluid surface goes down in reverse mode. Also, as in forward mode case, there is an initial overshoot in the displacement profile however, the overshoot amplitude in reverse mode is much smaller

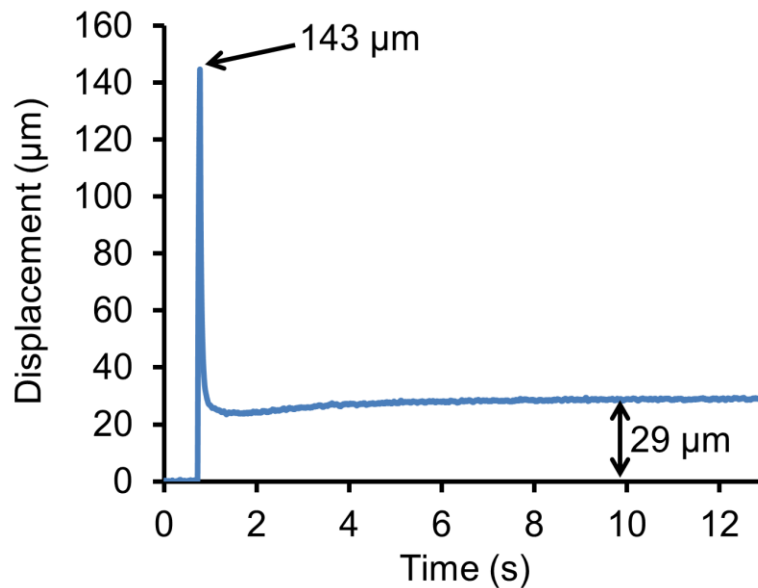


Figure 2.3: Ferrofluid surface displacement in forward activation mode at coil centre point as a function of time with 100 mA of applied current

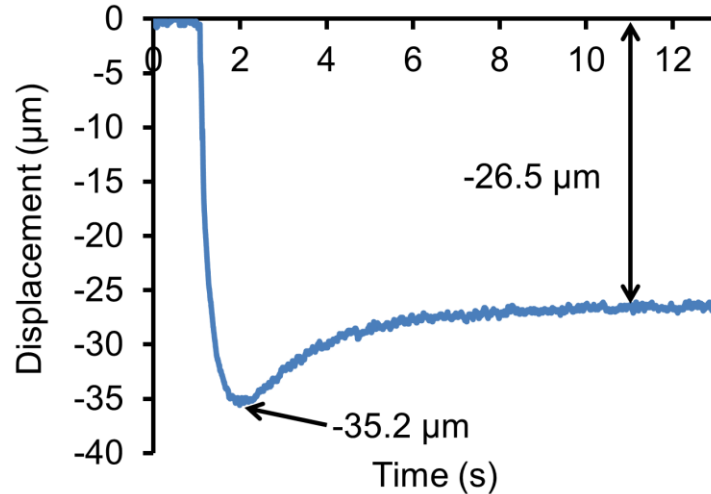


Figure 2.4: Ferrofluid surface displacement in reverse activation mode at coil central point as a function of time with 100 mA of applied current

compared to forward mode case which probably is due to the damping force that comes from the surrounding fluid in the reservoir limiting the outward motion of the fluid in the central portion of the reservoir. As driving current is increased in the reverse mode, thermocapillary effect becomes more visible in the ferrofluid response. Figure 2.5 shows the ferrofluid response in the high current regime (e.g. $> \sim 200$ mA in this particular experimental setup). As mentioned in previous section, in reverse mode, thermocapillary force acts in the same direction as the magnetic force, however, as seen in Figure 2.5 thermal response time is slower than the magnetic force which results in a slow outward fluid motion after initial fast downward motion of fluid surface due to magnetic force.

In summary, these results in this section confirmed the overall predicted ferrofluid response in section 0. It was observed that in forward mode case (tested up to 1 A of driving current), magnetic attraction force is a dominant effect compared to thermocapillary repelling force. In the reverse mode actuation however, it was observed that beyond certain driving current threshold which is dependent on the device design parameters, both magnetic and thermal forces contribute

to the ferrofluid removal from the central region of the coil increasing the total fluid displacement at a particular driving current. This mode of

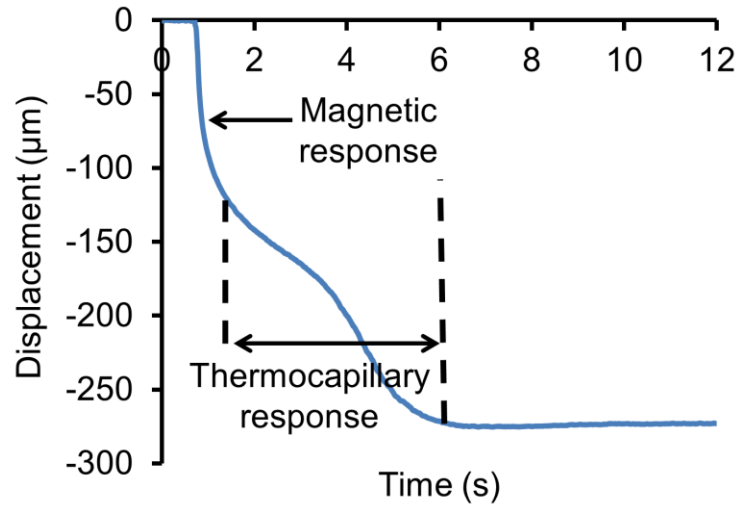


Figure 2.5: Ferrofluid surface displacement in reverse activation mode at coil central point as a function of time with 400 mA of applied current

operation (i.e. reverse mode) which is uniquely enabled by the proposed actuation scheme could broaden ferrofluid possible applications. In the following sections and also Chapter 3 two devices are developed which are enabled by the proposed actuation scheme.

2.4 Application: Active Mirror Arrays

This section describes the operation principle of the active mirror arrays based on the ferrofluid actuation mechanism discussed in the preceding sections, as well as the design and fabrication of the proof-of-concept devices. The operations of the devices are experimentally characterized and demonstrated in various activation conditions.

2.4.1 Device Principle, Design, and Fabrication

The active mirror device is operated by removing or attracting the ferrofluid placed over the mirror surface, which is created on a planar spiral coil (Figure 2.6). Ferrofluid is nearly opaque to visible light. Thus, when the coil is inactive (i.e., no current applied to it), most of the incident

light to the mirror is damped by the ferrofluid layer (Figure 2.6(a)). Upon the activation of the coil in the reverse mode, the ferrofluid is removed from the mirror surface due to F_m induced by the field gradient similar to the one shown in Figure 2.1(b) in combination with F_{th} , leading to the reflection of the incident light at the location (Figure 2.6(b)). Deactivating the coil allows the ferrofluid to return to the initial equilibrium state and cover the mirror again. This returning motion is assisted by the force generated by the bias field that pulls the fluid back to the coil location. In addition, the forward mode that actively attracts the fluid, due to the magnetic force induced by the field gradient depicted in Figure 2.1(b), may be used to accelerate the returning motion. Various planar devices with different coil arrangements were designed to evaluate the above operation mechanism. Sample device layouts with 3×1 and 3×3 arrays of the mirror-coil cell are illustrated in Figure 2.7(a) and Figure 2.7(b), respectively. The dimensions of the spiral

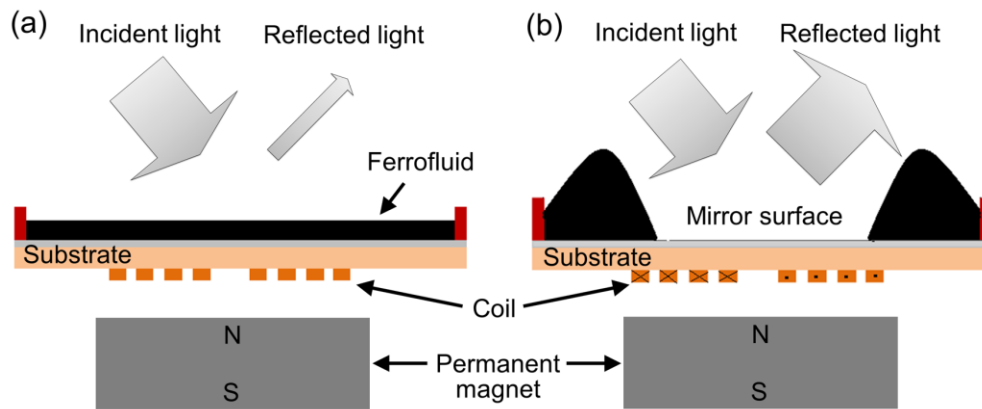


Figure 2.6: Schematic representation of the ferrofluid-based active mirror device: (a) inactive state of the device where most of the incident light is absorbed by the fluid; (b) active state of the device where most of the incident light is reflected on the mirror surface exposed by the actuation of the ferrofluid.

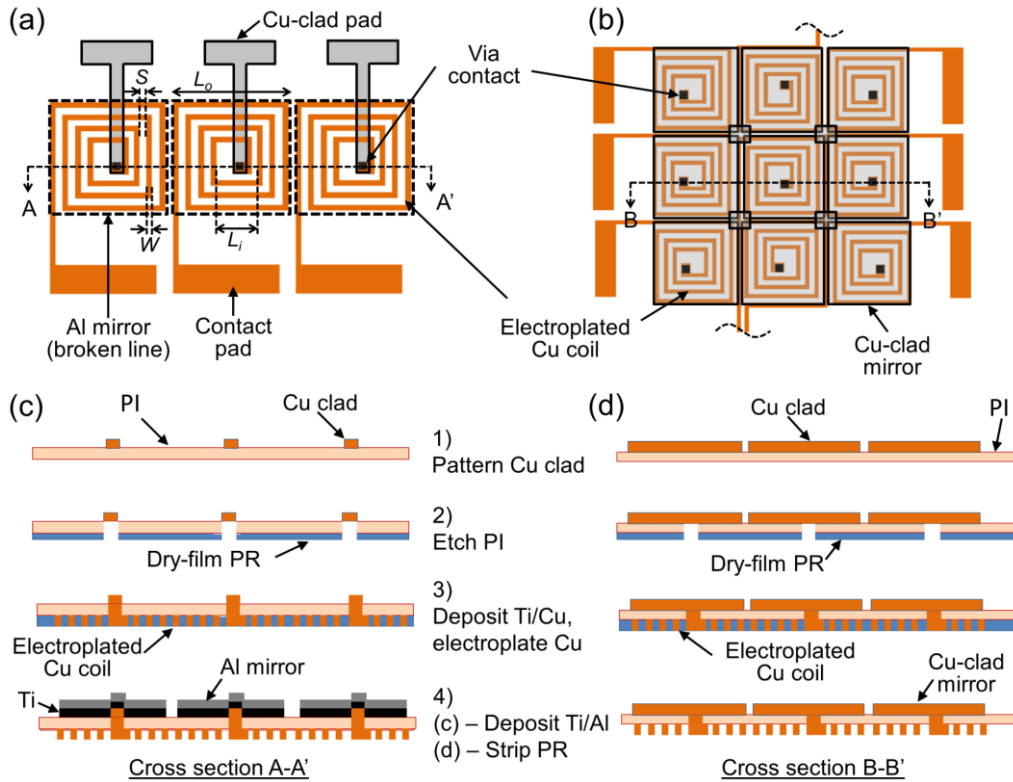


Figure 2.7: Sample designs of the active mirror arrays and their fabrication processes: (a) design of 3×1 array of the planar coil with the aluminum mirror (the dimensions indicated are as follows: $W = 100 \mu\text{m}$; $S = 150 \mu\text{m}$; $L_i = 1.2 \text{ mm}$; $L_o = 2.9 \text{ mm}$); (b) design of 3×3 array of the planar coil with the copper-clad mirror; (c) fabrication process steps for the device in (a); (d) fabrication process steps for the device in (b).

coils used in these devices are the same as those listed in Table 2-1. The devices are fabricated using single-sided copper-clad polyimide (PI) film with 50- μm thickness (G2300, Sheldahl Co., MN, USA) as the substrate through the fabrication process described in [47]. The fabrication processes for the 3×1 and 3×3 arrays are illustrated in Figure 2.7(c) and Figure 2.7(d), respectively. In these processes, the coils are formed on the PI side of the film by the electroplating of copper in order to form thick ($\sim 20 \mu\text{m}$) wire for the coils and reduce its parasitic resistance, i.e., the Joule-heating effect. The copper-clad layer with 5- μm thickness is used to

pattern the interconnect leads and contact pads for the 3×1 device – after this patterning, an aluminum layer (with a titanium adhesion layer) is deposited and patterned on the copper-clad

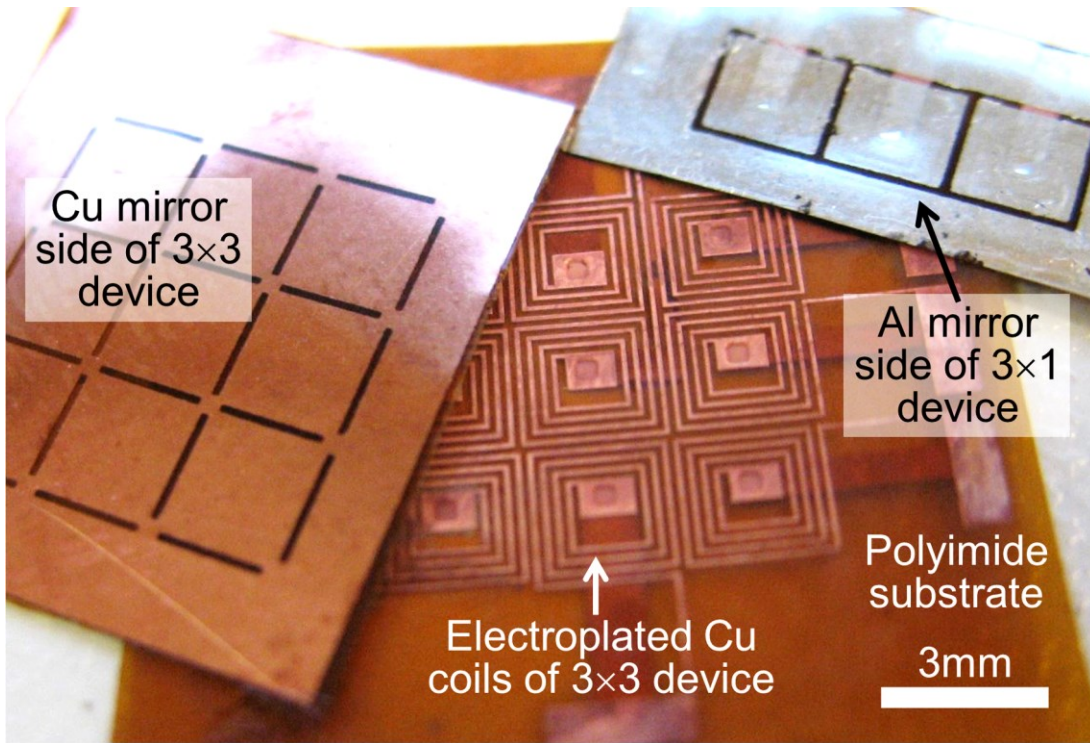


Figure 2.8: Fabricated devices with 3×1 and 3×3 arrays of mirror-coil cell.

side of the substrate to define square-shaped mirrors aligned to the coils. For the 3×3 device, the copper-clad layer is used as the contact pad, but also as the mirrors, by patterning the layer as shown in Figure 2.7(b) and Figure 2.7(d) instead of using the aluminum mirrors. Fabricated sample devices are shown in Figure 2.8.

2.4.2 Experimental Results and Discussion

The fabricated devices were characterized using the experimental setup shown in Figure 2.9. A commercial ferrofluid (EFH1) noted earlier was used for all the experiments. The ferrofluid was added onto the mirror surface that served as the bottom of a reservoir as shown in Fig. 5, while the thickness of the fluid layer was adjusted to be approximately 100 μm . Permanent NdFeB

magnets (K&J Magnetics, Inc., PA, USA) were placed underneath the mirror-coil cells at a distance that did not cause normal-field instability in the fluid (which was 8 mm for the particular magnets used). In each experiment, the temporal response of the ferrofluid and the reflection properties of the cell array were recorded with a video camera at a frame rate of 100 fps for quantitative analysis of the results. The recorded movies were converted to individual

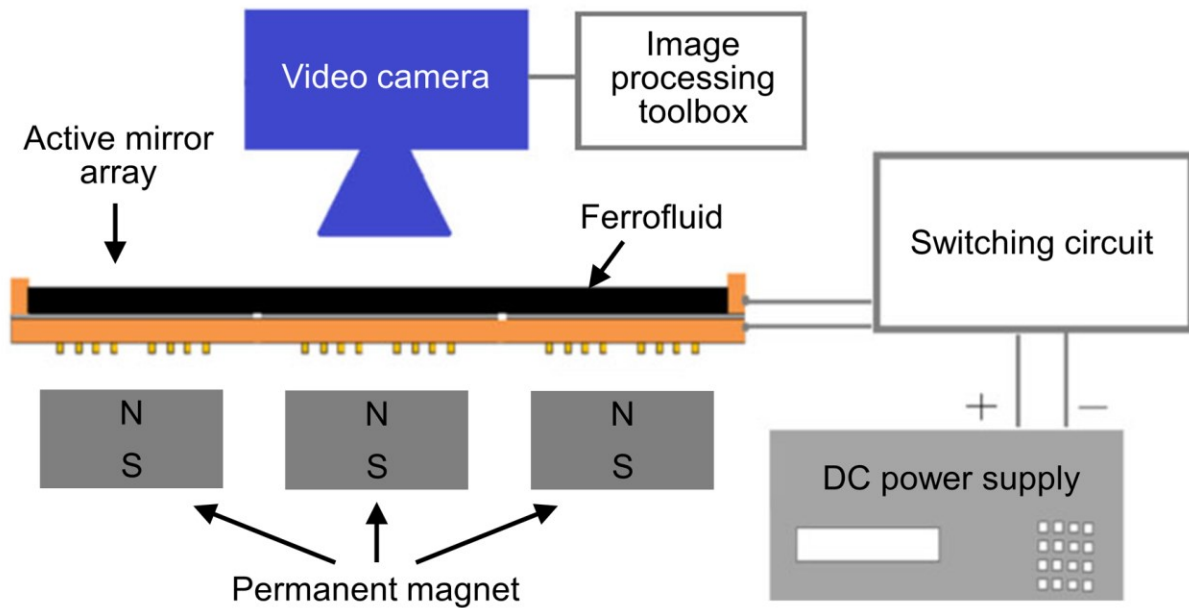


Figure 2.9: Experimental setup used for device characterization.

frames to evaluate the above characteristics. The image processing toolbox of MATLAB® was used to extract brightness profiles on the array from the converted frames.

2.4.2.1 Temporal Response

Figure 2.10(a) shows a series of the frames captured while activating one of the coils in the 3×1 array in the reverse mode with a current of 400 mA, displaying the progress in deformation of the ferrofluid layer on the cell region. (Note that the aluminum reflective layer deposited on this and other devices resulted to be thin enough to make the copper-clad patterns underneath the

layer visible – this issue can be easily solved by simply increasing the thickness of the aluminum layer.) The deformation (thickness reduction) of the fluid layer can be seen at ~10 ms after the

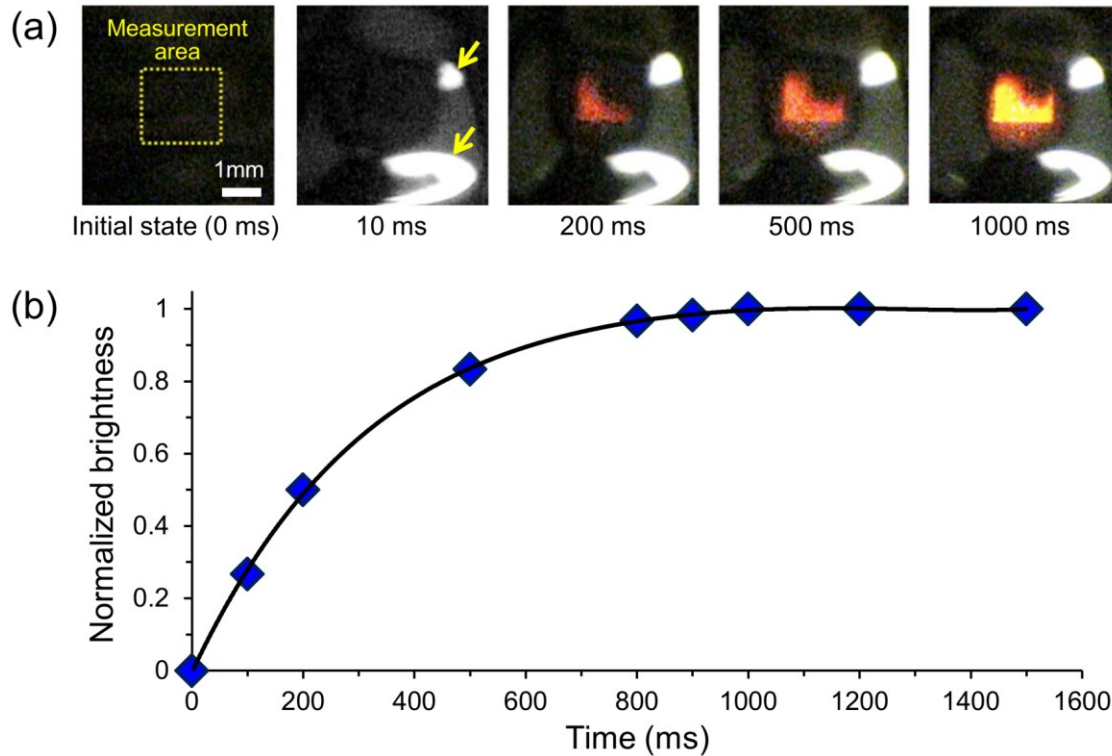


Figure 2.10: Measured temporal response of the ferrofluid with the single coil-mirror cell: (a) captured frames at different times (white spots indicated with arrows are due to light reflection on the deformed fluid surface); (b) measured brightness (average of three separate measurements) in the center region of the cell (normalized to the maximum value) vs. activation time.

activation. This fast thinning of the ferrofluid layer was followed by a relatively slow process of ferrofluid removal as was observed in Figure 2.5. The complete removal was measured to take approximately 1 s for this device. After 1 s, the fluid layer was stabilized and stationary until the current was turned off. This process can also be seen in Figure 2.10(b), which plots the brightness levels extracted from the individual frames. In addition, it was observed that a small amount of ferrofluid remained on the center of the coil (on the rectangle copper pattern in Figure 2.10(a)) when the fluid was repelled. Similar results can also be seen in Figure 2.11(a), Figure

2.12(a), Figure 2.12(b), and Figure 2.13(a). This phenomenon may be associated with the small peak of B that appears in the center of the coil, as seen in the reverse-mode case in Figure 2.1(b). The local peak of B on the center of the coil could hold some portion of the fluid on that location. However, this effect may be eliminated or minimized by optimizing the coil's design. The relatively long response time may be related to the boundary effect caused by the viscous shear force (F_v) that opposes the motion of the actuated ferrofluid, in addition to the large cell area and thickness of the ferrofluid layer used in the devices. Thus improvement in the temporal response may be approached through these aspects, i.e., decrease of the coil size and the initial fluid thickness, modification of surface properties of the mirror layer, and use of ferrofluids with lower viscosities [16], [21]. Surface modification by coating hydrophobic film (e.g., parylene) may also be incorporated to prevent any residual layer of the ferrofluid from remaining on the mirror surfaces when activated.

2.4.2.2 Dependence of Exposed Cell Area on Driving Current

The use of the reverse mode was observed to enable the control of the exposed mirror area on an activated cell by varying the driving current. Figure 2.11(a) shows the responses of a cell activated with three different amounts of current. It can be verified that the exposed area of the cell increased as the level of the current rose. This effect can be clearly seen in Figure 2.11(b) that shows the brightness profiles across the cell at the three current conditions (each plot is the average of three brightness profiles along the lines A-A' that were processed through a low-pass filter to remove the noise; this processing was also applied to the brightness data in Figure 2.12(c) and Figure 2.13(b) involved in the subsequent experiments). The result indicates consistent extensions of the reflective region towards the boundary of the cell with the current increase. It is understandable

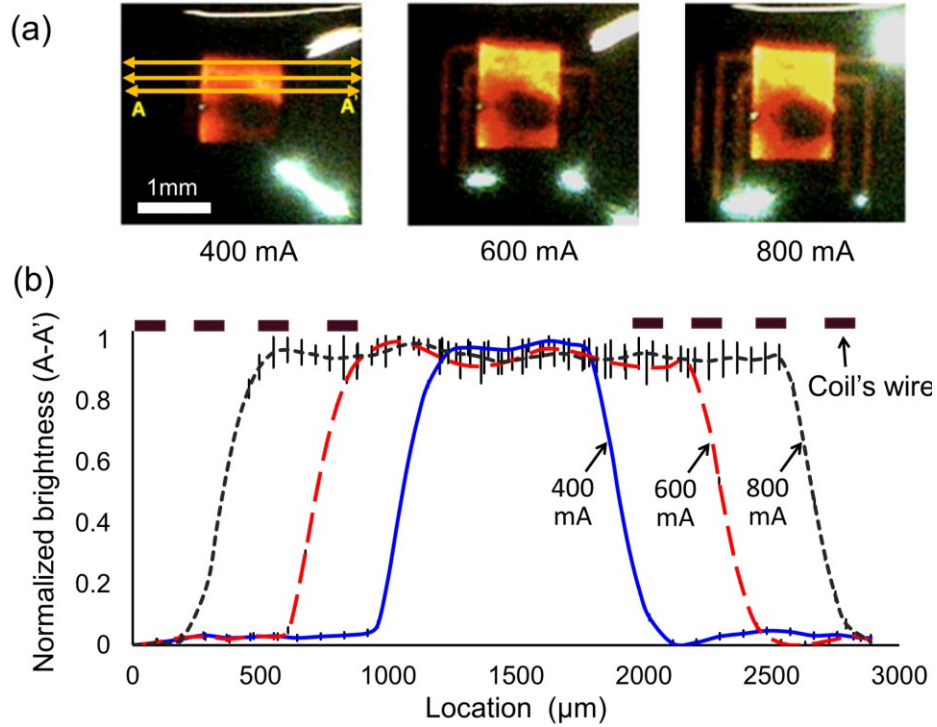


Figure 2.11: Removal of the ferrofluid on the single cell with varying driving current: (a) captured frames at three different levels of the current; (b) averaged and normalized plots of three low-pass-filtered brightness profiles measured along the three lines (A-A') at the three current levels. that the observed effect was associated with F_m that increased with the current (along with F_h), resulting in increased fluid volumes removed from the cell's surface.

2.4.2.3 Operation of Multiple Cells

The ferrofluid actuation was further characterized using the cell arrays. It was verified that the enhanced fluid actuation on a cell could be achieved by the activation of the adjacent cells along with the selective use of the forward/reverse operation mode.

This was demonstrated using the 3×1 device with two operation conditions. In one condition, the middle cell in the array was activated in the reverse mode while the two side cells were deactivated (Fig. Figure 2.12(a)). In the other condition, the two side cells were activated in the forward mode while the middle cell remained in the reverse mode (Figure 2.12(b)). The identical

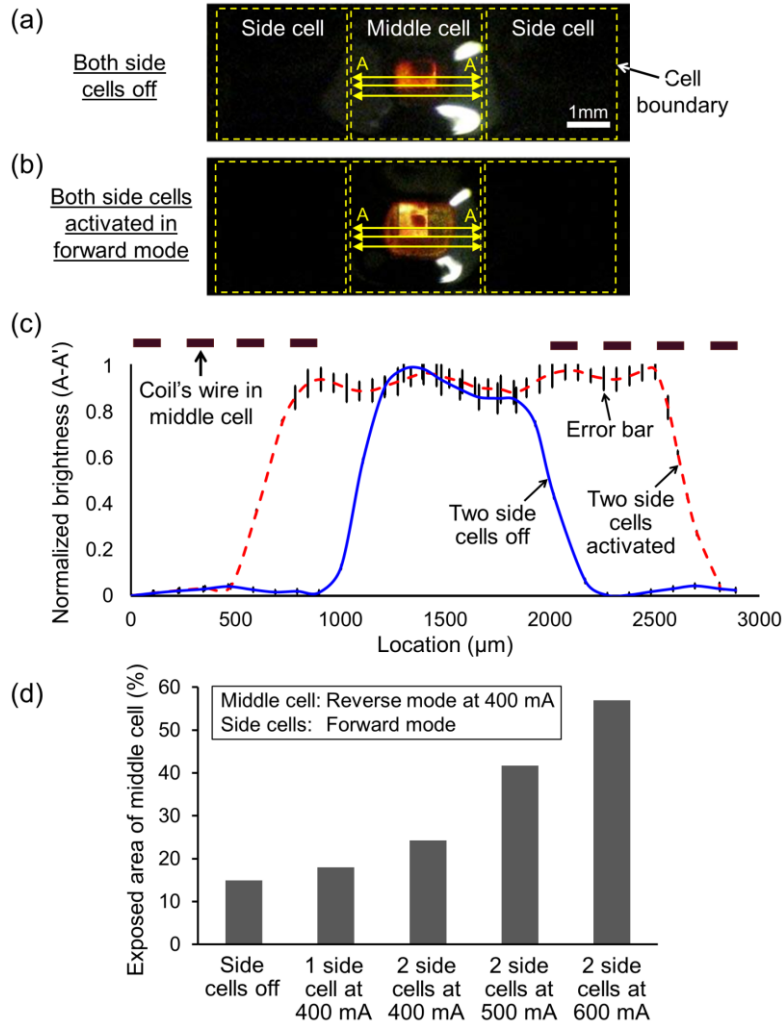


Figure 2.12: Enhanced ferrofluid actuation using adjacent cells: (a) ferrofluid condition when only the middle cell is activated in the reverse mode; (b) the condition when the two side cells are additionally activated in the forward mode; (c) averaged and normalized plots of three low-pass-filtered brightness profiles measure along the three lines (A-A') on the middle cell shown in (a) and (b) under the two conditions; (d) effect of the level of forward-mode driving current to the side cells on the exposed area of the middle cell in the reverse mode.

current level (400 mA) was used for all the activations. Comparing the two images in Figure 2.12(a) and Figure 2.12(b), it can be seen that more fluid was removed from the middle cell in the latter case so that the exposed area on the cell was increased.

This effect is also represented in Figure 2.12(c), the brightness profiles on the middle cell measured in the two conditions. This enhanced actuation resulted because each of the two side cells attracted the fluid when operated in the forward mode – this attraction force was combined with the force provided by the middle cell in the reverse mode that pushed the fluid to the side cells, effectively increasing the displacement of the fluid compared to the single-cell (middle-cell) activation case. The above effect may be exploited to increase the active area on a cell at a given individual driving current, or lower the current applied to a cell to achieve a certain active area on it, so as to achieve higher performance and/or efficient operation of the devices. Figure 2.12(d) shows the measurement results from further analysis in the effect of driving current to the two side cells in the forward mode on the exposed area of the middle cell in the reverse mode. It is evident from these results that, as expected, the exposed area consistently increased with the number of activated side cells, as well as with the driving current.

Figure 2.13(a) and Figure 2.13(b) show the fluid removal from all the three cells in the 3×1 device using the reverse mode for them, as well as the brightness profile over the device in that condition, presenting simultaneous exposures of the three mirrors in the array. The impact of the reverse-mode operation of the side cells with different conditions on the exposed area of the middle cell was characterized (Figure 2.13(c)). In contrast to Figure 2.12(d), the exposed area of the middle cell exhibited shrinkage as the number of activated side cells and the driving current to the side cells were increased. This result is consistent with the predictable phenomenon that the ferrofluid repelled in a side cell pushes back the ferrofluid repelled in the middle cell, reducing the exposed area on the middle cell, and that this effect is enhanced by activating more side cells and by increasing the current to the side cells. This cross-talk effect will need to be

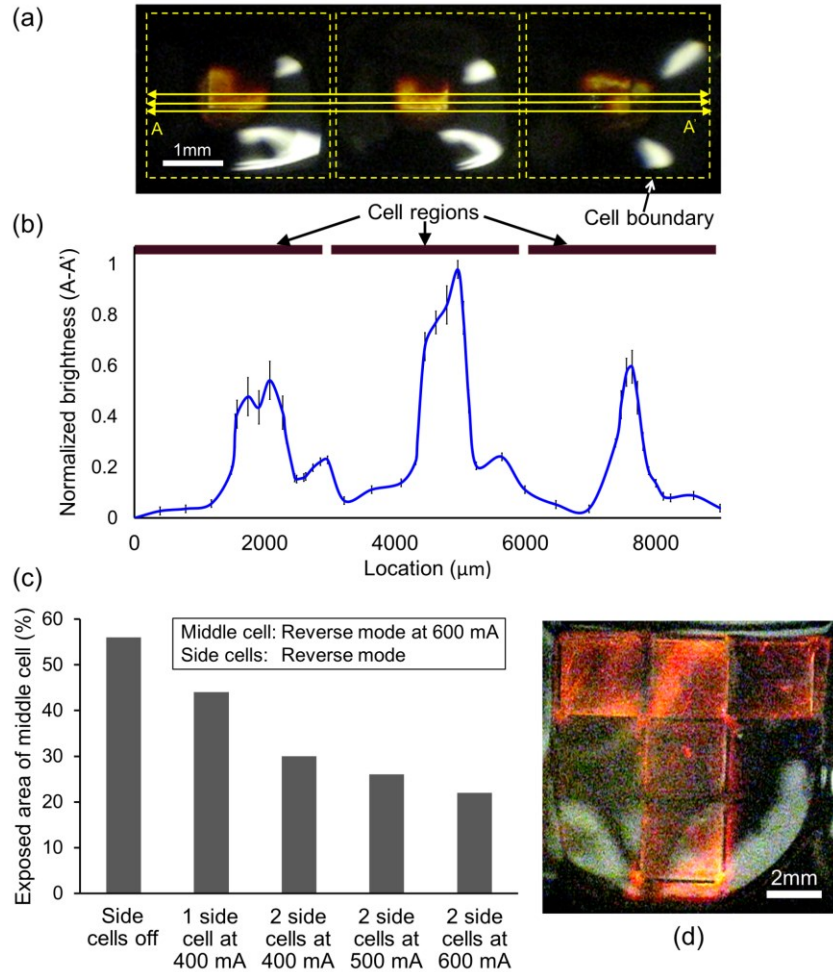


Figure 2.13: Simultaneous activation of multiple cells in the arrayed devices: (a) ferrofluid actuated on all the cells in the reverse mode in the 3×1 device; (b) averaged and normalized plots of three low-pass-filtered brightness profiles measured along the three lines (A-A') shown in (a); (c) effect of the level of reverse-mode driving current to the side cells on the exposed area of the middle cell in the reverse mode; (d) demonstration of letter ("T") formation using the 3×3 device.

considered as part of device design optimization. The experiment was extended to the operation of the 3×3 device. Displaying various patterns through the selective activation of the nine cells was successfully performed; Figure 2.13(d) shows an example that displayed a letter created by activating the corresponding cells in the reverse mode (the other cells were deactivated in this

test). These results demonstrate the feasibility of the developed technique for a variety of optical applications such as flat panel displays and optical switch/modulator arrays.

2.5 Conclusions

A new approach for ferrofluid actuation using planar coils with permanent magnets has been studied to achieve improved controllability in the fluid actuation. The use of bias fields in combination with the variable fields provided by the coils made it available to switch the polarity of the gradient of the field strength on each of the coils by selecting the orientation of the current passed through the coil. This field-gradient control enabled the bidirectional radial actuation of the ferrofluid. The actuation principle was experimentally verified using the arrayed active mirror devices designed and fabricated in this study. The dynamic characterization of the mirror-coil cell showed a fast initial response of the ferrofluid followed by gradual saturation after about one second. The activated area of each cell was shown to be controllable by adjusting the level of the driving current. Enhanced fluid actuation on an arbitrary cell could be implemented by the activation of the adjacent cells with selective use of the forward/reverse model. Multiple-cell control and pattern generation were successfully demonstrated. Future work encompasses the optimization and further miniaturization of the devices including the integration of permanent magnets with them towards the application to optical MEMS and imaging devices.

Chapter 3: Planar Variable Inductor Controlled by Ferrofluid Actuation²

3.1 Introduction

Integrated variable inductors have a broad range of applications, not only in RF circuits [48]–[52] but also in magnetic sensors [53], [54] and micromagnetic power devices such as dc/dc converters [55]. Different approaches including the use of actuators based on micro-electro-mechanical systems (MEMS) have been investigated in order to create discrete and continuous variable inductors. Discrete-value variable inductors have been developed using micro relays [49], [51] as well as integrated MOSFET switches [52] with limited tuning ability and applications. Various schemes for continuous variable inductors also have been developed. One common mechanism reported relies on displacing magnetic cores inside microsolenoids [55], [56] or metal pieces over planar coils [50], [57] to vary inductance without having particular actuation mechanisms. More integrated approaches have been reported to use displacements of planar coils or wires through electrostatic actuation [58], [59]; however, they are limited in dynamic ranges and/or need for high voltages (e.g. 150 V) for the actuation. Although electrothermal actuators have also been utilized to enable the actuation of inductive structures and vary their inductances [60], [61] they generally require larger power for operation. An interesting microfluidic approach that uses conductive liquid was recently reported to construct a variable inductor [62]; in spite of its wide tuning range, the device does not have an integrated pumping mechanism to actuate the liquid, posing implementation issues.

²Part of this chapter appeared in the following publications:

1. B. Assadsangabi, M.S. Mohamed Ali, and K. Takahata, “Planar Variable Inductor Controlled by Ferrofluid Actuation,” *IEEE Transactions on Magnetics*, 49 (4), pp. 1402-1406, 2013.
2. B. Assadsangabi, M.S. Mohamed Ali, K. Takahata, “Ferrofluid-Based Variable Inductor,” 25th IEEE Int'l Conf. Micro Electro Mechanical Systems (MEMS 2012), Paris, France, January 2012, pp. 1121-1124.

In this chapter, a new type of planar variable inductor based on the magnetic actuation of ferrofluid, is presented as a potential solution to the complexity and integration issues associated with the previous devices outlined above.

In the developed device, ferrofluid is used as a movable magnetic core that modifies permeability distribution on a planar spiral-coil inductor. Figure 3.1 schematically shows the device configuration. Ferrofluid in the reservoir created on the inductor is displaced using magnetic-field gradients produced by another planar coil (actuation coil) that is aligned to the inductor. A bias magnetic field is used to uniquely enable repelling of the fluid from the inductor, instead of attracting to it, which is found to significantly enhance the tuning range of the inductor. In this chapter, first design and fabrication of the variable inductor is presented followed by the characterization results of the fabricated prototype.

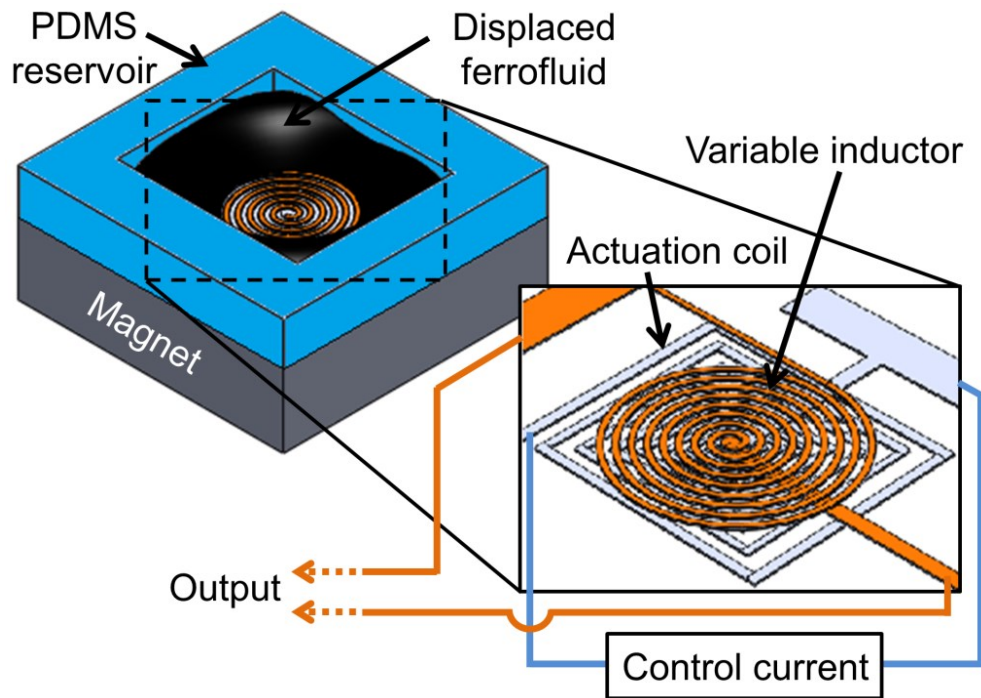


Figure 3.1: Configuration of the ferrofluid-based variable-inductor device.

3.2 Device Design and Fabrication

The variable inductor investigated in this study is operated by controlling the ferrofluid displacement over the planar inductor surface using the bidirectional actuation mechanism discussed in Chapter 2, which in turn controls the spatial distribution of the permeability on the inductor and thus modifies the inductance. Both actuation modes cause certain levels of modification in the ferrofluid profile and the inductance. Since the magnitude and gradient of B , or F_m acting on the ferrofluid, directly depends on the amount of the driving current supplied to the actuation coil, this principle can be used to achieve continuous variation of inductance of the planar inductor.

To characterize and demonstrate the ferrofluid-based variable inductor, a proof-of-concept device was developed. Figure 3.2 shows the device design and the dimensions of the coils. The

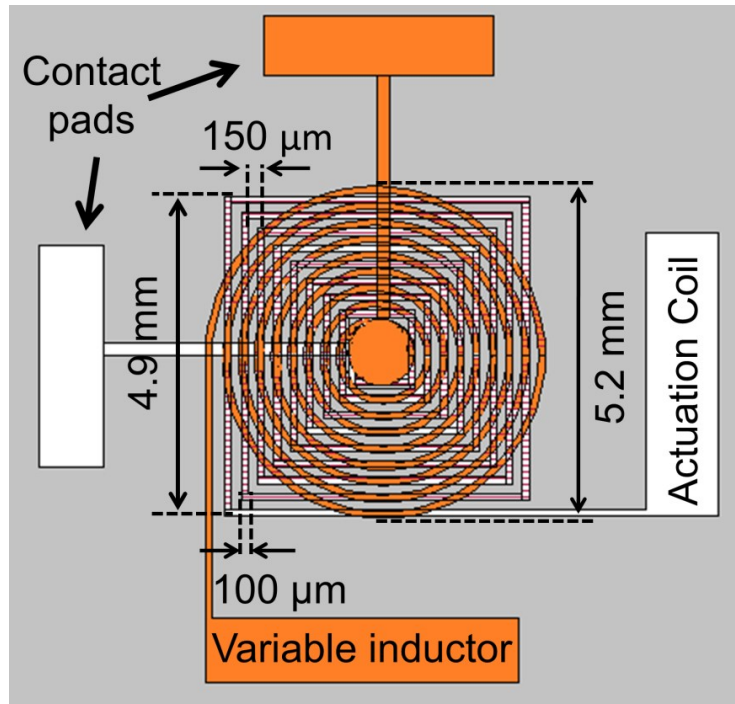


Figure 3.2: Top view of the device design showing the variable inductor (circular spiral) and the actuation coil (square spiral). PDMS reservoir is not shown.

variable inductor and the actuation coil were chosen to have circular and square patterns with the same number (i.e. 9) of turns. The variable inductor is located above the actuation coil to make a direct contact with ferrofluid that is stored in the PDMS reservoir fabricated on top of the inductor. The device is fabricated using single-sided copper-clad polyimide (PI) film with 50- μm thickness (G2300, Sheldahl Co., MN, USA) as the substrate (Figure 3.3). In this process, the Cu-clad layer with 5- μm thickness is used to pattern one of the contact pads and its lead. The spiral coils used as the variable inductor and the actuation coil are separately formed by Cu electroplating in the molds photo-patterned in a dry-film photoresist (PM240, DuPont, NC, USA) laminated on the PI side of the film (Figure 3.3 (steps 1-3)). A liquid PI (HD-4010, HD Microsystems, DE, USA) is spin coated on the actuation coil, which is then aligned and bonded to the backside of the variable inductor by curing the PI. A 130- μm -thick mold to form the walls of PDMS reservoir is created on the substrate by patterning three layers of spin-coated photoresist (SPR 220-7, Rohm and Hass Co., PA, USA). After forming the walls and dissolving its mold, the reservoir formation is completed by bonding a separately prepared PDMS cap layer to the molded walls using a O_2 -plasma bonding technique [63]. Prior to the bonding, the cap layer is mechanically punched to create two holes for ferrofluid injection into the reservoir. It was observed that the oil-based ferrofluid (EFH1, Ferrotec Co., NH, USA) used in this study caused swelling of PDMS. To prevent this swelling, a polyvinyl-alcohol protective layer is formed on the inner surfaces of the PDMS reservoir by injecting a 4 wt% aqueous solution of PVA into the reservoir and then dried out to form a thin layer of PVA on all the inner surfaces of the reservoir. Finally, a ferrofluid is injected into the reservoir to complete the fabrication. Figure 3.4 shows a sample device fabricated through the developed process (prior to ferrofluid injection).

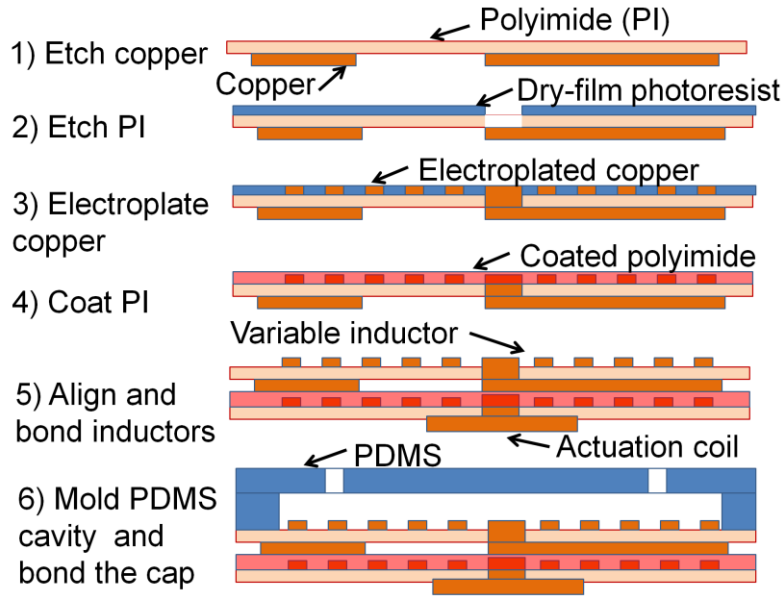


Figure 3.3: Fabrication process.

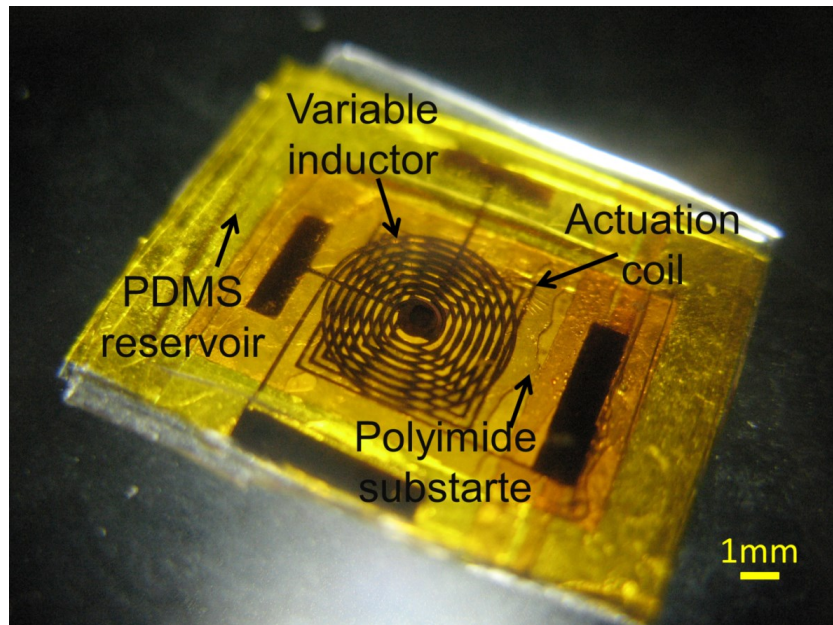


Figure 3.4: A sample of the fabricated device (prior to ferrofluid injection).

3.3 Experimental Results and Discussions

The static and dynamic behaviors of the fabricated devices were characterized using an experimental set-up, in which the actuation coil was connected to a power supply to provide a

current to it, and the variable inductor was coupled with a spectrum-impedance analyzer (Agilent 4395A) for its electrical measurements. A permanent NdFeB magnet (K&J Magnetics Inc., PA, USA) was placed underneath the device to provide a constant biasing field. The distance between the magnet and the coil was set to be ~ 8 mm, which was the shortest distance to prevent non-uniform patterns on the fluid's surface (so-called the normal-field instability [8]) for the particular magnet used. The B level of the provided bias field at the location of the device was measured to be approximately 10 mT.

The device response was first characterized without the ferrofluid by varying the driving current, due to any potential influence from the actuator coil to the variable inductor, and observed no

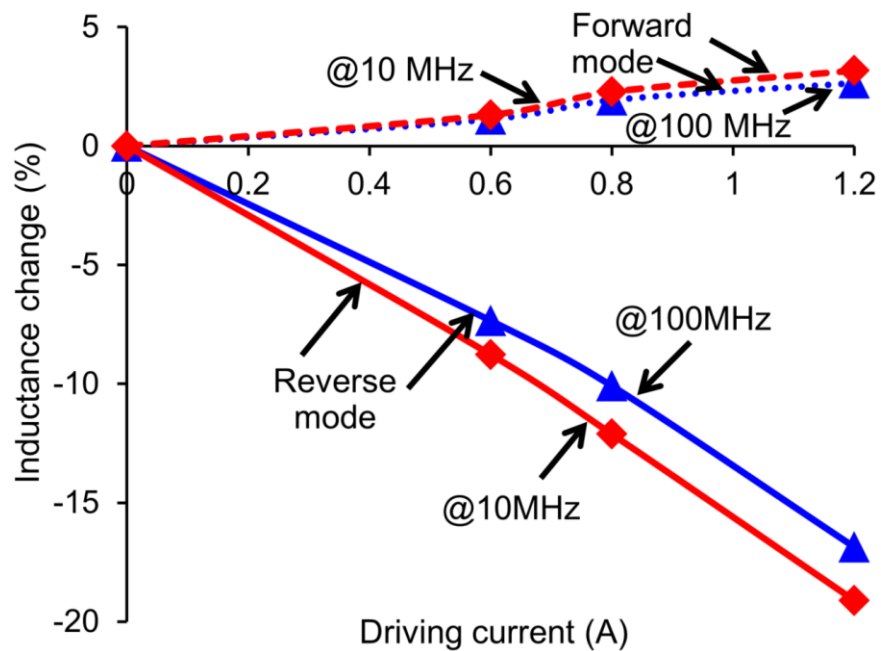


Figure 3.5: Inductance changes measured at 10 MHz and 100 MHz for the operations in the forward and reverse modes.

noticeable change in the inductance. Following this verification, the response of the ferrofluid-loaded device to the driving current was compared in the two (forward and reverse) operation modes. Figure 3.5 shows the average values (each from two measurements) of inductance

changes measured at 10 MHz and 100 MHz for both modes. As can be seen in the graph, the inductance increases with the current in the forward mode whereas it decreases in the reverse mode. The former case can be explained by the fact that the ferrofluid, a magnetic medium, is accumulated in the central area of the coil, which increases the local inductance in the area but decreases that in the other (periphery) region as the amount of the ferrofluid in the region decreases because of the accumulation in the center part; however, since the outer turns of a planar coil make less contribution to the formation of a magnetic field than its inner turns [64], the impact of the inductance reduction in the periphery on the overall inductance of the device is smaller than that of the inductance rise in the central area, collectively resulting in an increase of the total inductance. The reduction of the overall inductance in the reverse mode can be explained similarly, in a manner opposite to the above case.

A notable characteristic indicated in Figure 3.5 is that the reverse mode exhibits a significantly larger response than the forward mode; at 100 MHz, for example, the inductance sensitivity to the driving current in the reverse mode is ~ 135 ppm/mA, approximately $6.1\times$ greater than the sensitivity in the forward mode. This result is evidently associated with the phenomenon observed in reverse mode, where the repelling effect caused the exposure of the inner turns of the inductor to air, a medium with a much lower permeability than the ferrofluid (by a factor of ~ 2.6), strongly reducing the inductance in the exposed region. This region extended as the driving current increased – Figure 3.6 displays this observation, showing gradual extension of the exposed region with the current (up to 1.2 A) until reaching the entire area of the inductor. This result suggests that the reverse mode allows one to control the ferrofluid position over the variable inductor, or the number of the coil turns covered by the ferrofluid, by adjusting the driving current. In the forward mode, in contrast, the exposure of the coil surface (on its

periphery) was not observed with any current level tested. Due to the large difference in permeability between the ferrofluid and air, it can be expected that the inductive change led by the variation in the exposed area seen in the reverse mode is larger than the change only led by the variation in thickness of the ferrofluid while it still covers the entire area of the inductor, the case in the forward mode, which may be the main mechanism of the difference in the inductance change between the forward and reverse modes. One possible reason that no exposure occurs in the forward mode may be related to effect of surface tension involved in the reservoir walls

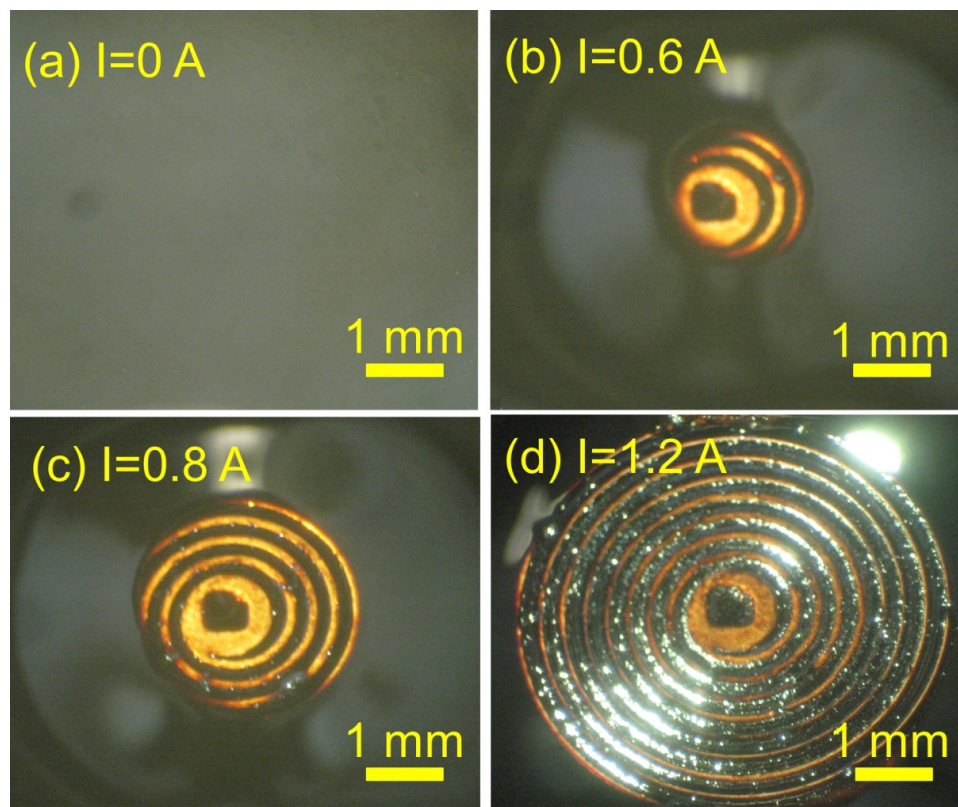


Figure 3.6: Optical images of the variable inductor operated in the reverse mode at different driving currents showing varying displacements of the ferrofluid and exposed areas of the inductor.

(located outside of the coils), which can act against the fluid motion in the forward mode, leading to less fluid displacement compared with the reverse-mode case in which the surface

tension can assist the fluid motion as discussed in section 2.3 in chapter 2. Another potential reason is that the surface area that attracts the fluid is smaller in the forward mode (the central region of the coil) than in the reverse mode (the periphery region), thus the reduction in the fluid thickness may be smaller in the forward mode.

The dynamic responses of the device were also characterized and compared between the forward and reverse modes, which are shown in Figure 3.7(a) and Figure 3.7(b), respectively. In each mode, the driving current was increased stepwise every 5 seconds while measuring the transient time to change the inductance level. As can be seen from the comparison, the forward-mode operation responds much faster than the reverse-mode case however, this feature is available at a cost of smaller tuning range of the inductance. This outcome is consistent with the result in section 2.2 of chapter 2 where it was shown that reverse mode operation includes a fast response due to magnetic force as well as a slower one as a result of thermocapillary effect on the fluid. Therefore, the accumulative effect in this mode is achieved in a longer time compared to forward mode case where magnetic attraction force is the dominant effect (as mentioned in section 2.2) and responsible for the inductance change. Focusing onto the advantage in the tuning range, we further characterized the device operated in the reverse mode for its frequency dependence using the spectrum-impedance analyzer. The measurement results displayed in Figure 3.8(a) clearly show, as predicted, consistent decreases of inductance with the driving current. Figure 3.8(b) shows measured Q factors, indicating the maximum value of the maximum value of 23 at ~60 MHz upon the complete removal of the ferrofluid from the inductor (at 1.2 A). The tuning range and the self-resonant frequency of the inductor were measured to be 16% (at 60 MHz with the maximum Q factor) and ~350 MHz, respectively.

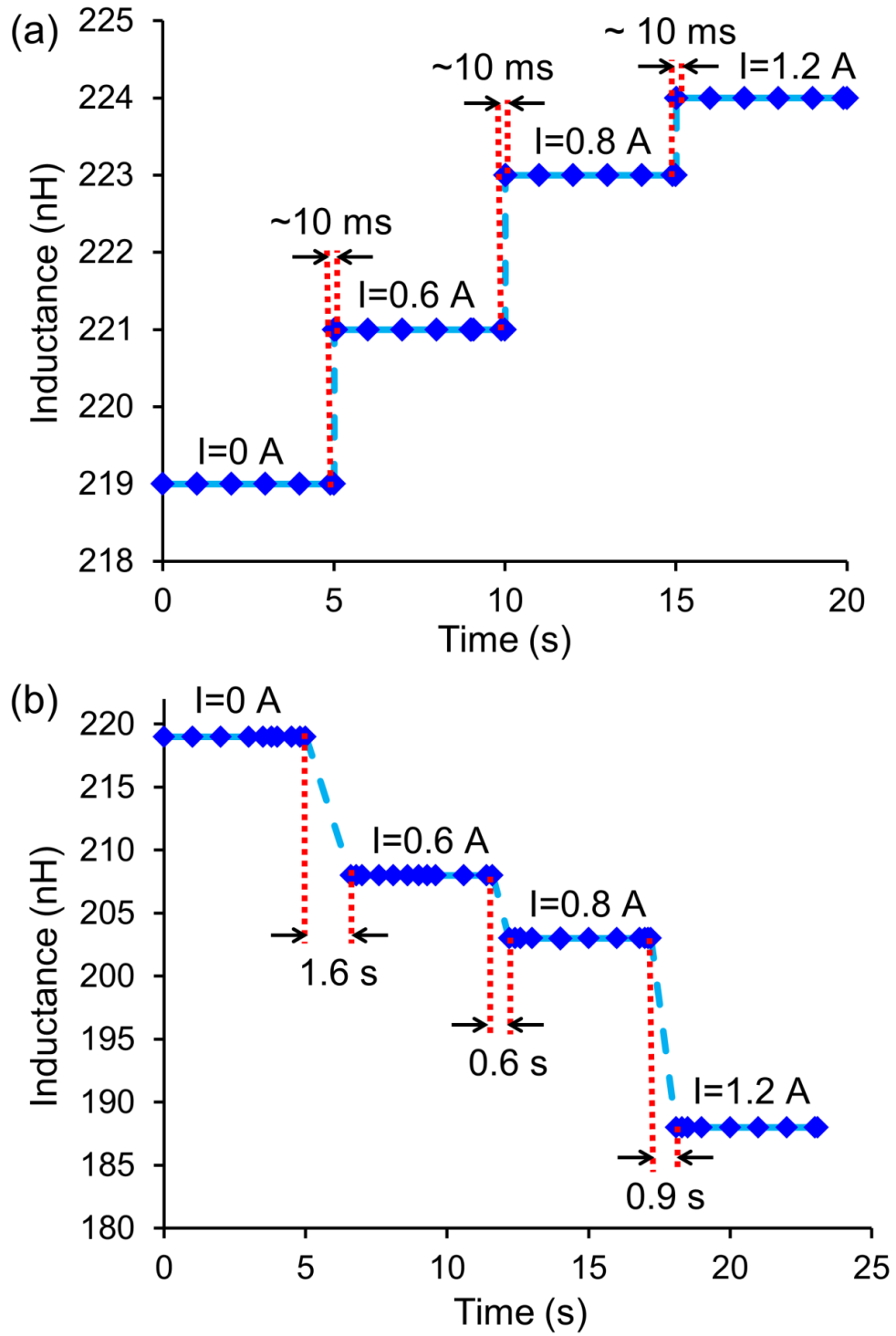


Figure 3.7 Measured temporal response of inductance (at 10 MHz) of the device operated in (a) forward and (b) reverse mode at different driving currents.

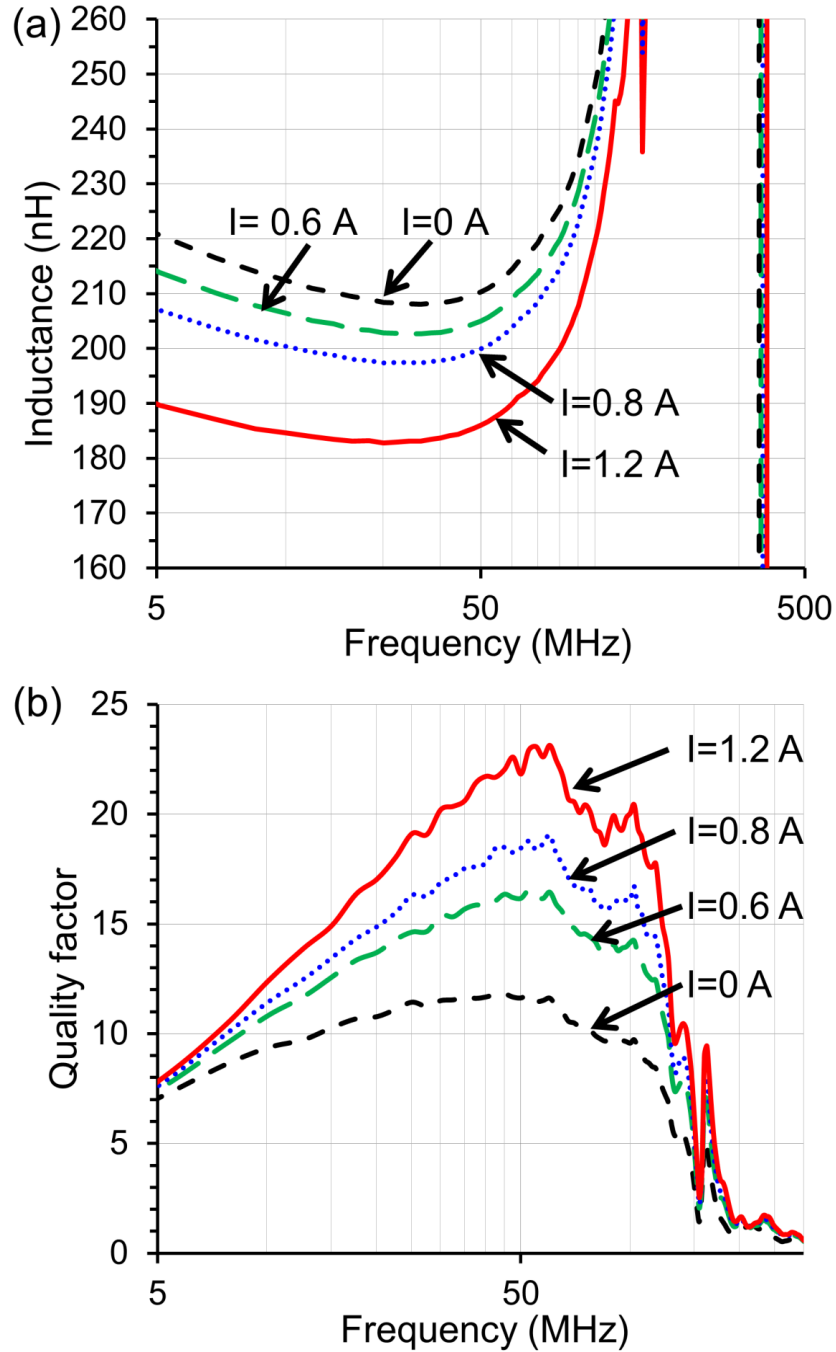


Figure 3.8: Measured frequency dependence of (a) inductance and (b) Q factor of the device operated in the reverse mode at different driving currents.

The Q factor was measured to increase with the current, (i.e., displacement of the ferrofluid) as shown in Figure 3.8(b). If we assume a typical inductor model represented by a series

combination of the inductance (L) and its parasitic resistance in parallel with the parasitic capacitance (C_p), the Q factor of the inductor is proportional to the square root of L/C_p . As the fluid is removed from the inductor surface, L decreases; however, C_p also decreases as the dielectric constant of ferrofluid is much larger than that of air [65]. These may suggest that the decrease of C_p is more dominant than that of L in the observed increasing trend of Q factor.

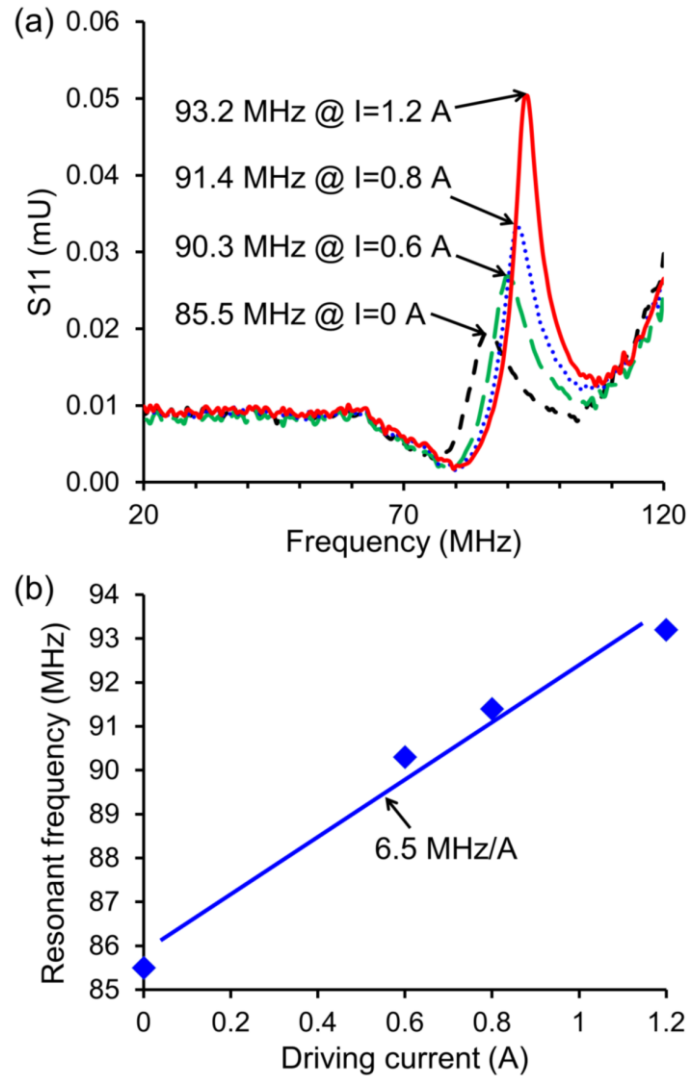


Figure 3.9: Wirelessly measured resonances of the L-C tank formed using the fabricated variable inductor, showing (a) the frequency modulation with the driving current in the reverse mode, and (b) the resonant frequency vs. the driving current.

As another experiment toward the application for tunable filters, the device was coupled with a discrete capacitor (9.8 pF) to form an inductor-capacitor (L - C) tank, in which the resonant frequency of the tank was defined by the level of the variable inductance, i.e., ferrofluid displacement. The resonance of the tank was wirelessly sensed using an external coil that was inductively coupled with the variable inductor. The measurement result shown in Figure 3.9(a) demonstrates the modulation of the resonant frequency with the input current to the actuation coil. Figure 3.9(b) re-plots the measured frequency shifts as a function of the current, suggesting a frequency response to the input current of 6.5 MHz/A and a corresponding sensitivity of 76 ppm/mA.

3.4 Conclusion

A micropatterned planar variable inductor that is operated with controlled actuation of ferrofluid has been studied. The ferrofluid actuation was enabled by the magnetic field provided by another planar coil in combination with a bias field, which allowed repelling motions of the fluid from the inductor in the reverse-mode operation. This mode of operation was found to offer substantially larger inductance variations compared with the forward-mode case. The continuous modulation of the inductance with its tuning range of 16% was demonstrated with the fabricated device operated in the reverse mode. Frequency tuning was also demonstrated using an L - C resonant tank constructed using the developed variable inductor. For the operation in the reverse mode, a combinational use of the forward-mode operation, to actively pull the fluid back to the central area of the inductor, may be effective to enable faster modulation. In addition to potential applications in electrical/electronic circuits, the simple and integrated operation concept of the device may provide a path to improve various ferrofluid-based sensors [53], [54] in their

performance and sizes. Future work will encompass further miniaturization and performance improvement including operation frequency and power consumption.

Chapter 4: Electromagnetic Microactuator Realized by Ferrofluid-Assisted Levitation Mechanism³

4.1 Introduction

It was mentioned in Chapter 1 that as ferrofluid is applied onto a permanent magnet, it accumulates on the poles areas and as a result of generated magnetic pressure in the fluid, magnet is lifted above the substrate. The ferrofluid layer essentially acts as a self-sustained lubricant and bearing that physically follows the magnet as it moves, realizing smooth motions of the magnet with minimal frictions.. Therefore, one promising ferrofluid application is for microbearing purpose in the moving magnet based microactuators, however, literature review shows no integrated microactuator that has exploited this capability in its operation.

There are studies that exploit the ferrofluid levitation of permanent magnets [46], [66], however, these efforts use magnetic means external to the device packaging to move the magnet. That is, another permanent magnet, or electromagnet, is externally moved to drag the magnet supported on the ferrofluid with it. Moreover, there is little information on the characteristics of ferrofluid based microbearing such friction force and load carrying capacity.

In this chapter, an integrated electromagnetic linear micromotor is designed, fabricated, and characterized. The device incorporates microfabricated planar spiral coils that provide necessary electromagnetic forces to actuate the magnet slider levitated by ferrofluid along the coil array (Figure 4.1).

³ Part of this chapter appeared in the following publications:

1. B. Assadsangabi, M.H. Tee, and K. Takahata, "Ferrofluid-Assisted Levitation Mechanism for Micromotor Applications," 17th IEEE Int'l Conf. on Solid-State Sensors, Actuators and Microsystems (Transducers 2013), Barcelona, Spain, 2013, pp. 2720-2723.
2. B. Assadsangabi, M. H. Tee, and K. Takahata, "Electromagnetic Microactuator Realized by Ferrofluid-Assisted Levitation Mechanism", Journal of Microelectromechanical Systems. (Published online on Feb 26th 2014; DOI: 10.1109/JMEMS.2014.2305112)

The operation principle, design and simulation using finite-element analysis (FEA), fabrication process, and characterization and testing results of the developed device are discussed in the following sections.

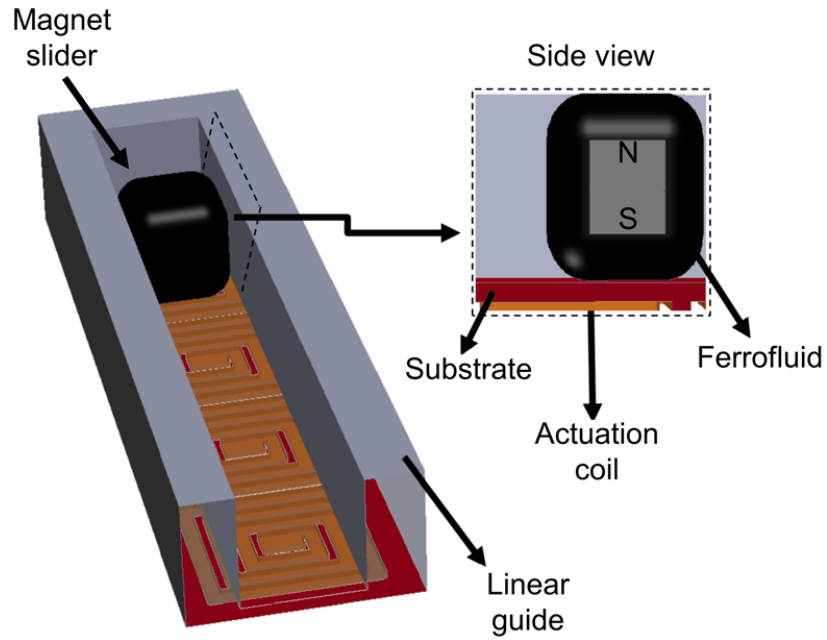


Figure 4.1: Schematic diagram of the electromagnetic linear micromotor based on the ferrofluid bearing.

4.2 Working Principle and Analysis

When ferrofluid is applied onto a permanent magnet, it accumulates around the poles and develops a static pressure inside the fluid as noted earlier. The pressure generated in the ferrofluid, p_m , can be expressed as [67]:

$$p_m = \mu_0 \int_0^H M_f dH \quad (4.1)$$

where μ_0 is the magnetic permeability of free space, H is the magnetic field intensity provided by the magnet, and M_f is the magnetization of the ferrofluid caused by the field. Under the

assumption that the accumulated ferrofluid is saturated (i.e., $M_f = M_{fs}$ where M_{fs} is the saturation level of a selected ferrofluid, a likely condition for the proposed configuration with typical permanent magnets), the expression is simplified to:

$$p_m = \mu_0 M_{fs} H \quad (4.2)$$

An accurate calculation of p_m requires the information on the distribution of H on the magnet and can be complicated even for simple geometries [68]. For an approximate analysis on the level of p_m generated in the ferrofluid, the following example is considered. Using a ferrofluid with a saturation magnetization ($\mu_0 M_{fs}$) of 44 mT and a permanent magnet that generates a maximum magnetic flux density ($\mu_0 H$) of 500 mT (these are the actual values involved in the materials to be used in the experiments discussed later), p_m is estimated to be 17.5 KPa

For a 1.6mm cubic magnet with a weight of 40 mg (also to be used in the experiments), assuming that p_m is uniformly distributed over the magnet surface, this pressure translates to a levitation force of 44.8 mN that is applied to the magnet. Since H (and thus p_m) within the ferrofluid decreases with the distance from the magnet surface, the above force level is a somewhat overestimated value but in a range similar to the actual levitation forces measured as will be shown later in Section 4.4.1. This level of force is orders of magnitude larger than the gravitational force (0.4 mN) acting on the magnet. Therefore, the levitation force can support not only the magnet itself but also an additional load exerted on the magnet. This levitation mechanism is applied to the electromagnetic linear micromotor (Figure 4.1) proposed in the preceding section.

Figure 4.2 schematically shows the magnet motion that is caused by the magnetic field produced by a single planar coil. The magnet is attracted towards the coil center when a current applied to the coil results in the opposing polarity to the magnet polarity that faces the coil (Figure 4.2(a)).

In contrast, the magnet is repelled from the coil when the current direction is reversed (Figure 4.2(b)). The force density generated on the magnet, \vec{F} , can be described as [28]:

$$d\vec{F} = \nabla(\vec{M} \cdot \vec{B}) \quad (4.3)$$

where \vec{M} is the remnant magnetization vector of the magnet and \vec{B} is the magnetic flux density.

Assuming that the magnet has a constant magnetization along the direction normal to the coils (z), i.e., $\vec{M} = M_0\vec{z}$ where M_0 is the inherent magnetization of the magnet, integrating Eq. (4.3)

over the magnet volume, V , provides the x component of the force acting on the magnet as:

$$F_x = \int_V \mu_0 M \frac{\partial H_z}{\partial x} dV \quad (4.4)$$

where H_z is the normal component of magnetic field intensity. Eq. (4.4) suggests that the magnitude of the force is dependent on the field gradient determined by the actuation coil as well as on the magnetization and volume of the magnet. The direction of the force is dictated by the

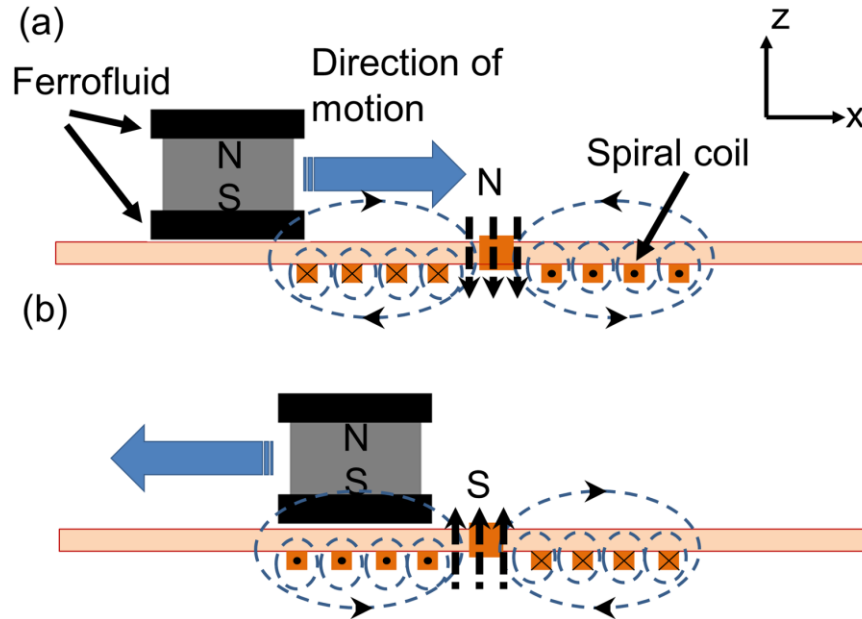


Figure 4.2: Ferrofluid-levitated magnet in (a) attracting and (b) repelling modes of actuation over a planar coil controlled by switching the direction of the coil current.

polarity of the field gradient, which can be switched simply by changing the direction of the current that the coil is energized with.

To assess the magnet’s response to the magnetic field generated by a planar coil, three-dimensional FEA was performed using COMSOL Multiphysics V 4.3. Table 4-1: Specifications for the finite element model of the planar spiral coil shows the specifications of the coil used in the model. (These specifications represent the design of the actual device as discussed later.) A relatively large current (1 A) was used to clearly visualize relevant effects in the simulation.

Table 4-1: Specifications for the finite element model of the planar spiral coil

Parameter	Value
Coil’s wire width / spacing / thickness	100 μm / 150 μm / 20 μm
Number of turns	4
Overall size	2.4 mm
Applied current	1A

Figure 4.3 shows the z component of the magnetic field intensities at three different elevations, 200 μm , 400 μm and 800 μm from the surface of the spiral coil in which the current flows in the counter-clockwise direction (as viewed from the top of the coil). It can be seen that the magnetic field has the main peak that appears at the central area of the coil as well as minor peaks with the opposite polarity near the periphery of the coil. The polarities of these peaks are reversed when the current direction is made clockwise. As the coil center exhibits the largest peak of the field intensity, this location serves as the main equilibrium position that attracts or repels the magnet depending on the polarity of the magnet and the direction of the current (e.g., for the setting shown in Figure 4.2(a), attraction is achieved with a counter-clockwise current). The coil

periphery can also serve as another equilibrium location for the magnet due to the minor peaks of the field. When the magnet is repelled from the center of the coil (using a clockwise current), it can either be trapped at the coil periphery due to the opposite polarity of the minor peak at that location or pass through the periphery and escape from the coil, depending on the elevation level of the levitated magnet and also on the level of the coil current (e.g., no periphery trapping due to small/no field peak at higher elevation levels and/or due to a fast repulsive motion from the coil center when the current is large).

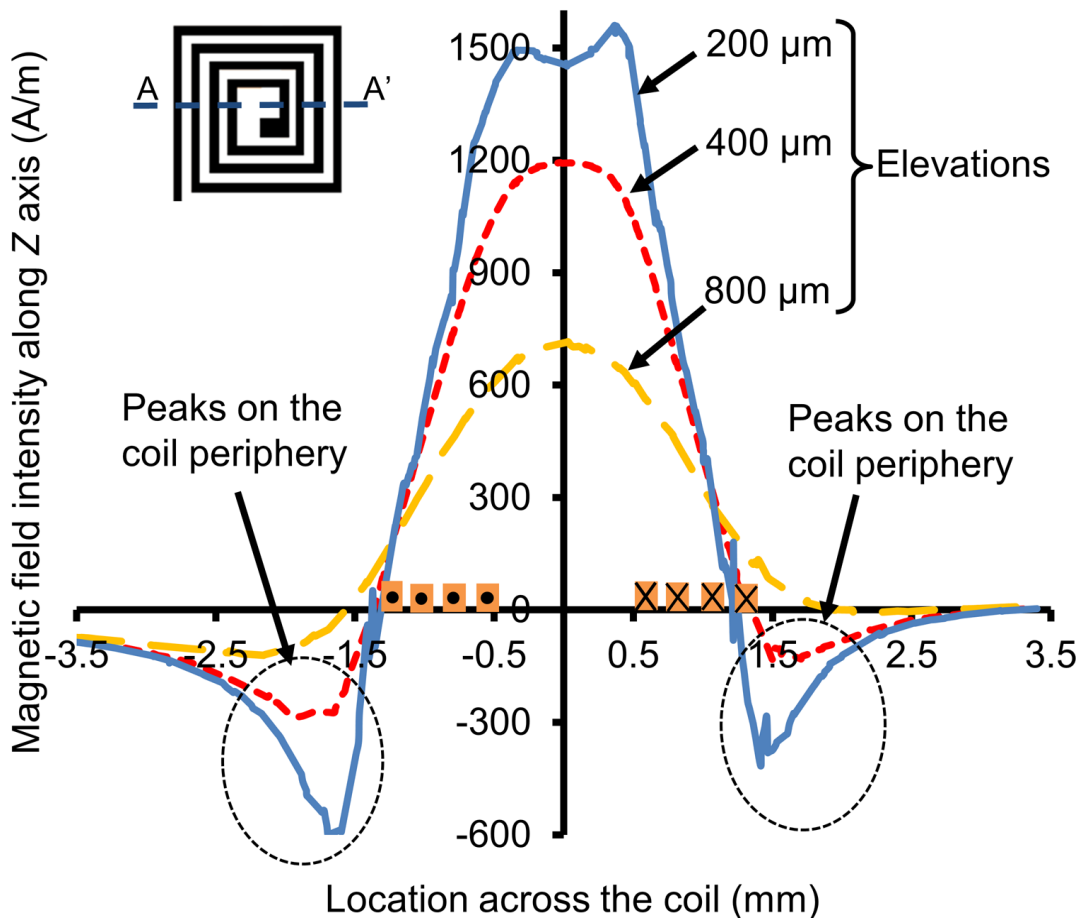


Figure 4.3: Normal component of the magnetic field generated by the planar coil at different elevations from the coil along the A-A' line indicated in the inset showing the coil pattern.

4.3 Design and Fabrication

To demonstrate and characterize the linear actuator discussed above, a proof-of-concept device shown in Figure 4.4 was fabricated. In the device, an array of micropatterned spiral coils with a linear guide serves as the rail track for the ferrofluid-levitated magnet slider to be actuated along the array. The planar coils have an identical spiral pattern with an overall size of 2.4 mm (detailed dimensions are indicated in Figure 4.4). These coils also have separate contact pads so that each of the coils can be individually powered. A commercially available oil-based ferrofluid (EFH1, Ferrotec Co., NH, USA; relative magnetic permeability of ~ 2.6 ; this choice of ferrofluid is discussed in 4.4.1) is applied onto a NdFeB permanent magnet with a 1.6 mm or 3 mm cubic shape (K&J Magnetics Inc., PA, USA; surface field ~ 500 mT) until the magnet is levitated above the substrate.

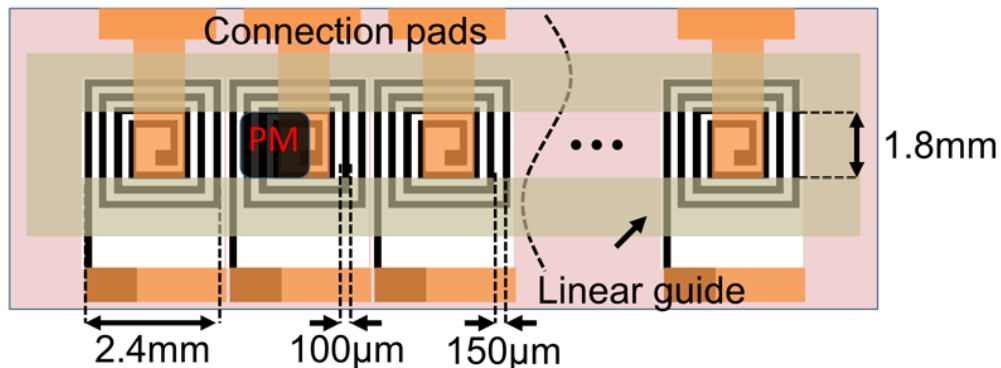


Figure 4.4: Top view of the device design, showing the levitated magnet (PM) located on an array of the planar coils with its linear guide.

The rail-track component was fabricated using single-sided Cu-clad polyimide (PI) film with a thickness of $50 \mu\text{m}$ (G2300, Sheldahl Co., MN, USA) as the substrate through the process shown in Figure 4.5. The Cu-clad layer with a thickness of $5 \mu\text{m}$ on the film was used to pattern the contact pads (Figure 4.5(a)). The spiral coils were formed by Cu electroplating for a thickness of

~20 μm in the molds of a photo-patterned dry-film photoresist (PM240, DuPont, NC, USA) laminated on the PI side of the film (Figure 4.5(b) and Figure 4.5(c)). The linear-guide part was fabricated by water-jet cutting of a PMMA sheet, which was then aligned and bonded to the

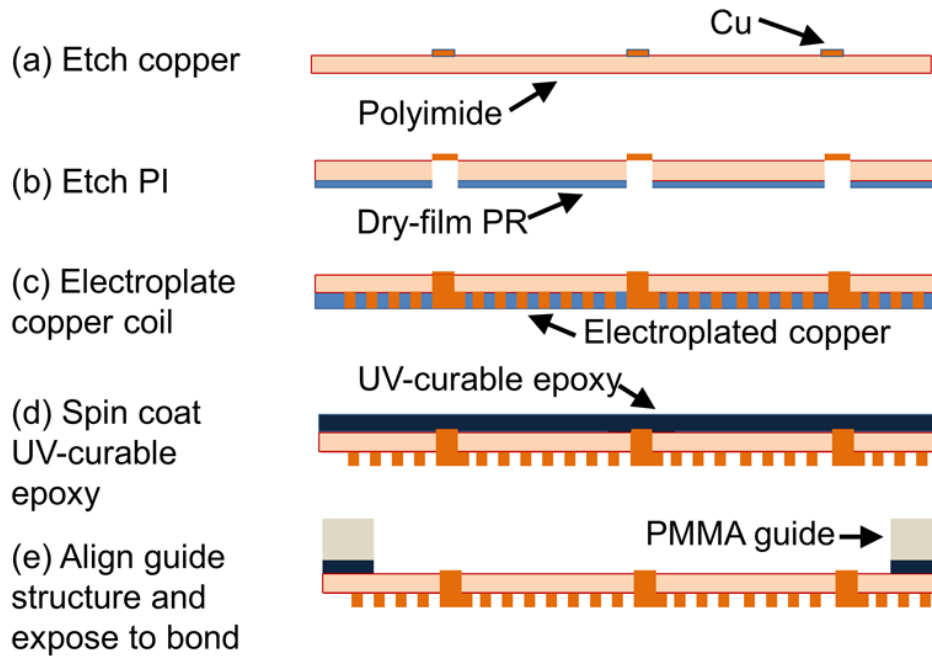


Figure 4.5: Fabrication process for the electromagnetic rail track.

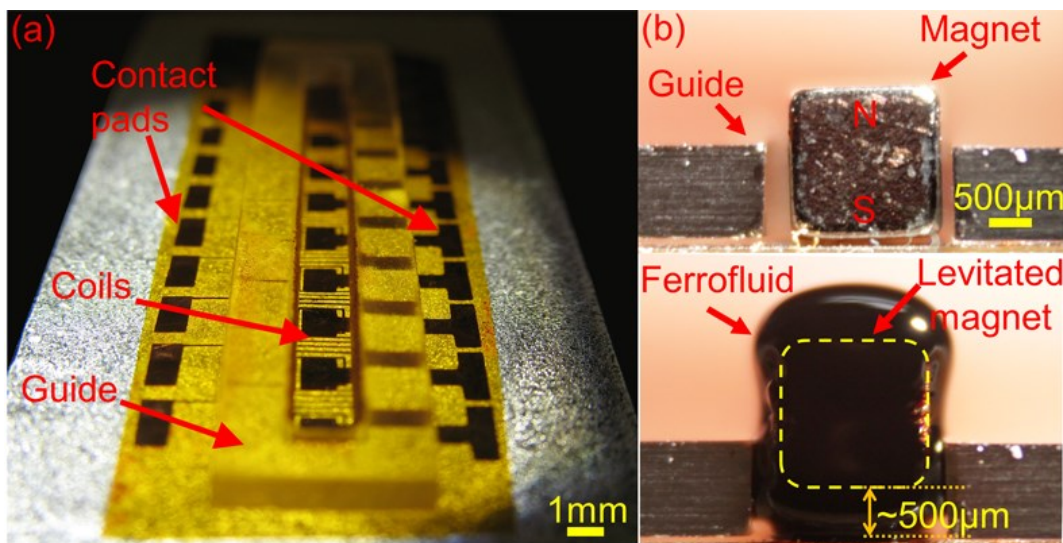


Figure 4.6: (a) Fabricated sample device and (b) NdFeB magnet without ferrofluid (upper) and with the fluid (bottom) showing a levitation gap of ~500 μm

substrate. The bonding step was performed using a UV-curable epoxy (U305, Cyberbond, IL, USA) spin coated on the substrate prior to bonding, by exposing the coated epoxy to UV light through a photomask (Figure 4.5(d) and (e)). The uncured portions of the epoxy were removed using isopropanol alcohol, followed by rinsing with deionized water. Figure 4.6(a) and Figure 4.6(b) show a sample device fabricated through the process described above and close-up images of the 1.6 mm magnet levitated with ferrofluid in the linear guide, respectively. The levitation height was observed to be $\sim 500 \mu\text{m}$ for the 1.6mm magnet (Figure 4.6). The amount of the ferrofluid required to reach this state was approximately $1 \mu\text{L}$.

4.4 Experimental Results and Discussion

4.4.1 Frictional and Levitation Force of Ferrofluid Bearing

The friction force involved in ferrofluid bearing is an important parameter that impacts on the actuation performance. To quantify this parameter, the 1.6 mm magnet levitated by ferrofluid on the coil substrate was placed on a tilting stage, and the minimum angle that caused the magnet to start moving down was recorded. This evaluation was performed for two types of commercially available ferrofluids, A-300 (Sigma Hi Chemicals Inc., Kanagawa, Japan) and EFH1. Table 4-2 summarizes key properties of these ferrofluids and the results from the tilt test. The results suggest that EFH1 with a lower viscosity level exhibited a smaller threshold angle, i.e., a smaller friction effect compared with A-300. The friction force, $F_{friction}$, is estimated to be $\sim 14 \mu\text{N}$ for EFH1 based on the recorded threshold angle. As also shown in Table II, EFH1 has a higher saturation magnetization ($\mu_0 M_{fs}$) and, thus, is expected to provide a higher level of p_m or the levitation force than A-300 as suggested by Eq. (4.2). Based on these conditions, EFH1 was used for further experimental analysis.

The lifting force provided by the ferrofluid bearing was first characterized to evaluate the load carrying capacity of the magnet slider. For this measurement, the EFH1 ferrofluid was applied onto the 1.6 mm magnet until the magnet was levitated with an approximate distance of 450 μm from the substrate surface. The repulsive force exerted by the ferrofluid bearing was recorded

Table 4-2: Material properties and tilt test results for two type of ferrofluids

Ferrofluid (Carrier liquid)	Saturation magnetization	Viscosity	Measured tilting angle
A-300 (Alkylnaphthalene)	34 mT	300 cp @20 °C	7°
EFH1 (Light hydrocarbon)	44 mT	6 cp @27 °C	2°

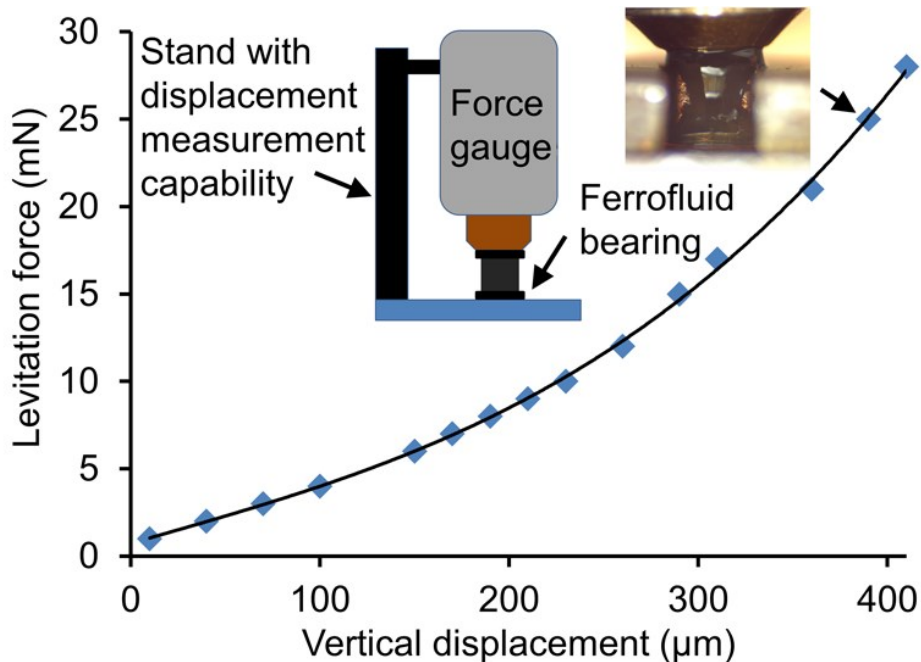


Figure 4.7: Levitation force generated with the ferrofluid bearing measured as a function of vertical displacement

using a digital force gauge (DS2-1, Imada Inc., IL, USA) by displacing the magnet using the probe of the gauge as shown in Figure 4.7 (the average of three separate measurements is plotted). As can be seen in the result also shown in Figure 4.7, the force increased with the magnet displacement, reaching, e.g., 28 mN when the levitated distance was decreased to $\sim 50 \mu\text{m}$. This suggests that the slider could support an additional load of 2.86 g on top of the magnet while maintaining a $50 \mu\text{m}$ bearing gap. The increase of the force could be related to the following condition: As the magnet is pushed against the substrate, the magnetic field lines near the pole (facing the substrate) are squeezed into a thinner layer of ferrofluid, effectively increasing the magnetic flux density and thus the internal pressure of the ferrofluid (as suggested in Eq. (4.1)). It should be noted that the amount of ferrofluid applied on the magnet determines the levitation height of the magnet that also affects the maximum allowable load that does not cause the slider to touch down the substrate.

4.4.2 Actuation Force

To quantify the actuation force that the fabricated device provides, tilting tests similar to the test

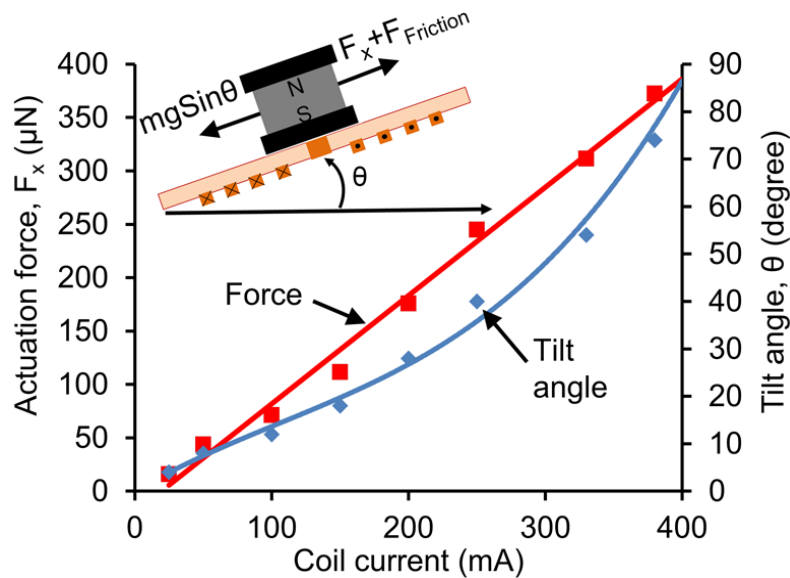


Figure 4.8: Actuation force vs. driving current with an inset showing the measurement method.

described in the previous subsection were performed, where the 1.6 mm magnet levitated on the coil was placed on a tilting stage, and the minimum angle that led to the magnet's motion was recorded at different driving currents. Figure 4.8 shows the average of two measurement results. At the boundary point, forces are balanced in the system so that $F_x + F_{friction} = mgsin\theta$, where m is the mass of the magnet, g is the gravitational acceleration, and θ is the tilting angle. The level of $F_{friction}$ is estimated to be $\sim 14 \mu\text{N}$ as described in the previous subsection. The values of θ measured with varying driving currents and F_x calculated from the measured θ and $F_{friction}$ (assuming that it is dominated by the substrate-ferrofluid interaction and nearly constant) are plotted in (Figure 4.8). As shown, the current of 380 mA led to θ of 74° or F_x of $370 \mu\text{N}$, and the relationship between the force and the current was approximately linear with a coefficient of $0.95 \mu\text{N}/\text{mA}$. When the current was raised to 400 mA, the magnet was stationary even when the stage was tilted to vertical ($\theta = 90^\circ$); this suggests that F_x is at least $386 \mu\text{N}$ at the current level.

4.4.3 Actuation on a Single Coil

The dynamic behaviors of levitated magnet sliders were characterized using the experimental set-up shown in Figure 4.9. As illustrated, a function generator was used to command a bipolar power supply, generating current signals that were fed to the coil to drive the slider. The motion of the slider was tracked using a laser displacement sensor (LK-G32, Keyence Co., ON, Canada) with 10nm resolution.

As the first step, the 3.0 mm magnet slider was driven with a square-shaped current signal generated so that the coil was turned on in the attraction mode for 3 seconds and then in the repelling mode for the next 3 seconds by switching the direction of the current. This cycle was repeated to actuate the magnet slider. The current level was kept constant at 200 mA for each

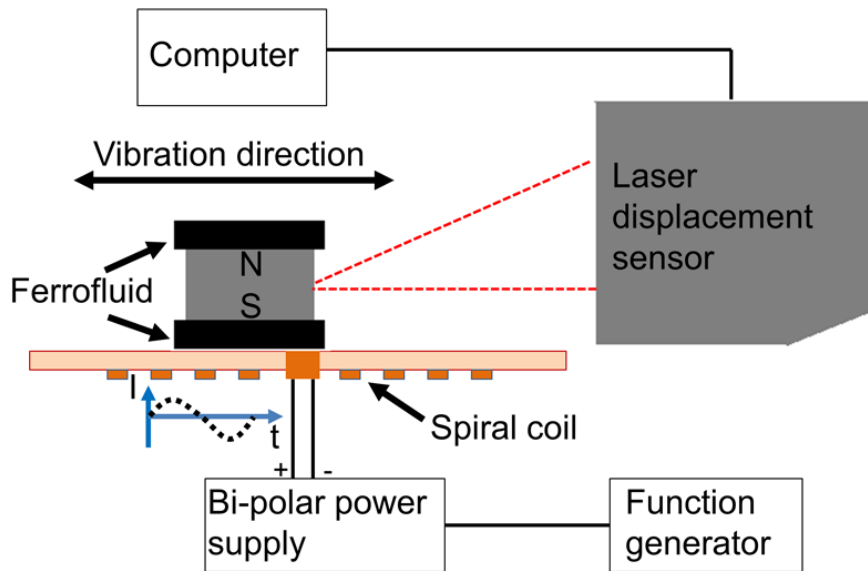


Figure 4.9: Experimental set-up used to characterize dynamic responses of the sliders.

direction. Figure 4.10(a) shows a typical response of the slider recorded. As can be seen, the slider was actuated corresponding to the square-wave input signal with rapid displacements between the center and periphery of the coil. The maximum acceleration of the actuation observed in this test was calculated to be $\sim 1 \text{ m/s}^2$. In the attraction mode, the slider moved to the coil center while showing an overshooting motion, and in the repelling mode, the magnet was moved to the coil periphery and trapped at that location, again with a similar overshooting motion as indicated in Figure 4.10(a). These bistable states at the coil center and periphery match well with the simulation results as discussed in Section II. Measurement results with sinusoidal input signals at frequencies of 1 Hz and 5 Hz are shown in Figure 4.10(b) and (c), respectively. In these signal patterns, the positive swing caused the attraction of the magnet whereas the negative swing led to the repulsion of it. The current amplitude was 100 mA for both frequencies. For 1 Hz (Figure 4.10(b)), the overshooting effect appeared as the slider reached the equilibrium positions at the coil center and periphery similar to the square-wave case discussed

above. In contrast, the result with 5 Hz (Figure 4.10(c)) did not exhibit this effect; this is because as the frequency increased, the magnet started to be pulled back before it reached the coil center or periphery, i.e., the actual travel distance became smaller (and reduced to ~ 0.85 mm in the particular case shown in Figure 4.10(c) than the distance between the two stable positions, resulting in a smooth actuation with no overshooting motion. Figure 4.10(d) displays a fast

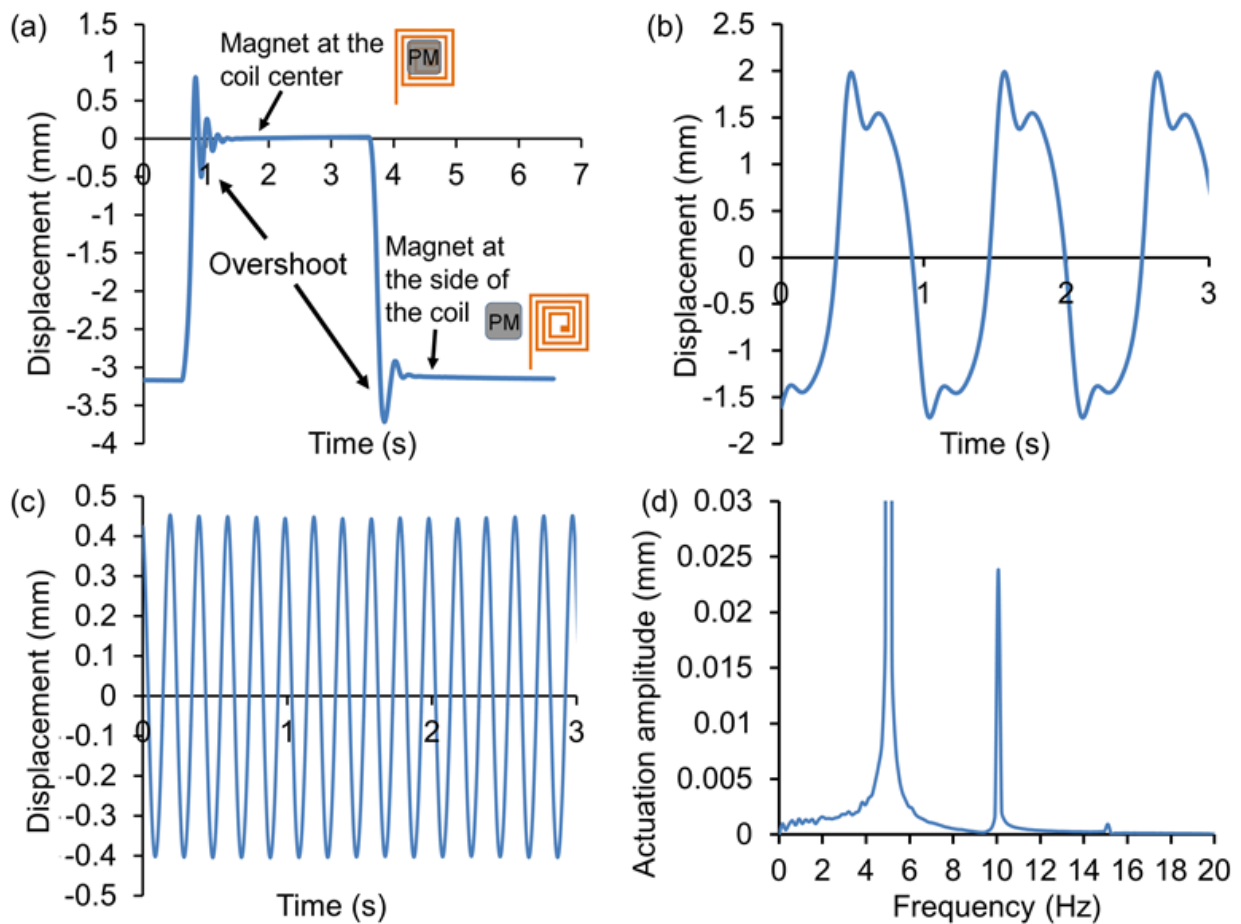


Figure 4.10: Temporal response of the levitated 3.0 mm magnet slider to (a) 200 mA square-wave current, (b) 100 mA sine-wave current at 1 Hz, and (c) 100 mA sine wave current at 5 Hz (the zero-displacement location in (b) and (c) corresponds to the halfway point between the coil center and periphery); (d) fast Fourier transformation of the slider response at the current frequency of 5 Hz.

Fourier transform of the slider response with the 5 Hz input frequency, indicating the main actuation frequency at the original 5 Hz along with super-harmonics (at 10 Hz and 15 Hz) in the response. The dependence of the displacement amplitude on the input frequency (up to 20 Hz) was further evaluated with two different current amplitudes, 100 mA and 200 mA. The results measured with the two sliders, the 1.6 mm and 3 mm magnets, are plotted in Figure 4.11(a) and (b), respectively. In these tests, the same coil was used to acquire two sets of data for each of the

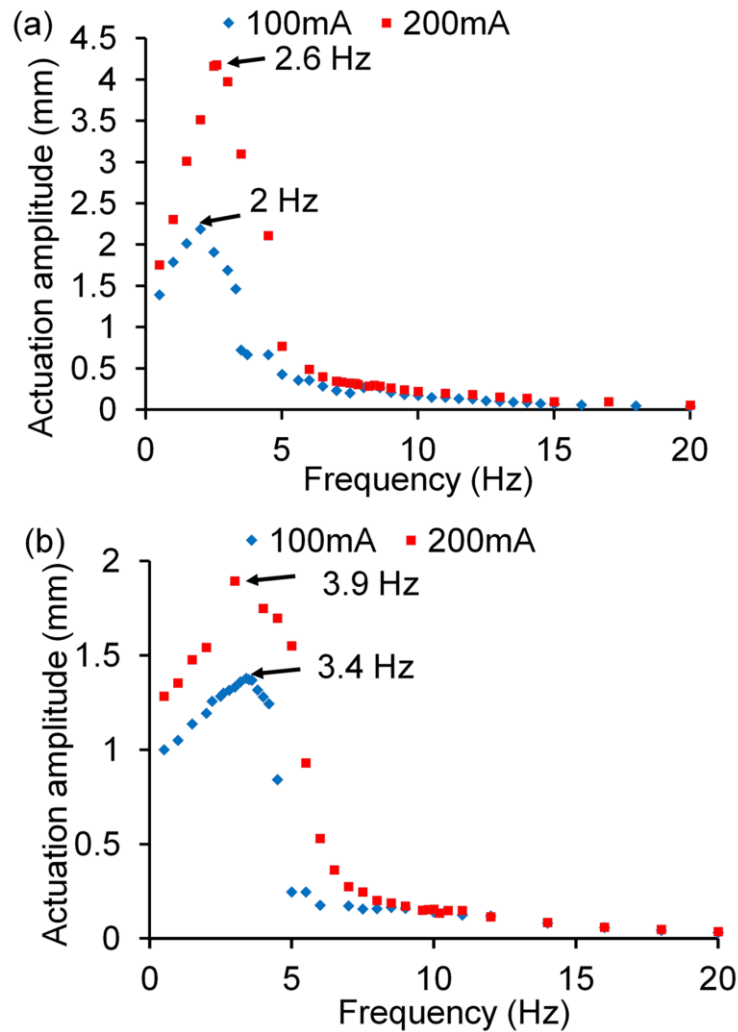


Figure 4.11: Frequency responses of oscillated actuations at different driving currents for (a) the 3 mm magnet and (b) the 1.6 mm magnet, showing corresponding resonant frequencies.

magnets. (Note that the variations in the data points were substantially smaller compared with the markers used in these plots; this is also the case for the results to be shown in Fig. 12). Both cases in Figure 4.11(a) and (b) indicate distinct resonances of the sliders at around 2-4 Hz for the tested current levels, with slightly higher frequencies for the smaller slider.

These resonant behaviors can be explained as follows: During the actuation, the magnet is attracted to either of the bistable locations (coil center and periphery) depending on the direction of the current. When the magnet reaches one of these locations, the magnet exhibits an overshooting motion (as seen in Figure 4.10(a) and (b)) while passing the location due to its inertia. For a given current amplitude, the overshoot distance is maximized under a certain rate of temporal change in the input signal (with a sinusoidal wave) that the decelerating magnetic force acting on the magnet moving away from the location becomes the lowest level, leading to the largest overshoot, at which the actuation enters the resonant condition. The results also show the response dependence on the current levels, in terms of both vibration amplitude and frequency. The vibration amplitudes were observed to increase with the current for frequencies up to ~8 Hz (where the amplitudes diminished to minimal levels for both currents); this outcome can be explained by the probable condition that a larger actuation force induced by the larger current pushed the slider to travel more within a given cycle time. The results in Figure 4.11 also indicate small shifts in the resonant frequencies to higher levels when a larger current (200 mA) was used. It is evident that as the current level rises, the magnet is displaced with a larger actuation force, i.e., a larger acceleration level. The observed shifts suggest that although the actuation amplitude at resonance increases with the current as described above, the magnet completes its travel cycle in a shorter time due to the effect of enhanced acceleration, which

appears to serve as the dominant factor in the cycle time in the particular set-up used, leading to the frequency shift observed.

The vibration amplitude was evaluated as a function of the driving current in detail using sinusoidal signals at a fixed frequency of 0.5 Hz (Figure 4.12). The results indicate that the current level that the travel distance reached the distance between the center and edge of the coil (1.2 mm) was ~80 mA for the 3 mm magnet and ~160 mA for the 1.6mm magnet. The currents larger than these levels were required for the repelling mode to push the magnet out of the coil across the periphery of the coil while overcoming a small attraction force exerted to the magnet at the periphery (as discussed with Figure 4.3 in Section 4.2). It is also worth noting that for the currents greater than 300 mA, the magnet could not be attracted back to the center of the coil once it escaped the coil area. This can be due to large repelling forces caused by the large driving currents which pushed the magnet too far from the coil so that it received an insufficient

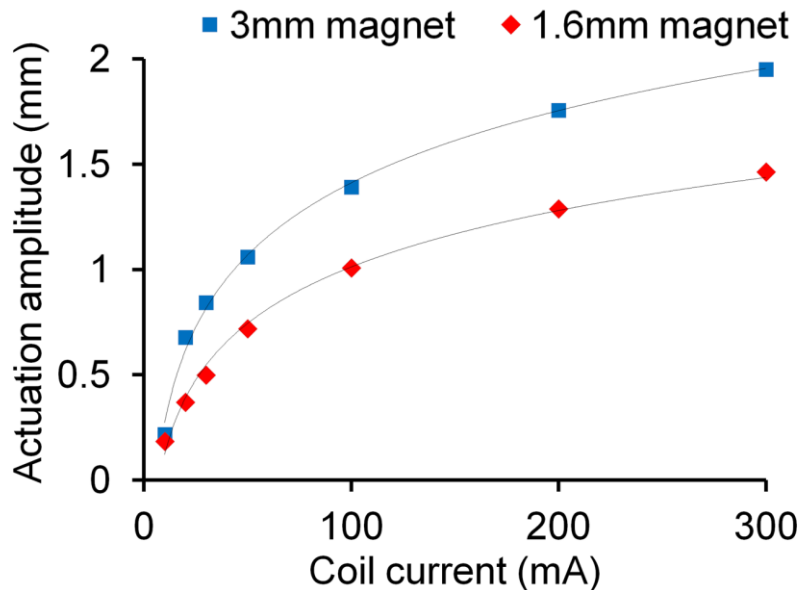


Figure 4.12: Oscillation amplitude vs. driving current at 0.5 Hz frequency for the 3 mm and 1.6 mm magnets.

attractive force from the coil when the current direction was reversed. The small repelling force exerted at the periphery of the coil in the attraction mode may have played an additional role to prevent the magnet from returning back to the coil area.

4.4.4 Continuous Actuation on the Coil Array

The linear actuation of the levitated slider along the coil array shown in Figure 4.6(a) was tested through sequential activations of the coils using the logic depicted in Figure 4.13(a). In each step, two coils were activated. The coil on which the slider was located was activated to repel the

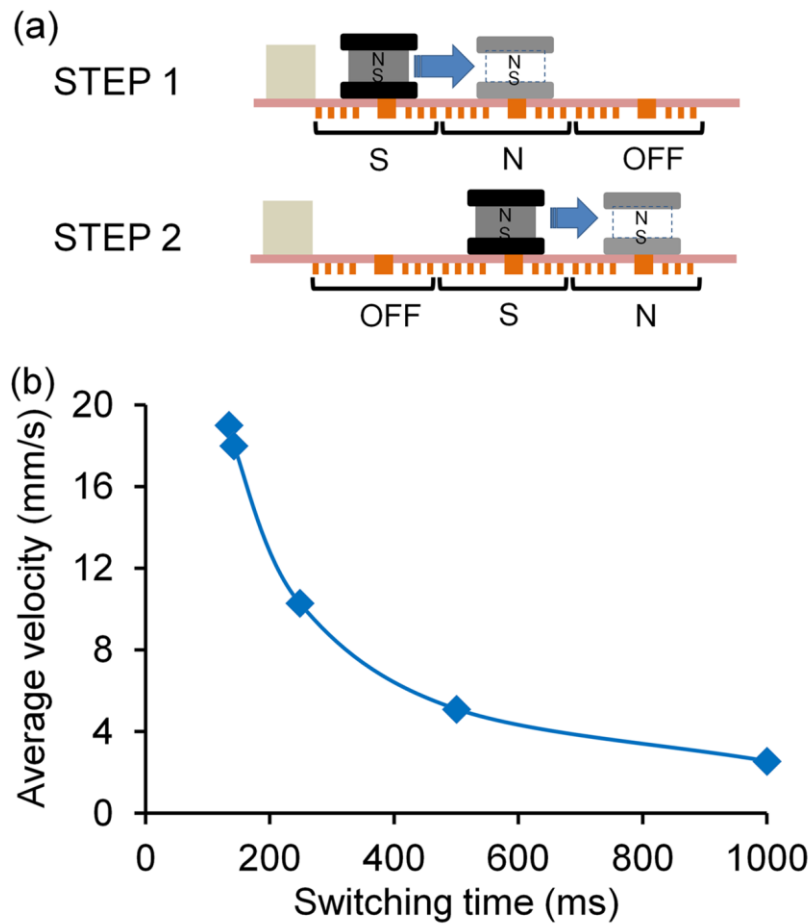


Figure 4.13: Continuous actuation of the slider on its rail track; (a) logic used for the actuation; (b) measured average velocities of the 1.6 mm magnet slider with varying switching times; variations in the velocity levels (observed through three sets of measurements) are smaller than the marker used.

slider while the adjacent coil was activated to attract it (Step 1 in Figure 4.13(a)), sending the slider from the former coil to the latter. Then the same activation pattern was applied to the next two coils to move the slider further (Step 2 in Figure 4.13(a)).

It was observed that there was an optimal range of the switching time between Step 1 and Step 2 to make smooth motions along the array. If the switching was too slow, the slider made stepwise motions with a low overall speed. In contrast, too fast switching attracted the slider back to the first coil before it reached the second coil, resulting in no continuous motion. The average velocity of the 1.6 mm slider was characterized with varying switching times (Figure 4.13(b)).

For this test, the driving current was fixed to be 300 mA, well larger than the level (160 mA) necessary to send the slider to the next coil as discussed in Subsection C. The stepwise motion became obvious when the switching time was set to be ~ 200 ms or more, limiting the overall speed as indicated in Figure 4.13(b). The slider exhibited smoother and faster motions as the switching time was shortened – the maximum velocity of 19 mm/s was obtained with a switching time of 134ms, which was the threshold for inducing continuous actuation of the above slider.

4.4.5 Position Control Between Two Coils

There is a possibility that the position of a magnet slider between two coils is precisely controlled by varying the power distribution to the two coils, enabling stepping motions of the slider. This feasibility was investigated through the following experiment. Initially, the slider, the 3mm magnet, was attracted to and located on one (first) coil by feeding a current of 300 mA to it while an adjacent (second) coil was deactivated. Part of the current to the first coil was then transferred to the second coil stepwise (with a 10% increment) to attract the magnet from the first coil. In this set-up, as the magnet was slightly larger than the coil (with the size of 2.4 mm), the

edge portion of the magnet overhung the periphery of the second coil when it was at the initial state on the first coil. The slider was displaced between the two coils for two consecutive cycles. Figure 4.14 shows the measured displacements and the standard deviation measured in the slider position for the entire travel distance (from the center of the first coil to that of the second coil). The result clearly displays that the stepping actuation can be implemented by controlling power distribution between two adjacent coils. This figure also indicates the region that exhibits large displacements with current transfer (at around 20-40%), beyond which the actuation shows a relatively low and constant displacement rate. (The average speeds of traveling observed in these two main regions were 4.3 mm/s and 1.4 mm/s, respectively.) The main cause of the rapid displacement is presumably due to the rise of the magnetic field on the second coil with

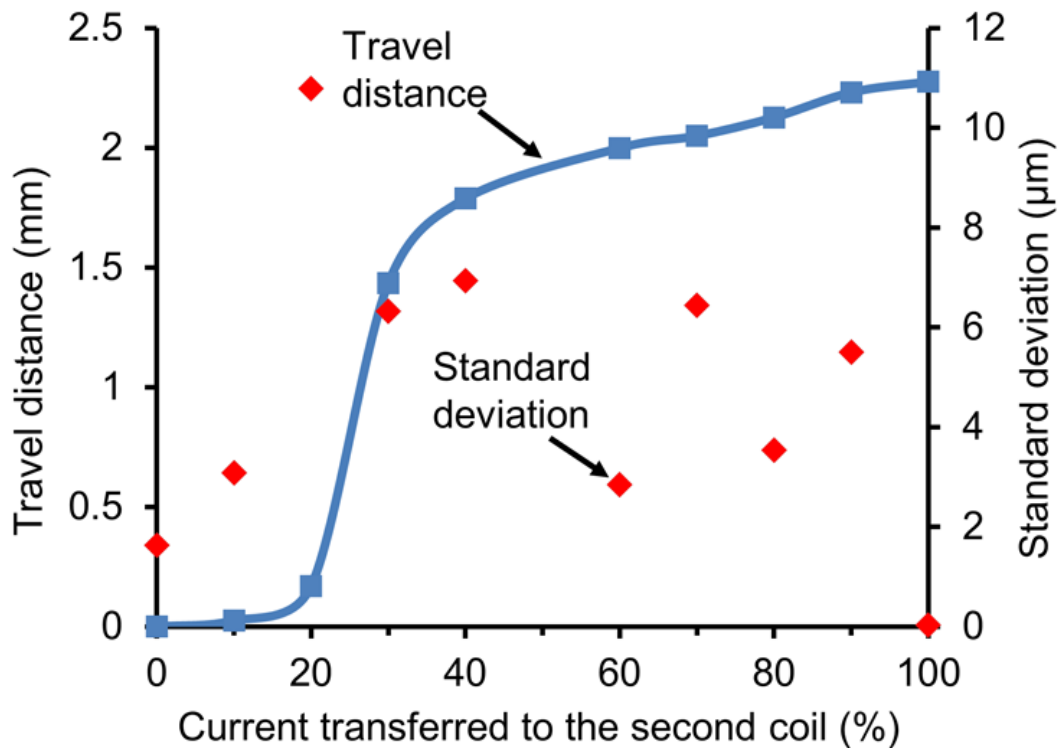


Figure 4.14: Measured step-mode displacements of the magnet slider actuated between two adjacent coils by varying current distribution to the coils.

increased current transfer to it, in combination with a large gradient of the field near the periphery of the coil (refer to Figure 4.3) that strongly pulled the magnet into the second coil (as suggested in Eq. (4.4)).

When the current transfer exceeded $\sim 40\%$, the magnet started entering the central area of the second coil where the field gradient was relatively small, lowering the displacement rate. This region, with a low and constant displacement rate, may be more suitable for implementing finer stepping motions for the particular set-up used. For example, Figure 4.14 suggests that, if the slider is operated in the current-transfer region between 40% and 100%, stepping of 7-8 μm may be achieved with a current-transfer increment of 1%. More uniform displacements over the entire travel distance could be approached by controlling the current transfer in a non-linear manner, possibly using a proper feedback scheme instead of the open loop method used in the current test, and/or using different coil arrangements (e.g., partly overlapping the coils by fabricating them in different layers) that lower the field gradients along the travel distance toward eliminating the rapid displacement region.

4.5 Conclusion

The ferrofluid-based levitation of permanent magnets and its microactuator application have been studied. A layer of ferrofluid served as the self-sustained bearing that lifted the magnet and physically followed the magnet as it moved, realizing low-friction motions of the magnet. The magnetic pressure generated within the ferrofluid layer established on a 1.6 mm cubic magnet was large enough to not only levitate the magnet itself but also support an additional load of up to 28 mN. The frictional force for the magnet was experimentally estimated to be $\sim 14 \mu\text{N}$. The linear actuation of the ferrofluid-levitated magnet slider was performed using an array of

microfabricated planar coils as the rail track that generated magnetic field gradients to displace the sliders. The force provided by the actuator was measured to be 386 μN or greater with 400 mA driving current. The bidirectional motions of the sliders over a planar coil were characterized under different driving conditions. Both continuous and stepping actuations were successfully demonstrated. The continuous linear actuation with the maximum velocity of 19 mm/s was achieved with optimized switching control of the coil array. This extremely simple, assembly-free ferrofluid micro bearing could be applied to a variety of micromotor applications to enable high-reliability devices with low costs. Future work will encompass further investigation and optimization of device design and ferrofluid bearing toward the improvement of actuation performance including the precision slider control for step-mode displacements.

Chapter 5: Ferrofluid-assisted Micro Rotary Motor for Minimally invasive endoscopy Applications⁴

5.1 Introduction

Micro-scale rotary motors have a vast range of potential applications in broad areas. One promising area is medical applications [69]–[71]. Microendoscopic catheters for minimally invasive medical imaging are an excellent application example. Advanced catheter devices that use rotary motors coupled with prism-shaped mirrors to perform full 360° circumferential scan for endoscopy have been widely investigated [72]–[75]. Piezoelectric rotary micromotors were developed for this type of application [76]. The use of magnetic actuation, however, has been a dominant approach in this area [72]–[74] for various reasons, including higher speeds, smaller sizes, and wider commercial availability compared with the piezoelectric type. One of the critical needs in the design of imaging endoscopes is the flexibility of the catheter. The magnetic micromotors used in these catheters, have large axial lengths (>1 cm [73]–[75]) in most cases, due to the need for a long cylindrical magnet, with a gear box to increase the output torque and compensate for large frictions between rotor and stator. The large axial size of the motors, rigid parts embedded in the catheters, significantly limit the flexibility and thus maneuverability of the catheters inside the body. Moreover, manufacturing of this type of micromotors requires high-precision assembly/packaging processes such as coil winding, which increase the overall production costs.

⁴ Part of this chapter appeared in the following publications:

1. B. Assadsangabi, M. H. Tee, S. Wu, and K. Takahata, “Ferrofluid-assisted micro rotary motor for minimally invasive endoscopy applications”, 27th IEEE Int'l Conf. Micro Electro Mechanical Systems (MEMS 2014), San Francisco, Jan. 26-30, 2014, pp. 200-203.

One fundamental challenge in the realization of practical micromotors is the development of a reliable rotor bearing. At present, most of commercially available miniaturized motors utilize microballs (e.g., Maxon Motor, Switzerland) or sintered metals (e.g., Faulhaber, Germany) as the bearing components. The fabrication and packaging necessary to integrate microball bearings with the other motor components including guiding structures further raises the complexity and cost of motor manufacturing. Moreover, the size of microballs (the smallest being a few hundreds of microns reported in, e.g., [77]) limits the miniaturization of the bearing and motors. Sintered-metal bearings are structurally simple and lower cost; however, this type of bearings is not well suited for low-speed actuations (e.g., 240 rpm [73]) used for endoscopy imaging as the friction force increases at lower speeds. The wear of the bearing materials is another critical concern in these types of bearings. Hydrodynamic lubrication is also not practical for low speeds that make it difficult to maintain thin lubrication film [36].

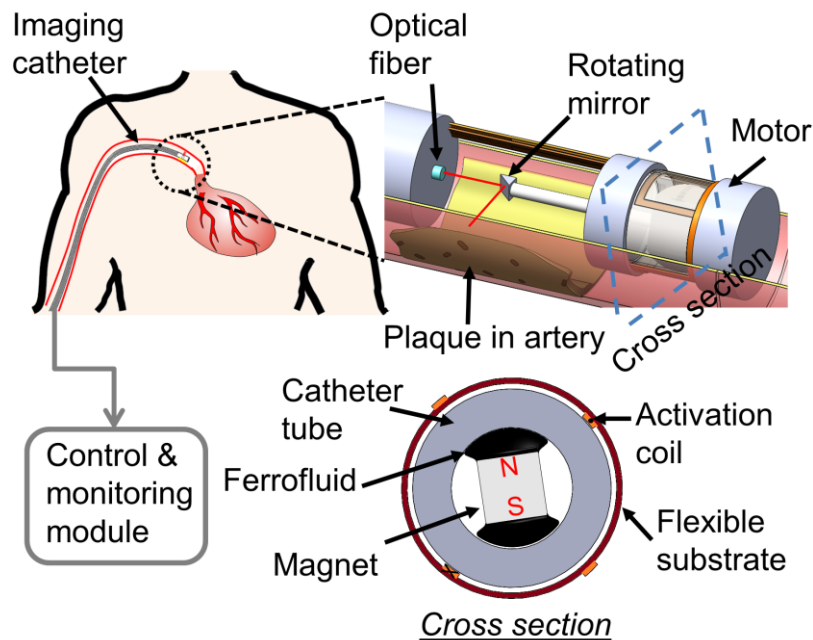


Figure 5.1: Conceptual diagram of the developed micro rotary motor and its application to microendoscopic catheters.

As shown in previous chapter, the levitation of permanent magnets can be achieved by the combinational use of ferrofluid that provides a reliable, low-friction bearing function highly suitable for micromotor applications. In this chapter, a rotary micromotor enabled with ferrofluid bearing is designed and fabricated.

Due to the extremely simple and self-sustained bearing mechanism as will be described, drastically shorter axial length of micromotors, suitable for medical catheter applications, can be realized. In order to demonstrate the feasibility of the ferrofluid-enabled rotary micromotor for endoscopic imaging applications (Figure 5.1), a proof-of-concept device has been developed and characterized. In the sequel, first the design and operation of the micromotor are discussed followed by a brief description of the motor fabrication process and subsequently the characterization results of the fabricated device is presented together with a preliminary test of endoscopic optical imaging application through rotating mirror performed in a test tube.

5.2 Micromotor Design and Operation

The developed micro rotary motor electromagnetically drives a permanent magnet as its rotor that is levitated by a ferrofluid layer inside a cylindrical hollow tube, or a catheter for the target application. When ferrofluid is applied onto the magnet, the fluid accumulates on the poles of the magnet due to the highest magnetic field gradient provided at those locations. As the ferrofluid layer is established on the magnet surfaces, the magnet is lifted up above the substrate surface due a magnetic pressure generated in the fluid. Therefore, the ferrofluid layer not only acts as a lubricant for the rotor to reduce the friction when rotated but also physically supports the rotor to be levitated from surrounding inner surfaces of the tube without external pressurizing means. Moreover, the ferrofluid layer is attracted to and self-sustained on the magnet and follows the

magnet as it rotates, eliminating the need for any precision alignment or special assembly to maintain the bearing layer in the motor construction.

The stator of the developed motor is composed of two meander-type coils, each of which is printed on a different side of the flexible polymer substrate, which is wrapped and bonded around the catheter tube to establish the stator circuit on its outer surfaces (as presented in Figure 5.1). Although, in this particular design, meander-type coils are chosen for the actuating circuit due to its simplicity, other geometries such as spirally shaped coils can also be utilized for the actuating circuit which can enhance the output torque of the motor. Figure 5.2 illustrates the design of the stator circuitry and its connection with the controller. The coils' patterns are designed to create four magnetic poles with 90°-phase difference around the tube.

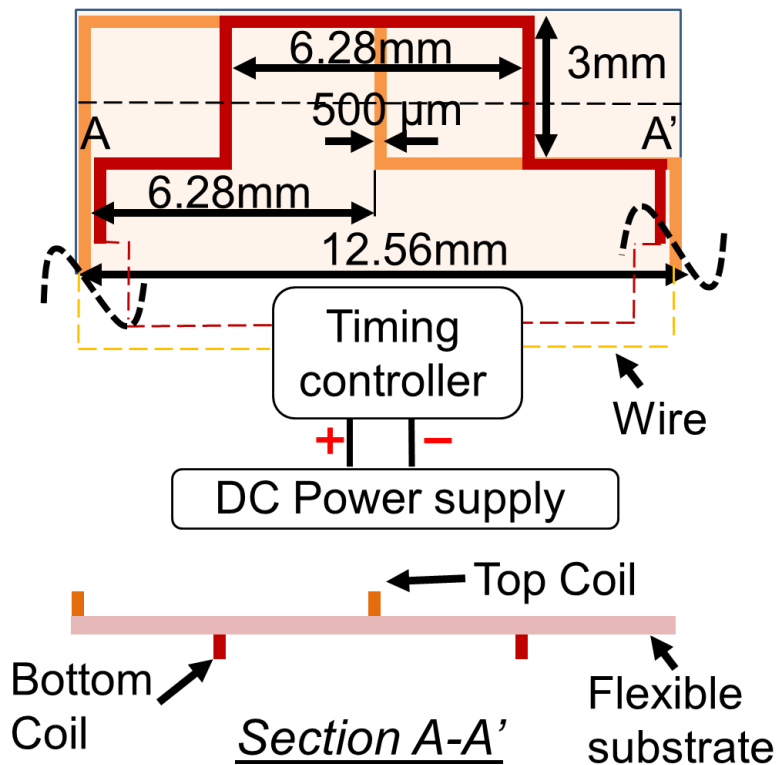


Figure 5.2: Design of the planar stator component, showing two driving coils patterned on opposing sides of the flexible substrate, and their connections with the current controller

For continuous rotation of the magnet, the coils are activated sequentially so that the magnet rotates 90° at each step. In each step, only one of the coils is activated and as the magnet rotates to a new position, the coil on the other side of the substrate is activated with a proper current direction so that the magnet rotates another 90° in the same direction. Figure 5.3 schematically demonstrates the rotation of the levitated magnet and the corresponding actuating current direction for each coil for a counter clockwise revolution. As suggested in Eq. (5.1) shown below the magnetic torque direction can be controlled by changing the B direction which can be easily done by changing the current direction at each step.

Although the proposed rotary motor may not need to provide high levels of torque for the targeted application due to low friction provided by ferrofluid bearing, in general, it is a major interest for a variety of applications. A simplified expression on the magnetic torque (T_m) acting on the magnet is given:

$$T_m = M \times B \quad (5.1)$$

where M is the magnet remnant magnetization and B is the external magnetic flux density generated by the stator coils. Eq. (5.1) assumes that the magnet is a thin a bar and the magnetic field is uniform across the magnet, therefore the expression does not take into account the distribution and variation effects in the field as well as the magnet size. Eq. (5.1) signifies that the magnet is rotated in direction so that its magnetization is aligned with the external magnetic field.

Also, Eq. (5.1) shows that magnetic torque can be increased by increasing either M or B . To increase M , a permanent magnet material with higher remnant magnetization should be selected; however, to increase B in a motor with fixed stator design, driving current should be increased which is constrained by the allowable operation temperature of the motor.

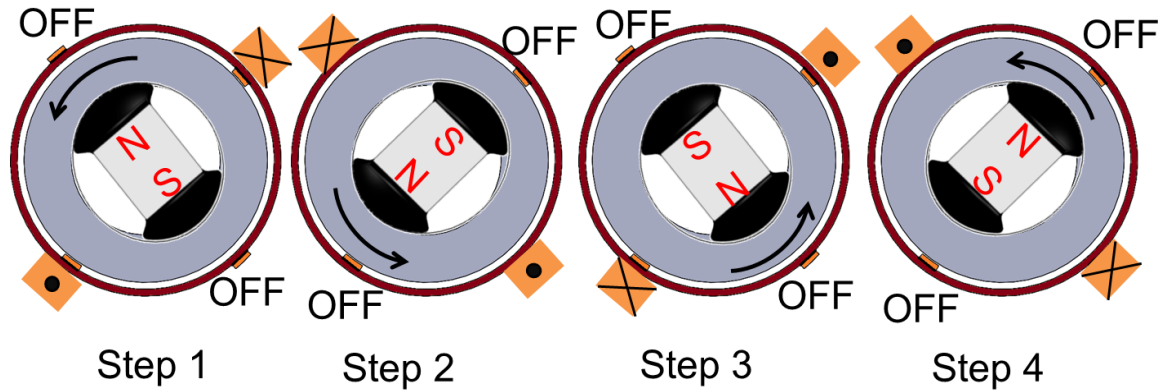


Figure 5.3: Activation logic used to produce a 360° rotation.

5.3 Fabrication Process

The activation coils of the micromotor were fabricated using double-sided Cu-clad polyimide (PI) film (Pyrlux AP8525R, DuPont NC, USA) as the substrate. The Cu-clad layers and PI film are 18 μm and 50 μm thick, respectively. The meander shaped coils were fabricated by photopatterning of dry-film photoresist (PM240, DuPont, NC, USA) laminated on the both sides of PI film. The activation coils are then bonded using epoxy around the tube made of glass with 2 mm or 0.7 mm inner diameters and 1 mm or 0.65 mm wall thicknesses selected for this proof-of-concept effort. For the rotor part, 1.6 mm and 500 μm magnet sizes were chosen. The 1.6 mm NdFeB permanent magnet (K&J Magnetics Inc., PA, USA) is coupled with a 0.8-mm-diameter steel shaft, and a 1-mm prism mirror is bonded at the free end of the shaft. The 500 μm magnet on the other hand, is micromachined from a bulk 500 μm NdFeB permanent magnet plate using Micro-Electro-Discharge Machining (μEDM) [78]. In order to attach a 300 μm nickel shaft to the magnet, first a 90 μm through-hole is μEDM ed in the magnet and was oriented perpendicular to the magnetization axis of the magnet and then the diameter of the shaft end was reduced to about 90 μm so that the shaft could be inserted into the through hole. Finally, a 500- μm prism

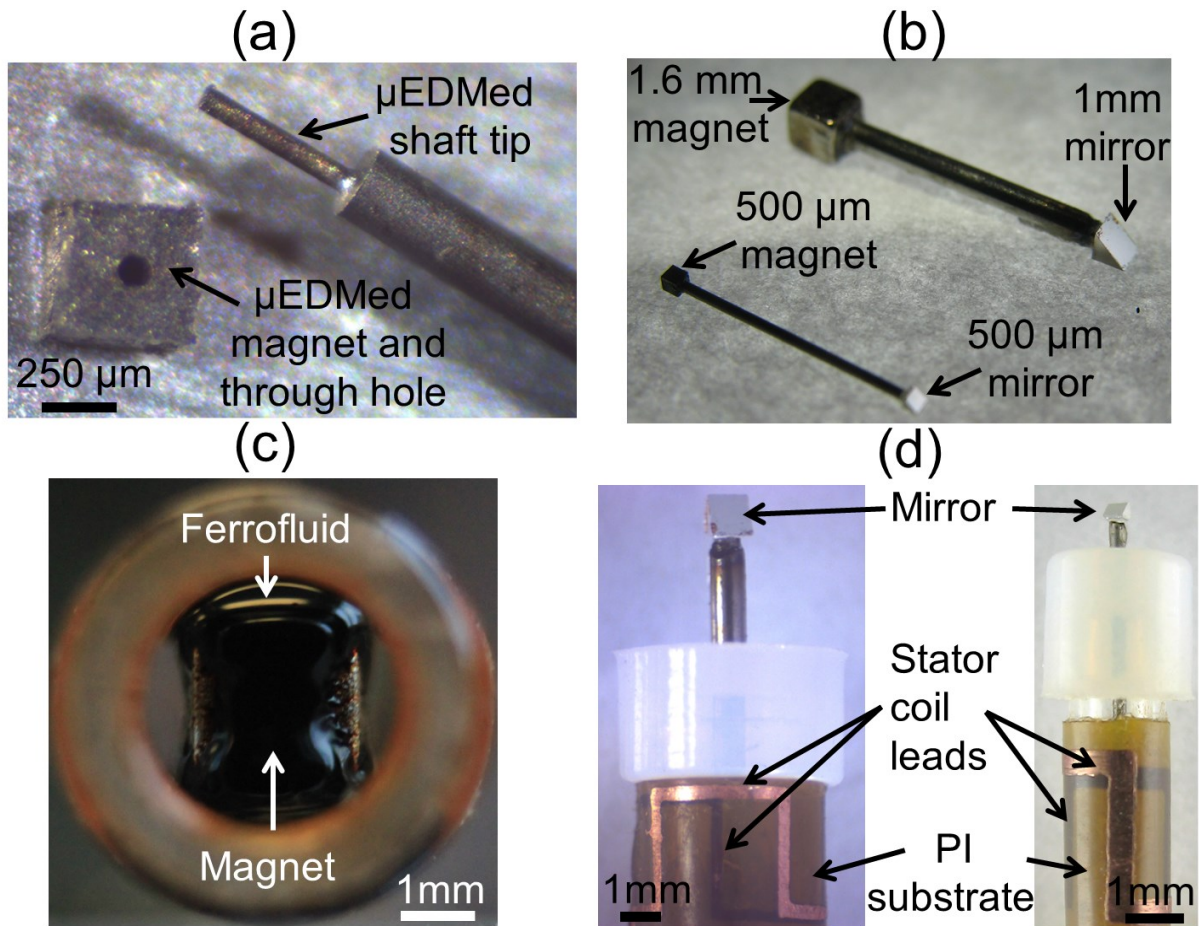


Figure 5.4: Optical images of (a) μ EDMed magnet and nickel shaft tip, (b) the rotor assemblies with the magnet, prism mirror, and coupling shaft, (c) the ferrofluid-levitated magnet rotor in the stator tube and (d) side view of the completed proof-of-concept devices.

mirror is glued to the free end of the shaft (Figure 5.4(a)). Figure 5.4(b) shows rotor assemblies for both motor sizes.

A commercially available oil-based ferrofluid (EFH1, Ferrotec Co., NH, USA) is applied onto the magnet to form a layer of the fluid between the magnet and the inner wall of the tube (Figure 5.4(c)). The tube is then capped by a 3D-printed plastic component with a hole that the rotor shaft passes through. Figure 5.4(d) shows the optical image of the fabricated samples for both abovementioned sizes.

5.4 Experimental Results and Discussion

5.4.1 Rotational Speed Characterization

The operation of the fabricated device was verified and characterized in air as well as under water using the set-up shown in Figure 5.5. In order to demonstrate the rotation of the mirror-assembled motor and quantify its revolution speeds, a laser beam was directed to the rotating mirror from the axial direction, and the motion of the reflected beam was video recorded as well as captured by a photodiode connected to an oscilloscope that displayed photo-induced voltages

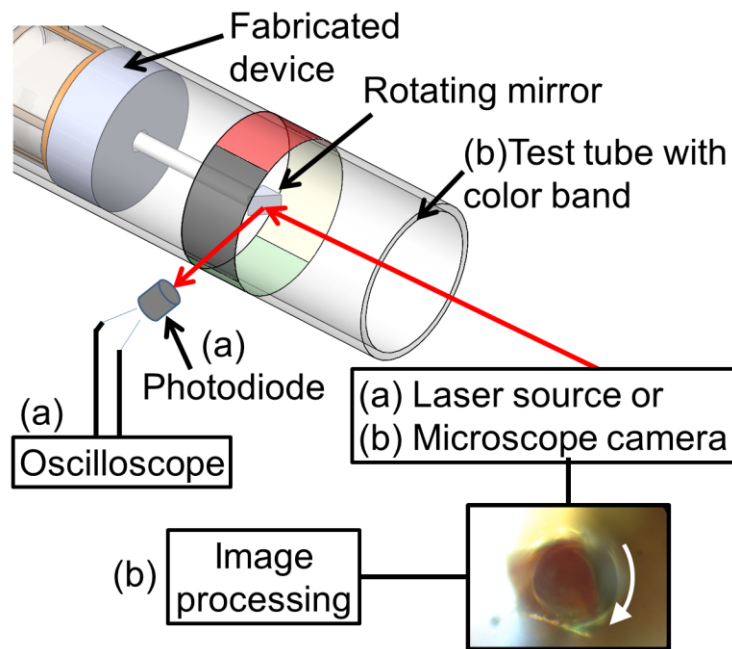


Figure 5.5: Experimental set-up used for (a) characterization of the fabricated rotary motor device and (b) preliminary test of endoscopic optical imaging through rotating mirror performed in a test tube with a color band. The image shown after the camera is an optical image of the actual mirror under rotation.

due to the incident beam (Figure 5.5(a)). The illustration in Figure 5 also includes the set-up used for optical imaging of the inner wall of a test tube (Figure 5.5(b)), which will be discussed later. The fabricated device was observed to provide stable rotation at different speeds using the control logic (Figure 5.3) by varying the switching time of the driving currents. This operation

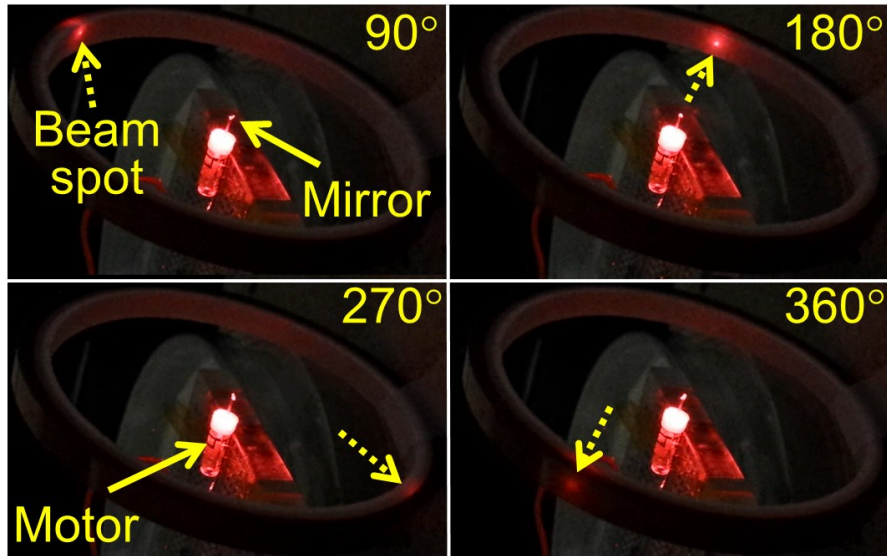


Figure 5.6: Angular scanning of laser beam (directed onto the inner wall of a plastic ring) by the rotating mirror showing the beam spot captured at each 90° step of one full rotation.

led to circumferential scanning of the reflected laser beam. Figure 5.6 shows the images of the reflected beam extracted from a video that recorded the rotation of the beam by 90° at each actuation step.

The rotation speed was characterized while shortening the switching time from the initial value of 500 ms. Also, it was observed that as the rotational speed increased, higher driving current was required to maintain stable rotation. The probable reason of the need for raising the current is that the torque, which is raised with the current, must be increased in order for the rotating rotor to catch up the speed of current switching. Therefore, minimum current that could maintain the stable rotation of the shaft was recorded as the speed was increased. Figure 5.7 shows the results of the speed characterization as the function of driving current for both rotor sizes (i.e. 1.6 mm and 500 μm). The test was repeated three times and the average current value with its standard deviation at each data point is plotted in Figure 5.7. It can be seen in Figure 5.7 that

maximum recorded speed for the smaller rotor is lower (i.e. 1500 rpm) than the device with larger rotor magnet (i.e. 1875 rpm) at the same driving current level. The reason for reduction in the maximum achievable speed for the miniaturized device could be due to the reduced magnetic torque on the smaller rotor magnet which is dependent on the magnet volume and although frictional force has also been reduced in the smaller motor, frictional effects depend on contact area and therefore have smaller impact while downsizing compared to magnetic forces.

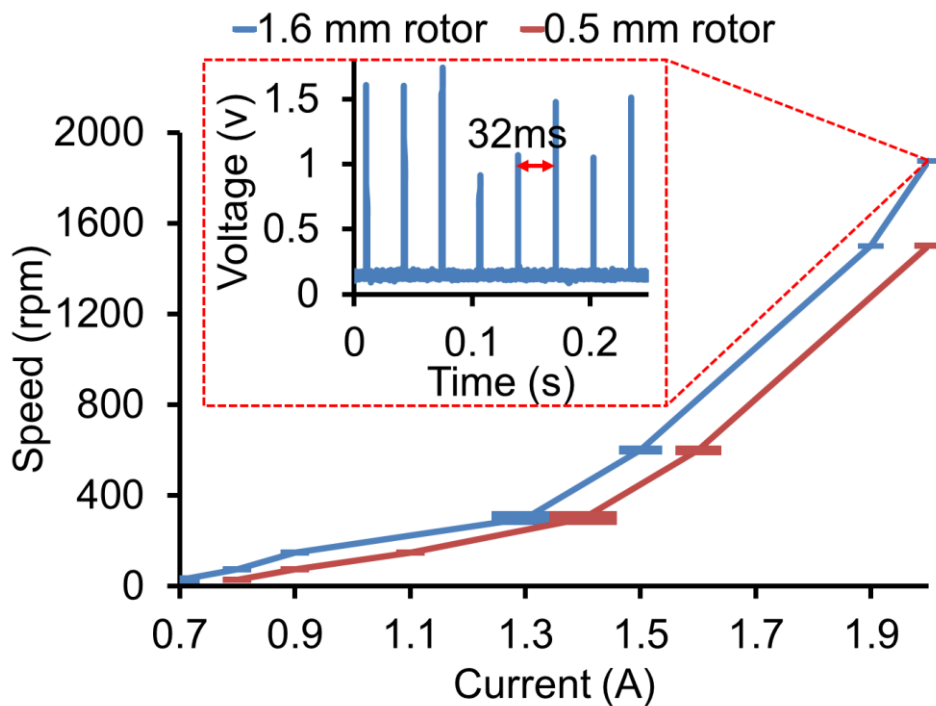


Figure 5.7: Rotation speed vs. driving current. Inset graph shows photodiode readings for the case of 8-ms switching time corresponding to the max speed recorded for the 1.6 mm rotor.

The maximum level of revolution speed obtained for both devices is well enough for endoscopic imaging applications (e.g., 240 rpm [73]) and in the case of the device with 1.6 mm rotor, there is the potential capability for real-time imaging (e.g., 30 revolutions per second [79]).

The operation of the device with 1.6 mm rotor was also verified by submerging it under water. The reason for this test is that for endoscopic applications based on ultrasound imaging the catheter is filled with water to create a matching medium to decrease wave propagation losses. In this test, it was made sure that water infiltrated into the glass tube containing the rotating magnet and is in contact with the magnet. Figure 5.8 illustrates the photodiode readings for the maximum recorded speed of the device in this test showing 2500 rpm at 2 A of actuating current. It can be seen that the maximum speed (at 2 A) in this configuration is higher than the case of operation in air. Although, the exact reason behind this increase is not clear, one possible explanation might be that the device is operating in a lower temperature compared to operation

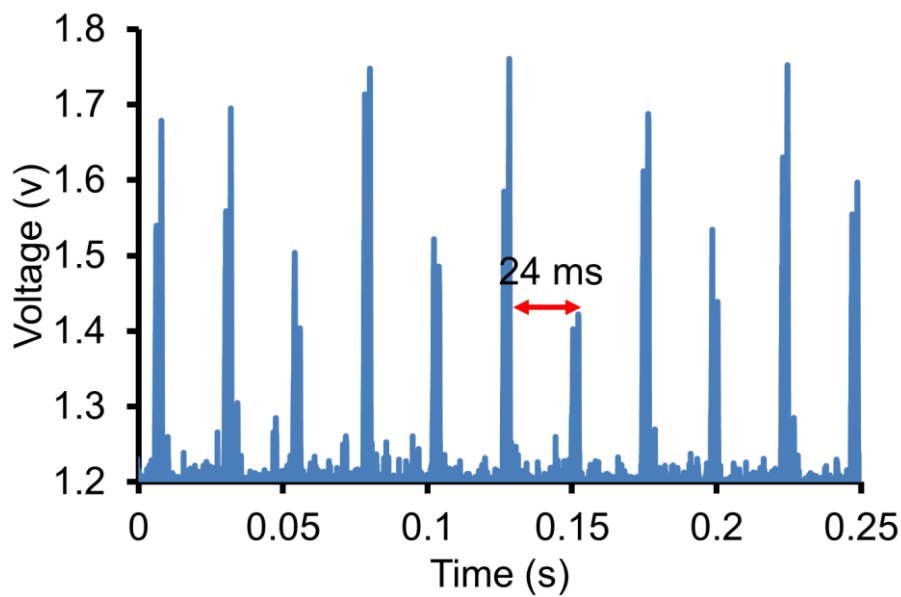


Figure 5.8: Photodiode readings for 6 ms switching time corresponding to the maximum recorded speed in water for the device with 1.6 mm rotor magnet

in air due to cooling effect in water. Lower device temperature means that the reduction in remnant magnetization of the rotor magnet due to temperature rise is smaller in this configuration which would result in a higher driving torque at the given applied current (e.g. 2 A for maximum speed). In order to validate this hypothesis further reinvestigation is required.

Another preliminary test was performed using an experimental model of body conduit/vessel to emulate the conditions involved in the endoscopic application. In this test, as illustrated in Figure 5.5(b), the device was placed inside the sample tube whose inner surface was circumferentially sectioned with four different colors (black, red, yellow, and green). The mirror was rotated with 1-s switching time while recording the optical image seen on the rotating mirror from the axial direction of the device/tube through a microscope. As shown in Figure 5.9(a), optical images of all the color sections were successfully acquired via the rotating mirror, which were then

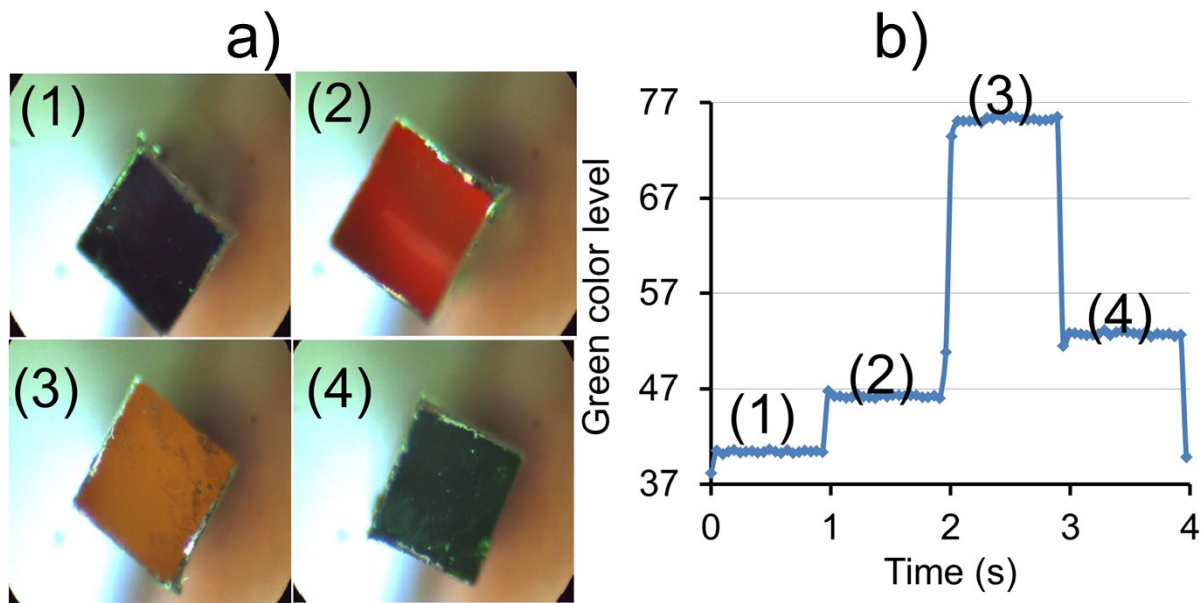


Figure 5.9: Endoscopic imaging test: (a) Rotating mirror at each 90° step detecting four different colors defined on the inner wall of the test tube; (b) detection of the green color component from the optical signals collected through the rotating mirror.

analyzed using the MATLAB® image processing toolbox to quantify a selected color component (in 8 bits) of the acquired optical signals as a function of time (Figure 5.9(b)). This demonstration verifies the feasibility of circumferential imaging through the fabricated micromotor device, an essential ability required for the targeted endoscopic application.

5.4.2 Stator Thermal Characterization

The temperature rise in the stator coils due to Joule heating is an important effect that should be characterized. This characterization becomes even more important in the target application of the proposed micromotor for endoscopic imaging since it determines necessary packaging of the device to prevent any thermal damage to tissue if device operation produces considerable heat.

Two sets of tests were performed for each rotor sizes operating in air and results are demonstrated in Figure 5.10 and Figure 5.11. In each test, the device was activated using the same logic and driving current as used in speed characterization test shown in Figure 5.7 and the test was done with and without the rotor in the glass tube. The reason for the test with and without the rotor was to investigate the effect of ferrofluid bearing frictional losses on the temperature rise of the devices. An infrared (IR) camera (VarioCam HiRes 1.2M, Jenoptik AG) was used to measure the stator surface temperature. Temperature measurements were taken every five minutes to ensure that the temperature has become steady.

This process was then repeated for another level of current after letting the coil to cool down to room temperature (i.e. 27.2°C). The temperature measurement point was chosen as close as possible to the copper wire (shown in the inset of Figure 5.11) where the temperature was maximum compared to other locations on the stator. It should be clarified that due to emissivity difference between copper and polyimide substrate, copper wire temperature looks cooler than polyimide in the infrared picture, which is not the actual case. In these tests, polyimide emissivity was assumed to be one. As seen in both Figure 5.10 and 11, both cases show similar levels of heating. It also shows that the temperature is slightly lower in the case where the rotor is present in the device compared with the configuration without the rotor. This could be due to the presence of rotor, shaft and the mirror, into which some of the heat is transferred results

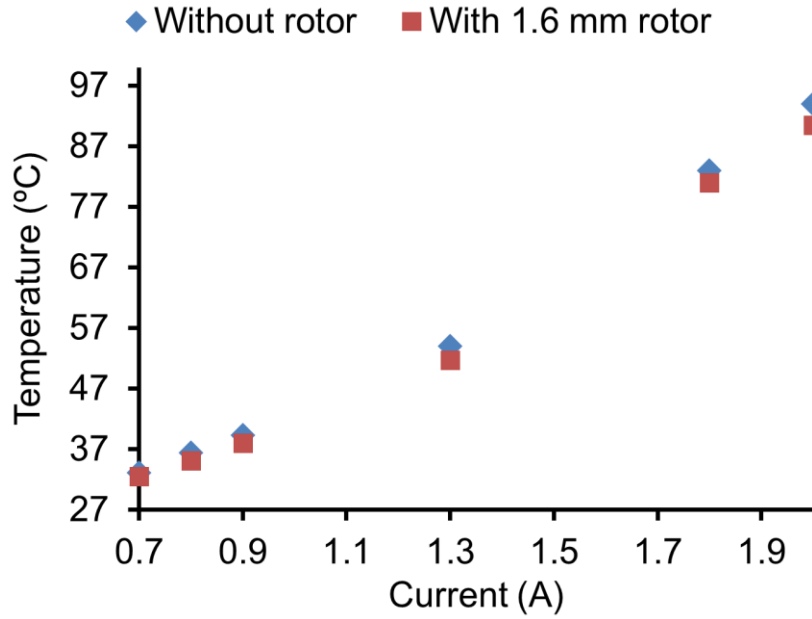


Figure 5.10: Stator temperature at different driving current for the device with 1.6 mm rotor. At each driving current, stator temperature is given for two cases (i.e. with and without rotor present in the device)

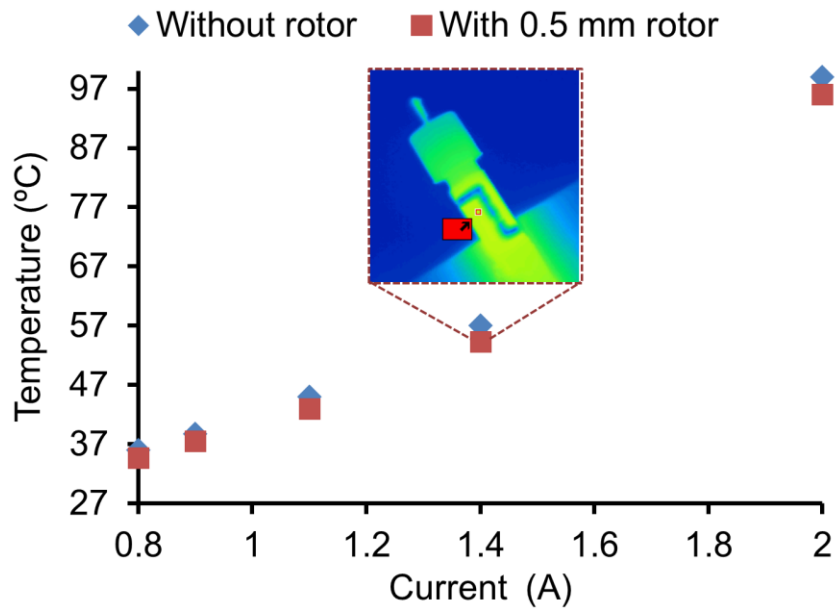


Figure 5.11: Stator temperature at different driving current for the device with 500 μm rotor. At each driving current, stator temperature is given for two cases (i.e. with and without rotor present in the device). Inset image shows the temperature distribution over the stator surface and measurement point taken by the infrared camera.

in lower overall temperature of the stator. Also, it can be confirmed that the frictional losses contribution from the ferrofluid bearing is small and can be ignored in these tests.

5.4.3 Discussion

As the result of the thermal characterization, it can be seen that the maximum stator temperature is quite high and therefore in order to use the motor in the endoscopic applications the current has to be limited to about 1 A which in turn limit the maximum rotational speed. However, according to Figure 5.7, the motor still can be used for endoscopic application with lower speed requirements. Moreover, further design optimizations could be considered to lower the stator temperature. One such design improvement would be to use copper clad substrates with thicker copper layers (e.g. Pyrlux AP 9222R, DuPont NC, USA, 70 μm thick copper) which would reduce the stator resistance greatly and also, a heat insulating packaging for the motor can also improve the amount of thermal impact of the device on the tissue.

Reducing the thickness of the stator glass tube will increase the effective magnetic flux density (B) acting on the magnet, an effective path to lowering the driving current or increasing magnetic torque (based on Eq. (5.1)); achieving both may also be approached by the use of a magnet with higher remnant magnetization (M) as the rotor material.

5.5 Conclusion

A novel micro rotary motor enabled with ferrofluid was designed, fabricated and characterized. Ferrofluid was used as a low-friction, self-sustained liquid bearing that levitated a permanent magnet that served as the rotor driven in the stator tubing. The magnet was electromagnetically actuated with microfabricated coils established around the stator tube. Two micromotors with 1.6 mm and 500 μm rotor sizes were fabricated and tested. The fabricated prototypes of the motor

were successfully operated to rotate the prism mirrors connected to the motors with revolution rates as high as 31.3 Hz and 25 Hz for the 1.6 mm and 500 μm rotor sizes, respectively. The endoscopic imaging function was demonstrated with the device coupled with the test tube used as a vessel model by collecting optical images of the inner walls of the model through the rotating mirror. Thermal responses of the devices were also characterized showing comparable responses for both fabricated prototypes. The ferrofluid-based bearing and levitation mechanism, with its simplicity and efficiency, offers potential advantages in the miniaturization with remarkably shortened axial sizes as well as in the production cost, enabling robust and low-cost rotary micromotors suitable for not only endoscopic imaging but also other applications in the medical area and beyond.

Chapter 6: Conclusion

This dissertation have reported experimental investigation and development of ferrofluid enabled MEMS. A complete form of the research which included modeling, simulation, fabrication and experimental verification of the ferrofluid-based micro devices was reported. A summary of the contributions from the research conducted and the future direction of this research is presented in this chapter.

6.1 Contributions

The main contribution of the present research was to propose and demonstrate new and novel approaches that ferrofluids could be used to enable various microactuators as well as other microdevices and hence broaden ferrofluids applications in MEMS research community.

More specifically, the contributions could be considered into two main categories. In the first category, a new actuation scheme was proposed for the operation of fully integrated ferrofluid-enabled microactuators using microfabricated coils and then two proof-of-concept devices were developed based on the proposed actuation scheme. In the second category, ferrofluid levitation of permanent magnets was studied. The efficacy of this levitation mechanism for bearing action was demonstrated through the development of a linear as well as a rotary micromotor. The acquired promising results suggest that the structurally simple and assembly-free ferrofluid micro bearing could be applied to a variety of micromotor applications to enable high-reliability devices with low costs.

In the sequel, research contributions in each chapter are presented in more detail:

I. Chapter 2

In this chapter, a new integrated method that utilized planar spiral coils with bias fields from permanent magnets for the ferrofluid actuation was presented. Combinational use of a controlled

magnetic field provided by planar coils and a bias field was shown to enable bidirectional actuation of ferrofluid to/from the coil depending on the direction of the current passed through the coil. The actuation principle was discussed in detail using finite element analysis (FEA) and experimentally demonstrated

In order to demonstrate the application of the proposed method, mirror cells with variable reflectivity were developed toward the application to imaging devices and optical switches. The planar coils were lithographically fabricated and were used for activation/deactivation of individual cells enabled by the bidirectional radial motion of the ferrofluid layer. As ferrofluid was manipulated over the mirror surface the reflectivity of mirror cells were modulated. The static and dynamic behaviors of the ferrofluid in the devices were characterized through an image processing approach. Multiple mirror cells were selectively and simultaneously operated to show enhanced ferrofluid control uniquely available with the two modes of the actuation as well as to demonstrate pattern generation with the arrays.

II. Chapter 3

As another application of the developed actuation method in Chapter 2, a micropatterned planar variable inductor was developed in this chapter. Ferrofluid was used as a moving magnetic core to modulate the inductance in the device. The ferrofluid actuation was enabled by the magnetic field provided by another planar coil in combination with a bias field, which allowed repelling motions of the fluid from the inductor in the reverse-mode operation. The device was characterized for both actuation modes (i.e. reverse and forward) and it was concluded that reverse mode of operation offered substantially larger inductance variations compared with the forward-mode case, though having slower response time. Frequency tuning was also demonstrated using an L-C resonant tank constructed using the developed variable inductor. In

addition to potential applications in electrical/electronic circuits, the simple and integrated operation concept of the device may provide a path to improve various ferrofluid-based sensors in their performance and sizes.

III. Chapter 4

In this chapter, a bearing mechanism based on ferrofluid levitation of permanent magnets and its microactuator application was presented. A layer of ferrofluid served as the self-sustained bearing that lifted the magnet and physically followed the magnet as it moved, realizing low-friction motions of the magnet. The magnetic pressure generated within the ferrofluid layer was large enough to not only levitate the magnet itself but also support an additional load. The frictional force for the magnet was experimentally measured confirming low frictional force in the bearing. The linear actuation of the ferrofluid-levitated magnet slider was performed using an array of microfabricated planar coils as the rail track that generated magnetic field gradients to displace the sliders. The bidirectional motions of the sliders over a planar coil were characterized under different driving conditions. Both continuous and stepping actuations were successfully demonstrated.

IV. Chapter 5

Using the ferrofluid as a microbearing, a novel micro rotary motor was designed, fabricated and characterized. The rotor magnet was electromagnetically actuated with microfabricated coils established around the stator tube. The fabricated prototypes of the motor was successfully operated to rotate the prism mirror connected to the motor. The endoscopic imaging function as a target application was demonstrated with the device coupled with the test tube used as a vessel model by collecting optical images of the inner walls of the model through the rotating mirror. Thermal responses of the devices were also characterized.

6.2 Future Works

Future works as the continuation of the present thesis can be group into three categories:

I. Investigations on further characterization of the ferrofluid actuation methods using planar coils biased by permanent magnet field

Further characterization of the developed actuation method in this thesis should be done in order to improve the performance of the microactuators based on this method. Detailed investigation and mathematical modeling on the effect of various design parameters such as substrate surface properties (e. g. hydrophobicity, roughness, surface tension, etc.), ferrofluid viscosity and saturation magnetization should be performed to study their impact on various performance measures of the devices such as response time and power consumption.

II. Further design and development of various microactuators on planar substrates using ferrofluid-assisted microbearing

Results from chapter 4 show great potential for further development of microactuators on planar substrates that utilize ferrofluid assisted levitation as a simple and efficient bearing mechanism. Integrated moving magnet microactuator in s lab-on-a-chip device is one of such applications that can greatly benefit from such technology.

III. Further development and characterization of rotary micromotors based on ferrofluid microbearing

The early demonstration of the developed rotary motor in chapter 5 confirms great potential for the use of such micromotors for minimally invasive medical procedures; however, as concluded in chapter 5, further development and optimization is needed to improve the performance of such micromotors. One important aspect that should be addressed in future works is the output torque measurement. There are various methods suggested in the literature based on back-emf

measurement [80] or dimensional analysis [81] that could be used to assess the level of torque available with the fabricated devices.

Bibliography

- [1] D. J. Bell, T. J. Lu, N. a Fleck, and S. M. Spearing, “MEMS actuators and sensors: observations on their performance and selection for purpose,” *Journal of Micromechanics Microengineering*, vol. 15, no. 7, pp. 153–164, Jul. 2005.
- [2] S. Kamisuki, M. Fujii, T. Takekoshi, C. Tezuka, and M. Atobe, “A high resolution, electrostatically-driven commercial inkjet head,” in *IEEE Micro Electro Mechanical Systems (MEMS 2000)*, 2000, pp. 793–798.
- [3] K. H. Gilchrist, D. E. Dausch, and S. Grego, “Electromechanical performance of piezoelectric scanning mirrors for medical endoscopy,” *Sensors and Actuators: A Physical*, vol. 178, pp. 193–201, 2012.
- [4] H. Fujita, “Studies of Micro Actuators in Japan,” in *IEEE Robotics and Automation*, 1989, pp. 1559–1564.
- [5] Y. B. Gianchandani, “Bent-beam electrothermal actuators-Part I: Single beam and cascaded devices,” *Journal of Microelectromechanical Systems*, vol. 10, no. 2, pp. 247–254, 2001.
- [6] J. E. Huber, N. A. Fleck, and M. F. Ashby, “The Selection of Mechanical Actuators Based on Performance Indices,” in *proceedings of Royal Society A*, vol. 453, pp. 2185– 2205, 1997.
- [7] H. J. Cho, C. H. Ahn, “magnetic microactuators: Techniques and Applications,” *MEMS/NEMS*, Springer, pp. 1631-1654, 2006.
- [8] R. E. Rosensweig, *Ferrohydrodynamics*. New York: Cambridge Univ. Press, 1985.
- [9] K. Raj, B. Moskowitz, and R. Casciari, “Advances in ferrofluid technology,” *Journal of Magnetism and Magnetic Materials.*, vol. 149, no. 1–2, pp. 174–180, 1995.
- [10] C. Alexiou, R. Schmid, R. Jurgons, C. Bergemann, W. Parak, and F. G. Arnold, “Trageted Tumor Therapy with Magnetic Drug Targeting: Therapeutic Efficacy of Ferrofluid Bound Mitoxantrone,” in *Ferrofluids: Magnetically Controllable Fluid and Their Application*, 2002, pp. 233–251.
- [11] Ferrotec Inc., “<https://www.ferrotec.com/products/ferrofluidic/>,” 2014.
- [12] R. Pérez-Castillejos, J. A. Plaza, J. Esteve, P. Losantos, M. C. Acero, and C. Cane, “The Use of Ferrofluids in Micromechanics,” *Sensors and Actuators A: Physical*, pp. 176–180, 2000.

- [13] J. J. Ahn, J.-G. Oh, and B. Choi, "A Novel Type of a Microfluidic System Using Ferrofluids for an Application of μ -TAS," *Microsystem Technologies*, vol. 10, no. 8–9, pp. 622–627, 2004.
- [14] A. Hatch, A. E. Kamholz, G. Holman, P. Yager, and K. F. Böhringer, "A Ferrofluidic Magnetic Micropump," *Journal of Microelectromechanical Systems*, vol. 10, no. 2, pp. 215–221, 2001.
- [15] W. Xiao and S. Hardt, "An Adaptive Liquid Microlens Driven by a Ferrofluidic Transducer," *Journal of Micromechanics Microengineering*, vol. 20, no. 5, 055032(8pp), 2010.
- [16] E. Kim, J. Oh, and B. Choi, "A study on the development of a continuous peristaltic micropump using magnetic fluids," *Sensors and Actuators A: Physical*, vol. 128, pp. 43–51, 2006.
- [17] N. Nguyen and M. Chai, "A Stepper Micropump for Ferrofluid Driven Microfluidic Systems," *Micro and nanosystems*, vol. 1, pp. 17–21, 2009.
- [18] W. Sim, J. Oh, and B. Choi, "Fabrication , Experiment of a Microactuator Using Magnetic Fluid for Micropump Application," *Microsystem Technologies*, vol. 12, no. 12, pp. 1085–1091, 2006.
- [19] A. Beyzavi and N. Nguyen, "One-Dimensional Actuation of a Ferrofluid Droplet by Planar Microcoils," vol. 42, 2009.
- [20] A. Beyzavi and N. Nguyen, "Programmable Two-dimensional Actuation of Ferrofluid Droplet Using Planar Microcoils," *Journal of Physics D: Applied Physics*, vol. 42, no. 1, 015018 (8pp), 2010.
- [21] J. Seo, H. Kim, D. Park, and H. Lee, "Microfluidic MEMS-Based Light Modulator Using Magnetic Fluid Suitable for Flat Panel Display Applications," *Journal of Microelectromechanical Systems*, vol. 14, no. 4, pp. 763–769, 2005.
- [22] N.-T. Nguyen, G. Zhu, Y.-C. Chua, V.-N. Phan, and S.-H. Tan, "Magnetowetting and Sliding motion of a Sessile Ferrofluid Droplet in the Presence of a Permanent Magnet," *Langmuir*, vol. 26, no. 15, pp. 12553–12559, 2010.
- [23] B. A. Malouin, M. J. Vogel, J. D. Olles, L. Cheng, and A. H. Hirska, "Electromagnetic Liquid Pistons for Capillarity-Based Pumping.," *Lab on a Chip*, vol. 11, no. 3, pp. 393–397, 2011.
- [24] H.-C. Cheng, S. Xu, Y. Liu, S. Levi, and S.-T. Wu, "Adaptive Mechanical-Wetting Lens Actuated by Ferrofluids," *Optics Communications.*, vol. 284, no. 8, pp. 2118–2121, 2011.

- [25] D. Brousseau, E. F. Borra, M. Rochette, and D. B. Landry, "Linearization of the Response of a 91-Actuator Magnetic Liquid Deformable Mirror.," *Optics Express*, vol. 18, no. 8, pp. 8239–50, 2010.
- [26] Q. Ramadan, V. Samper, D. Poenar, and C. Yu, "On-chip Micro-electromagnets for Magnetic-based Bio-Molecules Separation," *Journal of Magnetism and Magnetic Materials*, vol. 281, pp. 150–172, 2004.
- [27] H. Nguyen and J.-C. Chen, "Numerical Study of a Droplet Migration Induced by Combined Thermocapillary-Buoyancy Convection," *Physics of Fluids*, vol. 22, no. 12, pp. 122101–122109, 2010.
- [28] M. Barbic, J. J. Mock, A. P. Gray, and S. Schultz, "Electromagnetic micromotor for microfluidics applications," *Applied Physics Letters*, vol. 79, no. 9, pp. 1399-1401, 2001.
- [29] R. S. Fearing, "A Planar Milli-Robot System on an Air Bearing," *Robotics Research*, pp.570-581, 1994.
- [30] S. Hansen and H. H. Gatzen, *Design and Manufacturing of Active Microsystems*, Springer 2011.
- [31] T. Weisener, G. Vogeles, M. Widmann, C. Bark, and R. D. Scharft, "Development and fabrication of a rotary micropump and its industrial and medical applications," in *SPIE, Micromachined Devices and Components II*, pp. 218–225, 1996.
- [32] C. Ruffert, R. Gehrking, B. Ponick, and H. H. Gatzen, "Magnetic Levitation Assisted Guide for a Linear Micro-Actuator," in *IEEE International Magnetics conference*, vol. 42, no. 11, pp. 3785–3787, 2006.
- [33] S. D. Collins, A. P. Wallace, R. L. Smith, J. M. Sirota, and C. González "Microphotonics system implementation," in *10th International Conference on Solid-State Sensors Actuators and Microsystems*, 1999, pp. 124–127.
- [34] M. Fohse, H.-D. Stolting, J. Edler, and H. H. Gatzen, "A batch fabricated linear synchronous motor," in *International Mechanical Engineering Congress and Exhibition*, 2003, pp. 693–700.
- [35] L. G. Fréchette, S. A. Jacobson, K. S. Breuer, S. Member, F. F. Ehrich, R. Ghodssi, R. Khanna, C. W. Wong, X. Zhang, M. A. Schmidt, and A. H. Epstein, "High-Speed Microfabricated Silicon Turbomachinery and Fluid Film Bearings," *Journal of Microelectromechanical Systems*, vol. 14, no. 1, pp. 141–152, 2005.
- [36] C. W. Wong, X. Zhang, S. a. Jacobson, and a. H. Epstein, "A Self-Acting Gas Thrust Bearing for High-Speed Microrotors," *Journal of Microelectromechanical Systems*, vol. 13, no. 2, pp. 158–164, 2004.

- [37] M. L. Chan, B. Yoxall, H. Park, Z. Kang, I. Izyumin, J. Chou, M. M. Megens, M. C. Wu, B. E. Boser, and D. a. Horsley, "Design and characterization of MEMS micromotor supported on low friction liquid bearing," *Sensors and Actuators: A Phys.*, vol. 177, pp. 1–9, 2012.
- [38] R. Bandorf, H. Lüthje, C. Henke, J. Wiebe, J. H. Sick, and R. Küster, "Different carbon based thin films and their microtribological behavior in MEMS applications," *Surface Coatings Technology*, vol. 200, pp. 1777–1782, 2005.
- [39] R. Bandorf, H. Lüthje, K. Schiffmann, T. Staedler, and a. Wortmann, "Sub-micron coatings with low friction and wear for micro actuators," *Microsystem Technologies*, vol. 8, no. 1, pp. 51–54, 2002.
- [40] H. H. Gatzen, C. Morsbach, and A. Karyazin, "High precision machining of a longitudinal bearing for a linear microactuator," in *EUSPEN 3rd International Conference*, 2002, pp. 325–328.
- [41] M. Feldmann and S. Büttgenbach, "Linear Variable Reluctance (VR) Micro Motors With Compensated Attraction Force : Concept , Simulation , Fabrication and Test," *IEEE Transactions on Magnetics*, vol. 43, no. 6, pp. 2567–2569, 2007.
- [42] N. Ghalichechian, S. Member, and A. Modafe, "Design , Fabrication , and Characterization of a Rotary Micromotor Supported on Microball Bearings," *Journal of Microelectromechanical Systems*, vol. 17, no. 3, pp. 632–642, 2008.
- [43] C. Ruffert, J. Li, B. Denkena, and H. H. Gatzen, "Development and Evaluation of an Active Magnetic Guide for Microsystems With an Integrated Air Gap Measurement System," *IEEE Transactions on Magnetics*, vol. 43, no. 6, pp. 2716–2718, 2007.
- [44] S. Sudo and Y. Takaki, "Magnetic Fluid Devices for Driving Micro Machines," *JSME International Journal Series B-fluids and Thermal Engineering*, vol. 48, no. 3, pp. 464–470, 2005.
- [45] S. Sudo, D. Asano, H. Takana, and H. Nishiyama, "The dynamic behavior of magnetic fluid adsorbed to small permanent magnet in alternating magnetic field," *Journal of Magnetics and Magnetic Materials.*, vol. 323, no. 10, pp. 1314–1318, 2011.
- [46] S. Sudo, T. Goto, T. Yano, M. Futamura, H. Takana, and H. Nishiyama, "Micro Reciprocating Actuator Using Magnetic Fluid and Two Permanent Magnets," *Journal of Solid Mechanics and Material Engineering.*, vol. 6, no. 6, pp. 555–564, 2012.
- [47] M. S. M. Ali and K. Takahata, "Sensors and Actuators A : Physical Frequency-controlled wireless shape-memory-alloy microactuators integrated using an electroplating bonding process," *Sensors and Actuators: A Physical*, vol. 163, no. 1, pp. 363–372, 2010.

- [48] N. Ning, X. P. Li, J. Fan, W. C. Ng, Y. P. Xu, X. Qian, and H. L. Seet, "A tunable magnetic inductor," *IEEE Transactions on Magnetics*, vol. 42, no. 5, pp. 1585–1590, 2006.
- [49] S. Lee, S. Member, J. Kim, J. Kim, and Y. Kim, "Millimeter-Wave MEMS Tunable Low Pass Filter With Reconfigurable Series Inductors and Capacitive Shunt Switches," *IEEE Microwave and Wireless Components Letters*, vol. 15, no. 10, pp. 691–693, 2005.
- [50] Y. Yoshihara, H. Sugawara, H. Ito, K. Okada, and K. Masu, "A Wide Tuning Range CMOS VCO Using Variable Inductor," in *Silicon Monolithic Integrated Circuits in RF Systems*, pp. 278–281, 2004.
- [51] S. Zhou, X.-Q. Sun, and W. N. Carr, "A monolithic variable inductor network using microrelays with combined thermal and electrostatic actuation," *Journal of Micromechanics Microengineering*, vol. 9, no. 1, pp. 45–50, Mar. 1999.
- [52] P. Park, C. S. Kim, M. Y. Park, S. Do Kim, H. K. Yu, and S. Member, "Variable Inductance Multilayer Inductor With MOSFET Switch Control," *IEEE Electron Device Letters*, vol. 25, no. 3, pp. 144–146, 2004.
- [53] B. Andò, S. Baglio, and a. Beninato, "Behavior analysis of ferrofluidic gyroscope performances," *Sensors and Actuators: A Physical*, vol. 162, no. 2, pp. 348–354, 2010.
- [54] B. Andò, A. Ascia, S. Baglio, and N. Savalli, "A Novel Ferrofluidic Inclinator," *Instrumentation*, vol. 56, no. 4, pp. 1114–1123, 2007.
- [55] W. p. Shih, Z. Li, D. T. McCormick, N. C. Tien, and C. Y. Hui, "Tunable Solenoid Microinductors Utilizing Permalloy Electro-Thermal Vibromotors," in *IEEE MEMS Conference*, 2004, pp. 793–796.
- [56] D. Yun, M. Ellis, E. Home, J. B. Lee, H. Lu, R. Mansour, A. Nallani, and G. Skidmore, "Microassembled tunable mems inductor," in *18th IEEE International Conference on Micro Electro Mechanical Systems (MEMS 2005)*, pp. 183–186, 2005.
- [57] W. C. P. Technology, K. Okada, H. Sugawara, S. Member, and H. Ito, "On-Chip High Q Variable Inductor Using Wafer-Level Chip-Scale Package Technology," *IEEE Transactions on Electron Devices*, vol. 53, no. 9, pp. 2401–2406, 2006.
- [58] M. Kono, "Designing Variable Inductor with MEMS Technology," *IEEJ Intern. Analog VLSI Workshop*, 2005, pp. 1–6.
- [59] C.-M. Tasseti, G. Lissorgues, and J.-P. Gilles, "New tunable RF MEMS microinductors design," *Journal of Micromechanics and Microengineering*, vol. 14, no. 9, pp. 17–22, 2004.

- [60] S. Chang, S. Member, S. Sivoththaman, and S. Member, "A Tunable RF MEMS Inductor on Silicon Incorporating an Amorphous Silicon Bimorph in a Low-Temperature Process," *IEEE Electron Device Letters*, vol. 27, no. 11, pp. 905–907, 2006.
- [61] V. M. Lubecke, S. Member, B. Barber, E. Chan, D. Lopez, M. E. Gross, and P. Gammel, "Self-Assembling MEMS Variable and Fixed RF Inductors," *IEEE Transactions on Microwave Theory and Technology*, vol. 49, no. 11, pp. 2093–2098, 2001.
- [62] I. El Gmati, P. F. Calmon, A. Boukabache, P. Pons, R. Fulcrand, S. Pinon, H. Boussetta, M. A. Kallala, and K. Besbes, "Fabrication and evaluation of an on-chip liquid micro-variable inductor," *Journal of Micromechanics and Microengineering*, vol. 21, no. 2, p. 025018 (8pp), 2011.
- [63] M. a Eddings, M. a Johnson, and B. K. Gale, "Determining the optimal PDMS–PDMS bonding technique for microfluidic devices," *Journal of Micromechanics and Microengineering*, vol. 18, no. 6, p. 067001 (8pp), 2008.
- [64] A. Santra, N. Chakraborty, and R. Ganguly, "Analytical evaluation of magnetic field by planar micro-electromagnet spirals for MEMS applications," *Journal of Micromechanics and Microengineering*, vol. 19, no. 8, p. 085018 (8pp), 2009.
- [65] P. C. Fannin, C. N. Marin, I. Malaescu, and N. Stefu, "Microwave dielectric properties of magnetite colloidal particles in magnetic fluids," *Journal of Physics: Condensed Matter*, vol. 19, no. 3, p. 036104, 2007.
- [66] J. T. Cheung, "Transverse Mechanical Translator With Ferrofluid Support," US6917131 B2, 2005.
- [67] R. E. Rosensweig, "Buoyancy and stable levitation of a magnetic body immersed in a magnetizable fluid," *Nature*, vol. 210, pp. 613–614, 1966.
- [68] R. Ravaut, G. Lemarquand, and V. Lemarquand, "Mechanical properties of ferrofluid applications: Centering effects and capacity of a seal," *Tribology International*, vol. 43, pp. 76–82, 2010.
- [69] A. N. Shtetman, "Tomorrow ' s surgery : micromotors and microrobots for minimally invasive procedures," *Minimally invasive therapy and allied technologies*, vol. 7, pp. 343–352, 1998.
- [70] S. Member, "Design and Characterization of a Novel Hybrid Actuator Using Shape Memory Alloy and DC Micro-Motor for Minimally Invasive Surgery," *IEEE/ASME Transactions on Mechatronics*, pp. 1–10, 2007.
- [71] J. Shang, D. P. Noonan, C. Payne, J. Clark, M. H. Sodergren, and A. Darzi, "An Articulated Universal Joint Based Flexible Access Robot for Minimally Invasive

- Surgery,” in IEEE International Conference on Robotics Automation, vol. 1, pp. 1147–1152, 2011.
- [72] Z. Yan and I. Engineering, “Micro Motor Based A New Type of Endoscope,” in *20th Annual International Conference of the IEEE Engineering in Medicine and Biology Society*, 1998. vol. 20, no. 4, pp. 1822–1825.
- [73] J. Yang, R. Chen, C. Favazza, J. Yao, C. Li, Q. Zhou, K. K. Shung, and L. V Wang, “A 2 . 5-mm diameter probe for photoacoustic and ultrasonic endoscopy,” *Optics Express*, vol. 20, no. 21, pp. 1419–1421, 2012.
- [74] J.-M. Yang, C. Favazza, R. Chen, J. Yao, X. Cai, K. Maslov, Q. Zhou, K. K. Shung, and L. V Wang, “Simultaneous functional photoacoustic and ultrasonic endoscopy of internal organs in vivo.,” *Nature Medicine*, vol. 18, no. 8, pp. 1297–1302, 2012.
- [75] J. Yang, K. Maslov, H. Yang, Q. Zhou, K. K. Shung, and L. V Wang, “Photoacoustic endoscopy,” *Optics Letters*, vol. 34, no. 10, pp. 1591–1593, 2009.
- [76] S. Chang, E. Murdock, Y. Mao, C. Flueraru, and J. Disano, “Stationary-fiber rotary probe with unobstructed 360 ° view for optical coherence tomography,” *Optics Letters*, vol. 36, no. 22, pp. 4392–4394, 2011.
- [77] M. Mccarthy, C. M. Waits, and R. Ghodssi, “Dynamic Friction and Wear in a Planar-Contact Encapsulated Microball Bearing Using an Integrated Microturbine,” *Journal of Microelectromechanical Systems*, vol. 18, no. 2, pp. 263–273, 2009.
- [78] K. Takahata, and Y. B. Gianchandani, “Batch Mode Micro-Electro-Discharge Machining,” *IEEE/ASME Journal of Microelectromechanical Systems*, vol. 11, no. 2, pp. 102-110, 2002
- [79] J. Su, J. Zhang, L. Yu, and Z. Chen, “In vivo three-dimensional microelectromechanical endoscopic swept source optical coherence tomography,” *Optics Express*, vol. 15, no. 16, pp. 10390–10396, 2007.
- [80] P. A. Goemans, A. F. Kamerbeek, and E. M. Klijn, “Measurement of the pull-out torque of synchronous micromotors with PM rotor,” *Sixth International Conference on Electrical Machines and Drives*, 1993, pp. 8-10.
- [81] R. Jabłoński, M. Turkowski, and R. Szewczyk, “Determination of DC micro-motor characteristics by electrical measurements,” *Recent Advances in Mechatronics*, Springer Berlin Heidelberg, 2007, pp 278-282.

- [82] A. S. Ergun, Y. Huang, X. Zhuang, O. Oralkan, G. G. Yaralioglu, and B. T. Khuri-Yakub, "Capacitive Micromachined Ultrasonic Transducers: Fabrication Technology," *IEEE Transactions on Ultrasonic Ferroelectric Frequency Control*, vol. 52, no. 12, pp. 2242-2257, 2005
- [83] I. Shahosseini, E. Lefeuvre, E. Martincic, M. Woytasik, J. Moulin, S. Megherbi, R. Ravaud, and G. Lemarquand., "Microstructured Silicon Membrane with Soft Suspension Beams for a High Performance MEMS Microspeaker," *Microsystems Technology*, vol. 18, pp. 1791-1799, 2012.
- [84] L. Mele, F. Santagata, E. Iervolino, M. Mihailovic, T. Rossi, A. T. Tran, H. Schellevis, J. F. Creemer, and P. M. Sarro, "A Molybdenum MEMS Microhotplate for High-Temperature Operation," *Sensors and Actuators: A Physical*, vol. 188, pp. 173-180, 2012.
- [85] H. S. Lee, C. Cho, and S. P. Chang, "Robust Designed Capacitive Gas Pressure Sensor for Harsh Environment," in *Proceedings of IEEE Sensors*, Oct. 25-28, 2009, pp. 770-773.
- [86] Y. H. Zhang, C. Wang, W. X. Ouyang, and Z.-S. Lai, "Compound Sacrificial Layer Process for RF MEMS Applications," in *Proceedings of 3rd IEEE International Symposium Microwave, Antenna, Propagation EMC Tech. for Wireless Communications*, Oct. 27-29, 2009, pp. 485-487.
- [87] P. Ekkels, R. W. Tjerkstra, G. J. M. Krijnen, J. W. Berenschot, J. Brugger, and M. C. Elwenspoek, "Fabrication of Functional Structures on Thin Silicon Nitride Membranes," *Microelectronics Engineering*, vol. 67-68, pp. 422-429, 2003.
- [88] C. L. Dai, P. W. Lu, C. Chang, and C. Y. Liu, "Capacitive Micro Pressure Sensor Integrated with a Ring Oscillator Circuit on Chip," *Sensors*, vol. 9, no. 12, pp. 10158-10170, 2009.
- [89] H. San, H. Zhang, Q. Zhang, Y. Yu, and X. Chen, "Silicon-Glass-Based Single Piezoresistive Pressure Sensors for Harsh Environment Applications," *Journal of Micromechanics and Microengineering.*, vol. 23, 075020 (8pp), 2013.
- [90] A. R. Mohammadi, C. P. J. Bennington, and M. Chiao, "Development of a Combined Piezoresistive Pressure and Temperature Sensor Using a Chemical Protective Coating for Kraft Pulp Digester Process Monitoring," *Journal of Micromechanics and Microengineering.*, vol. 21, 015009 (10pp), 2011.
- [91] A. R. Mohammadi, T. C. M. Graham, C. P.J. Bennington, and M. Chiao, "Development of a Compensated Capacitive Pressure and Temperature Sensor Using Adhesive Bonding and Chemical-Resistant Coating for Multiphase Chemical Reactors," *Sensors and Actuators: A Physical*, vol. 163, no. 2, pp. 471-480, 2010.

- [92] C. Pang, Z. Zhao, L. Du, and Z. Fang, "Adhesive Bonding with SU-8 in a Vacuum for Capacitive Pressure Sensors," *Sensors and Actuators: A Physical*, vol. 147, pp. 672-676, 2008.
- [93] M. Wiemer, J. Chenping, M. Toepper, and K. Hauck, "Wafer Bonding with BCB and SU-8 for MEMS Packaging," in *Proc. of IEEE Electronics Systems. Integration Technology Conference (ESTC)*, vol.2, Sept. 5-7, 2006, pp.1401-1405.
- [94] D. Brox, A.R. Mohammadi, and K. Takahata, "Non-Lithographically Microfabricated Capacitive Pressure Sensor for Biomedical Applications," *IET Electronics Letters*, vol. 47, no.18, pp. 1015-1017, 2011.
- [94] J. Charmet, O. Banakh, E. Laux, B. Graf, F. Dias, A. Dunand, H. Keppner, G. Gorodyska, M. Textor, W. Noell, N.F. de Rooij, A. Neels, M. Dadras, A. Dommann, H. Knapp, Ch. Borter, and M. Benkhaira, "Solid on Liquid Deposition," *Thin Solid Films*, vol. 518, pp. 5061-5065, 2010.
- [95] C. P. Tan, and H. G. Craighead, "Surface Engineering and Patterning Using Parylene for Biological Applications," *Materials*, vol. 3, pp. 1803-1832, 2010.
- [96] S. Takamatsu, H. Takano, N. Binh-Khiem, T. Takahata, E. Iwase, K. Matsumoto, and I. Shimoyama, "Liquid-Phase Packaging of a Glucose Oxidase Solution with Parylene Direct Encapsulation and an Ultraviolet Curing Adhesive Cover for Glucose Sensors," *Sensors*, vol. 10, no. 6, pp. 5888-5898, 2010.
- [97] B.-K. Nguyen, E. Iwase, K. Matsumoto, and I. Shimoyama, "Electrically Driven Varifocal Micro Lens Fabricated by Depositing Parylene Directly on Liquid," in *Proceedings of IEEE 20th Int. Conference on Micro Electro Mechanical Systems (MEMS)*, Jan. 21-25, 2007, pp. 305-308.
- [98] M. Sadeghi, K. Hanseup, and K. Najafi, "Electrostatically Driven Micro-Hydraulic Actuator Arrays," in *Proceedings of IEEE 23rd Int Conference on Micro Electro Mechanical Systems (MEMS)*, Jan. 24-28, 2010), pp. 15-18.
- [99] G. Blazquez, P. Pons, and A. Boukabache, "Capabilities and Limits of Silicon Pressure Sensors," *Sensors and Actuators A: Physical*, vol. 17, no. 3, pp. 387-403, 1989.
- [100] W. H. Ko, and Q. Wang, "Touch Mode Capacitive Pressure Sensors," *Sensors and Actuators A: Physical*, vol. 75, no. 3, pp. 242-251, 1999.
- [101] A. Ettouhami, Z. Nouredine, and M. Elbelkacemi, "A Novel Capacitive Pressure Sensor Structure with High Sensitivity and Quasi-Linear Response," *Comptes Rendus Mecanique*, vol. 332, no. 2, pp. 141-146, 2004.

[102] J. J. Licari, Coating Materials for Electronic Applications, *William Andrew Publishing*, New York, USA, 2003.

Appendices

Finally, besides the studies presented in this dissertation I contributed in the papers listed below which were for other projects not directly related to my thesis.

Other publications:

1. M.S. Mohamed Ali, B. Bycraft, C. Schlosser, **B. Assadsangabi**, and K. Takahata, "Out-of-Plane Spiral-Coil Inductor Self-Assembled by Locally Controlled Bimorph Actuation," *Micro & Nano Letters*, vol. 6, no. 12, pp. 1016-1018, 2011.
2. X. Chen, L. Song, **B. Assadsangabi**, J. Fang, M.S. Mohamed Ali, and K. Takahata, "Wirelessly Addressable Heater Array for Centrifugal Microfluidics and Escherichia Coli Sterilization," *35th IEEE Int'l Conf. Engineering in Medicine and Biology Society (EMBS 2013)*, Osaka, Japan, July 2013, pp. 5505-5508.
3. H. Najar, **B. Assadsangabi**, M. Dahmardeh M., E. Cretu, "Combined FEA-Matlab optimization of Capacitive Micromachined Ultrasound Transducer Cell," *2010 ASME International Mechanical Engineering Congress & Exposition*, Vancouver, Canada, November 2010, pp. 229-235.
4. X. Chen, D. Brox, **B. Assadsangabi**, Y. Hsiang, K. Takahata, "Intelligent Telemetric Stent for Wireless Monitoring of Intravascular Pressure and its In Vivo Testing," *Biomedical Microdevices*, 2014, DOI: 10.1007/s10544-014-9879-8 (15pp).

Appendix A Ferrofluid Sacrificial Microfabrication of Capacitive Pressure

Sensors⁵

In this section, use of ferrofluid as a liquid sacrificial layer for creating suspended membrane for capacitive pressure sensors is demonstrated.

A.1 Introduction

Suspended or movable membranes are utilized in a variety of micro-electro-mechanical systems (MEMS) including micro sensors and actuators [82]-[84]. The microfabrication of these movable microstructures relies on the use of sacrificial etching in most cases. Sacrificial layers are typically thin films of selected materials, including polymers [85], [86], dielectrics [87], and metals [88], which are etched away using suitable chemicals once mechanical structures are established on top of the layers. The formation and removal of sacrificial layers requires several process steps, including time-consuming thermal processes. During sacrificial etching, the etchant may attack other structures. Moreover, photolithographic steps are often required to achieve targeted geometries of the structures, further complicating the process. Direct bonding of movable structures using anodic bonding [89], [90], UV-curable epoxy [91], and thermal bonding of polymers such as SU-8 [92], benzocyclobutene [93], and Parylene-C [94] has also been utilized to create suspended structures. However, the need for high temperatures, integrity of sealing, repeatability, etc. remain practical issues in this approach. “Solid On Liquid Deposition” [95] is an interesting technique that allows deposition of Parylene-C, a biocompatible polymer [96], over surfaces of different types of liquids. In this method, the

⁵ Part of this chapter appeared in the following publications:

1. B. Assadsangabi, X. Chen, D. Brox, K. Takahata, "Microfabrication of Capacitive Pressure Sensors using Ferrofluid Sacrificial Layers," IEEE Sensors, Baltimore, USA, 2013, in press.

Parylene is deposited over liquid surfaces under vacuum conditions, enabling perfect encapsulation of liquids; this technique has been utilized for various applications such as glucose sensor [97], varifocal microliquid lens [98], and micro-hydraulic actuator [99], in which encapsulated liquid components are used as part of functional device structures that allow the operation of the devices. This approach, thin-film deposition on liquid, could also be directed to the formation of suspended structures, by using a liquid component as a sacrificial layer for the structure formation after which the liquid layer is removed.

The present study investigates the use of ferrofluid as a liquid-phase sacrificial layer for suspended diaphragm formation and demonstrates its application to the microfabrication of a capacitive pressure sensor (Figure A.1). In this study, unique features of ferrofluid are exploited to enable sacrificial formation of suspended membranes over micromachined cavities that define the patterns of the ferrofluid sacrificial layer as it is filled in the cavities. This novel approach achieved through the use of ferrofluid contributes to significant simplification in the

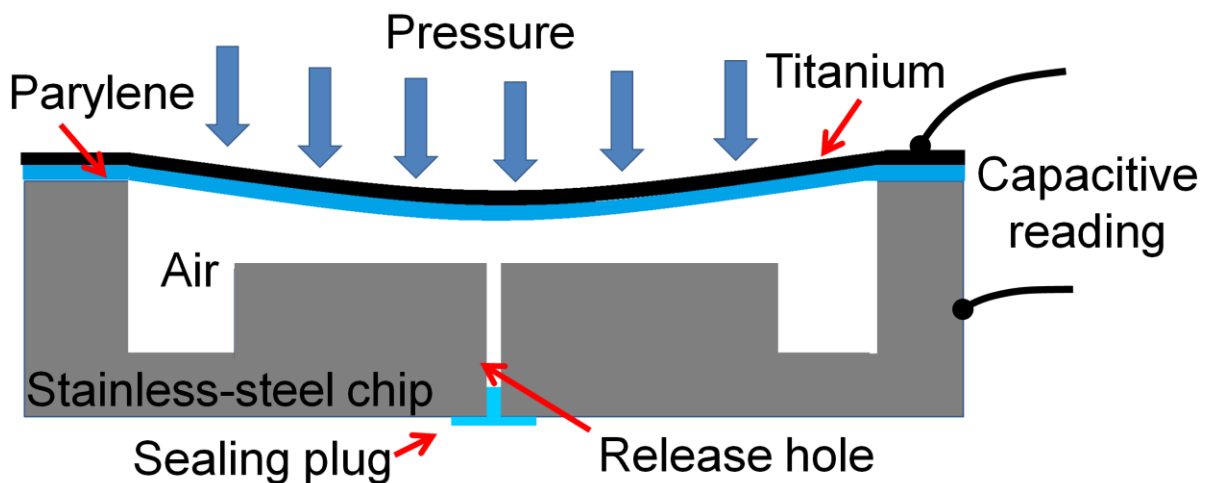


Figure A.1: A cross-sectional schematic of the capacitive pressure sensor.

simplification in the fabrication of MEMS membranes and related devices, as the method does not need to use any photolithographic, bonding, or chemical process. Temperature of the samples under the fabrication is maintained at or close to room temperature during the entire process. Furthermore, it allows one to utilize all biocompatible materials for the device construction, an essential requirement for biomedical and *in-vivo* applications of the sensor.

A.2 Design and Fabrication

The pressure sensor developed in this effort consists of a stainless-steel substrate chip with a $1 \times 1\text{-mm}^2$ cavity, capped by a $3\text{-}\mu\text{m}$ -thick membrane of Parylene-C that seals the cavity at atmospheric pressure (Figure A.1). The layer of titanium formed on the membrane and the bottom surface of the steel cavity serve as the parallel-plate electrodes of the sensing capacitor. The different cavity depths, $10\ \mu\text{m}$ and $30\ \mu\text{m}$, are selected for device characterization. Micro-electro-discharge machining (μEDM) is used to create the cavity in a $200\text{-}\mu\text{m}$ -thick stainless-steel plate, as well as to cut the chip component out of the plate (Step 1 in Figure A.3). (The particular stainless steel used in this study was type 304 that is not biocompatible; however, this can be easily replaced with medical-grade stainless steels such as type 316L as necessary.) In order to increase the cavity volume and hence membrane deflections [94], four dead-ended holes with $300\text{-}\mu\text{m}$ diameter and $70\text{-}\mu\text{m}$ depth are created within the cavity using μEDM . Similarly, a $300\text{-}\mu\text{m}$ -diameter through hole is drilled in the cavity to be used for the removal of sacrificial ferrofluid from the cavity after membrane formation. Figure A.2(a) shows the top view of a μEDM ed chip of stainless-steel substrate. A surface profile of the substrate that was μEDM ed to have a $30\text{-}\mu\text{m}$ -deep cavity is displayed in Figure A.2(b), indicating that the depth of the cavity was well controlled. Before filling the cavity with ferrofluid, the release hole is sealed using

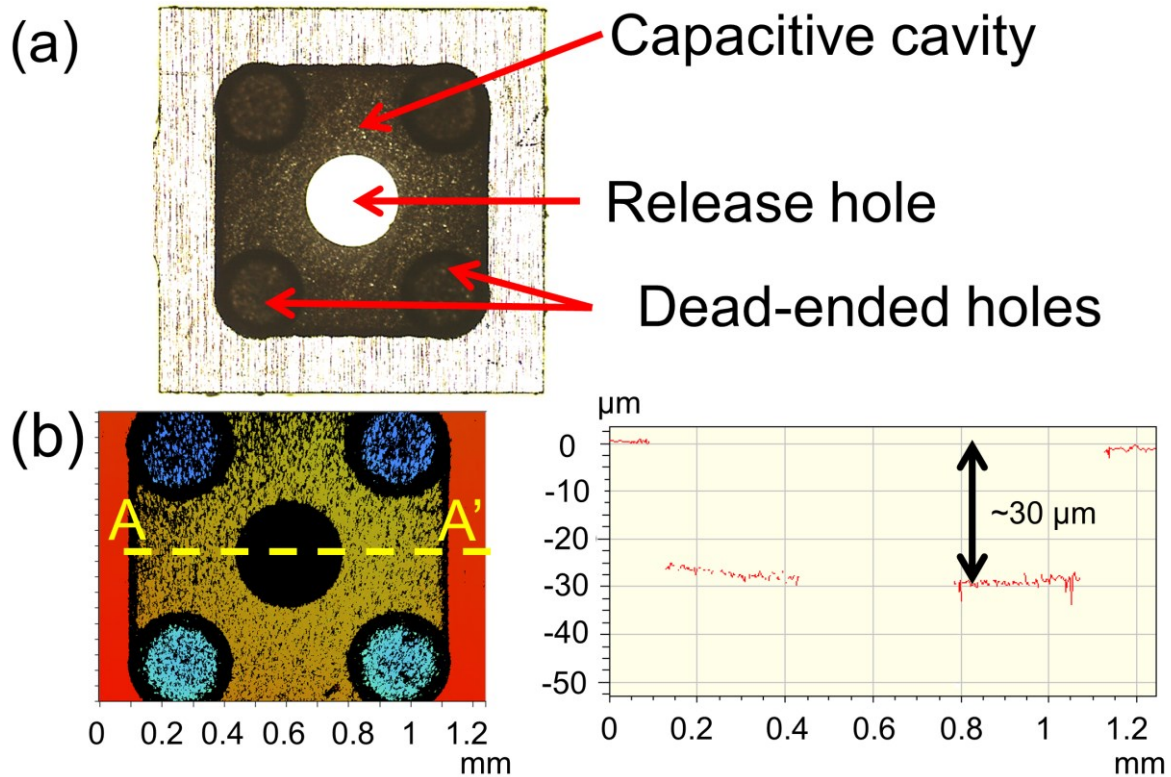


Figure A.2: (a) Optical image of the stainless-steel sensor substrate patterned using μ EDM, and (b) 2-dimensional surface profile of the machined substrate with the 30- μ m-deep cavity (left) and the depth profile along the A-A' line (right) measured using an optical profilometer (Wyko NT1100, Veeco, NY, USA).

epoxy on the bottom of the steel chip (Step 2 in Fig. 3). In addition, the surfaces of the chip are modified using an adhesion promoter (A-174 silane, Specialty Coating Systems, Inc., IN, USA) for Parylene-C deposition.

Ferrofluid is then filled in the cavity (Step 2 in Fig. A.3). One key feature for ferrofluid to be able to serve as the sacrificial layer for vapor-phase Parylene deposition is its vapor pressure, which must be sufficiently lower than the vacuum pressure involved in the Parylene deposition

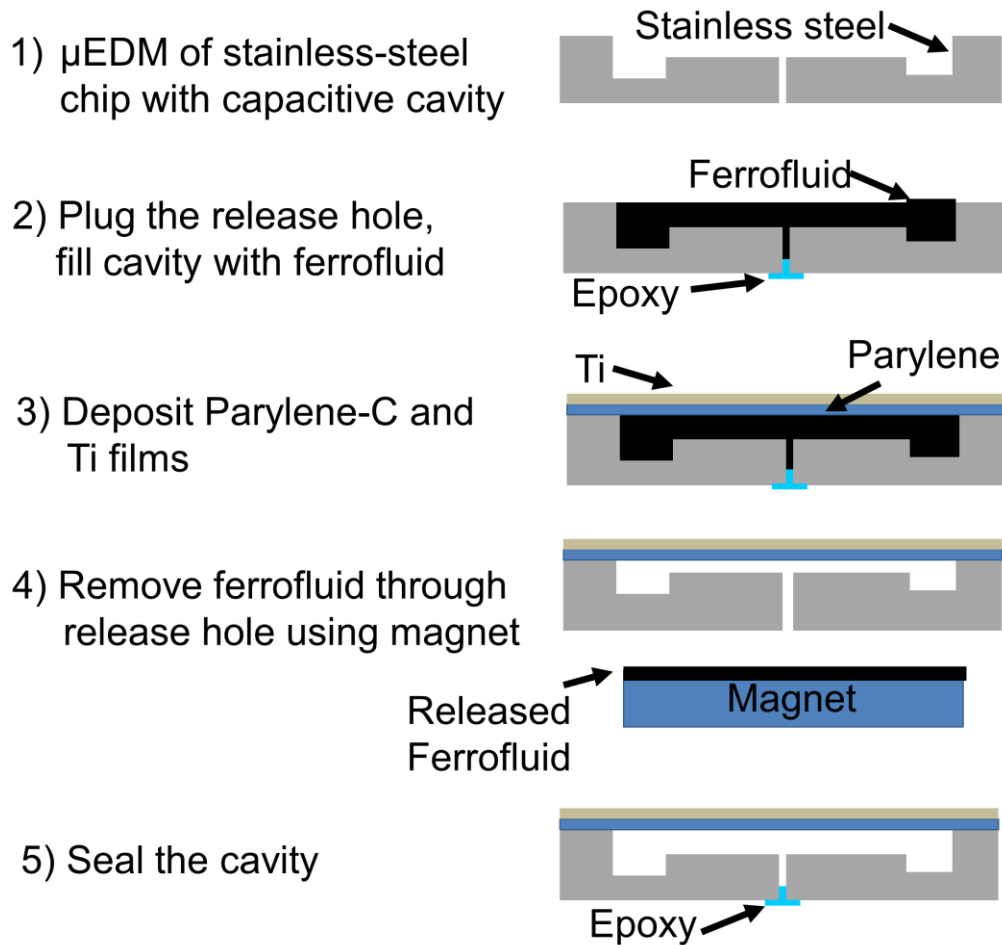


Figure A.3: Fabrication process flow.

process (performed with pressures of ~ 1.3 Pa at room temperature). This ensures that the vaporization of the fluid is negligible during the process. For this purpose, a commercially available ferrofluid (A-300, Sigma-Hi Chemical Inc., Japan) based on alkylnaphthalene that exhibits a vapor pressure of $<10^{-7}$ Pa (at room temperature) was utilized in this study. This oil-based ferrofluid was observed to be highly stable in the vacuum environment of Parylene-C deposition (Step 3 in Figure A.3). It is worth noting that this particular selection also allows one to observe a device with the ferrofluid injected into its cavity directly through scanning electron

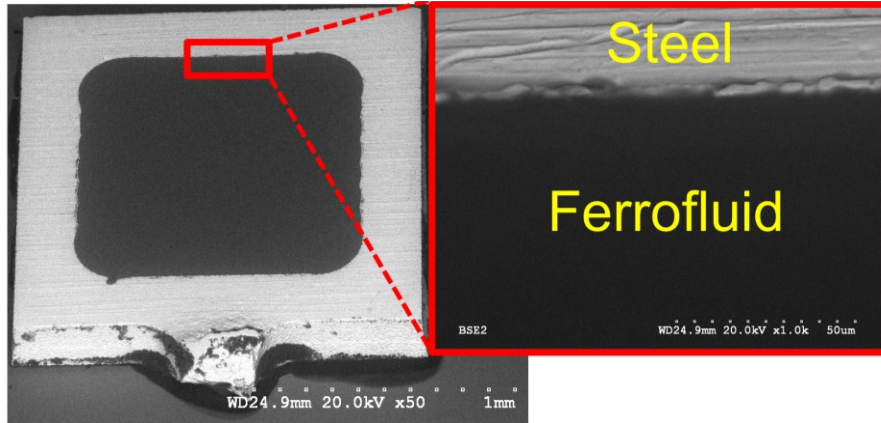


Figure A.4: SEM images of a sensor cavity filled with the ferrofluid A-300 acquired using Hitachi S3000N VP-SEM with its variable pressure mode (at 50 Pa).

microscopy (SEM) with an adjusted vacuum level (Figure A.4). Figure A.5(a) shows the device after conformal coating of Parylene-C with 3- μm thickness over all surfaces of the device including that of the ferrofluid filled in the 30- μm -deep cavity. After the Parylene coating step, a 50-nm-thick titanium layer is deposited on top of the Parylene using electron-beam evaporation, forming the upper capacitive electrode (Step 3 in Figure A.3 and Figure A.5(b)).

The surface profile of the Parylene-titanium membrane before ferrofluid removal (i.e., the device with the 30- μm -deep cavity shown in Figure A.5(b)) was characterized using the Wyko optical profilometer (Figure A.5(c)). It can be seen that the membrane had a curved concave profile. This profile pattern was likely dictated by the shape of underlying ferrofluid layer that had a slight meniscus pattern due to surface tensions acting on the ferrofluid at the edges of the cavity. The flatness of deposited membrane may be improved by precise control of the amount of ferrofluid (possibly using a syringe pump) injected into the cavity. It can also be seen that the membrane had high surface smoothness (with an average roughness, R_a , of ~ 15 nm) compared with the top surface of the cavity's periphery ($R_a \sim 330$ nm) whose roughness was attributed to

that of the steel substrate itself (as also observable in the close-up SEM image shown in Figure A.5(b)). After the membrane formation, the epoxy plug on the bottom of the release hole is removed, and then the ferrofluid is extracted out of the cavity through the hole by placing the sensor chip on a permanent magnet that attracts the fluid due to a field gradient established by

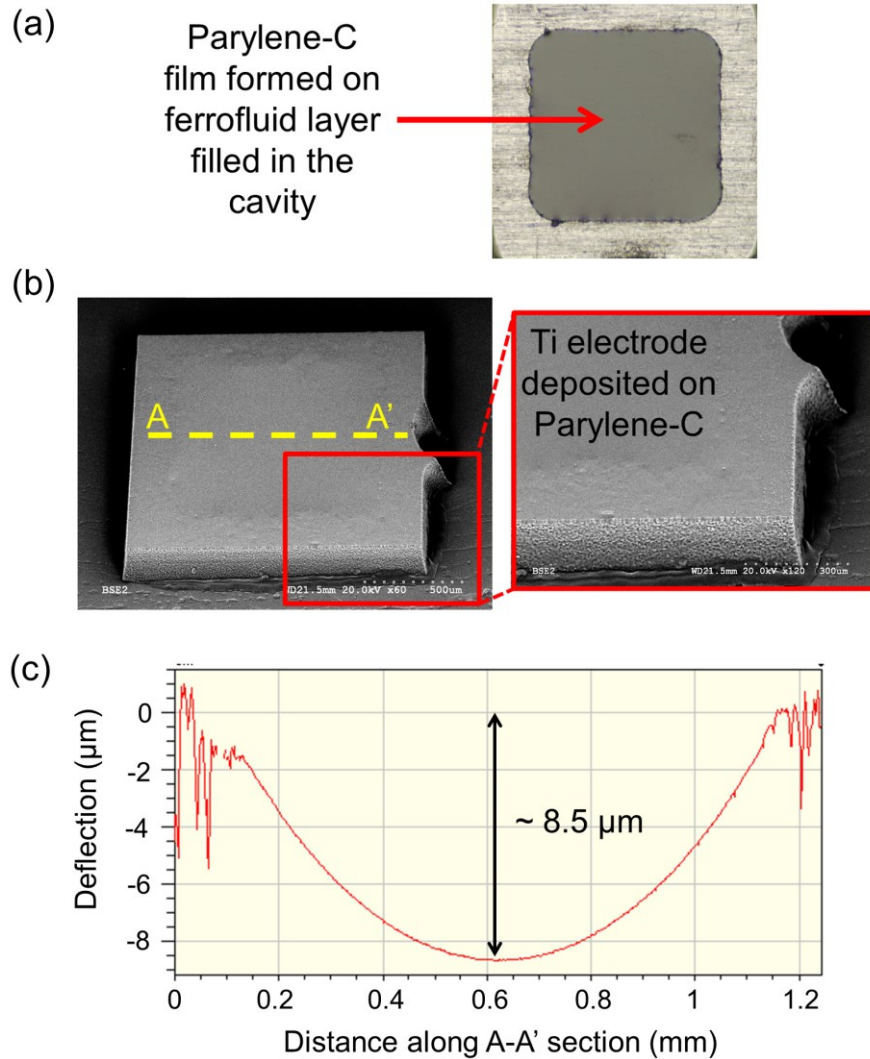


Figure A.5: (a) Optical image of the device after coating Parylene-C on top of the ferrofluid filled in the cavity of the stainless-steel chip, (b) SEM images of the device after depositing titanium electrode on the Parylene-C film, and (c) membrane profile before ferrofluid removal measured along A-A' line shown in (b).

the magnet (Step 4 in Figure A.3). Finally, the release hole is sealed again using the same epoxy (Step 5 in Figure A.3), completing the sensor fabrication (Figure A.6).

Figure A.7(a) shows a surface profile of the membrane after ferrofluid removal measured on a device with the 10- μm -deep cavity. The profile indicates a difference (of $\sim 5\text{-}\mu\text{m}$ in this particular case) between the level of the membrane and that of the top surface of the substrate, while showing a relatively uniform profile (with variations of only 1-2 μm) within the membrane at



Figure A.6: A completed sensor chip placed on a Canadian penny

its lowered level. A profile of the suspended membrane measured on the device with the 30- μm -deep cavity is also shown in Figure A.7(b) for comparison, indicating a curved concave shape, similar to the one prior to the release (Figure A.5(c)) with an increased deflection ($\sim 15\text{ }\mu\text{m}$ vs. $\sim 8.5\text{ }\mu\text{m}$ before the release). Both lowering and increased deflection of the released membranes are presumed to be caused by the presence of residual ferrofluid left within the cavities, i.e., the fluid that made contact with the backside of the membrane pulled it down

toward the cavity surface due to surface tensions of the fluid. For the 30- μm cavity case, the fluid might have accumulated around the central region of the membrane which was the closest to the cavity surface (as seen in Figure A.5(c)), pulling the region down further. In case of the 10- μm

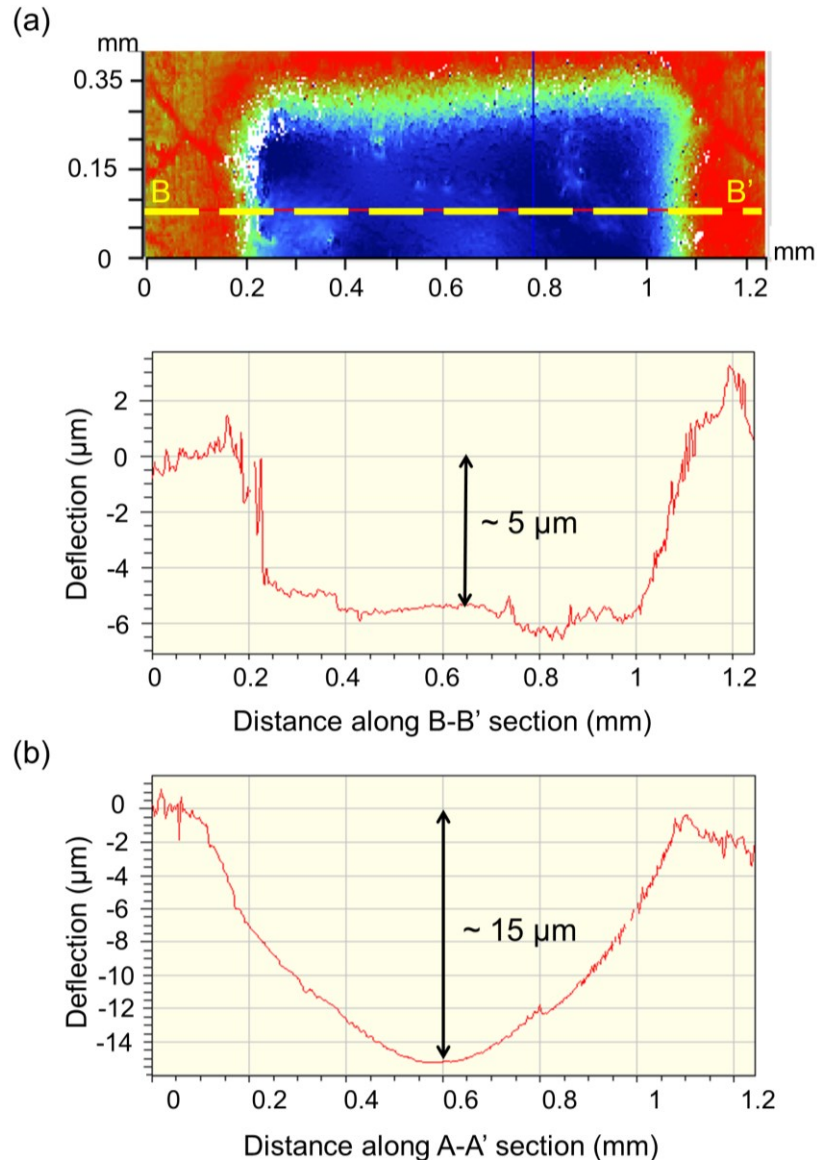


Figure A.7: Optical profilometer measurement results: (a) 2-dimensional surface profile (top) and the depth profile along the B-B' line (bottom) measured on the released membrane created with a 10- μm -deep cavity sensor, and (b) a measured depth profile of the released membrane created with a 30- μm -deep cavity sensor (Fig. A.5).

cavity case, due to its narrower gap, the fluid might have been present around peripheral regions of the cavity as well, pulling down the membrane more uniformly than the 30- μm cavity case. The presence of small amount of ferrofluid was verified by physical removal of the membranes after release and visual observation of the cavities and the backside of the membranes. Various factors such as surface roughness of the cavity, interfacial forces acting between ferrofluid and surfaces of the cavity/membrane, and certain magnetization of the stainless-steel substrate could contribute to incomplete removal of the ferrofluid, which require further analysis and optimization. Nevertheless, given the cavity's depths of 10 μm and 30 μm for the cases in Figure A.7(a) and 7(b), respectively, the measurement results evidently confirm that membranes were suspended after their release in both cases

A.3 Experimental Results

The experimental set-up used to characterize the fabricated sensors is schematically illustrated in Fig. 8. The electrical connection to the sensor chip was made by bonding a lead to the titanium

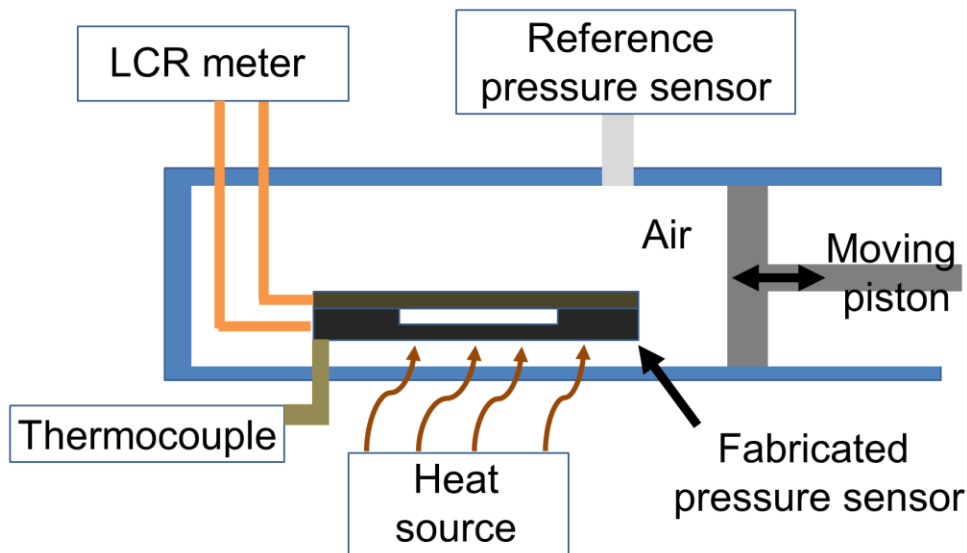


Figure A.8: Experimental set-up used to characterize the fabricated sensors.

surface on the sensor and silver pasting another lead to the stainless-steel body of the sensor. The capacitance between the two leads was measured using a precision LCR meter (HP 4275A). The ambient pressure of the sensor was varied by enclosing it in a custom chamber whose internal pressure was controlled while reading the reference pressure meter (PX-26, Omega Engineering Inc., QC, Canada) coupled with the chamber.

The responses of fabricated sensors placed in the above set-up were characterized for a pressure range up to 32 KPa at room temperature and the measurements were repeated two times for each device. The measurement results plotted in Figure A.9 indicate that the devices exhibited capacitive sensitivities of 766 ppm/KPa and 337 ppm/KPa (corresponding to the responses of 12.4 fF/KPa and 4.6 fF/KPa) for 10- and 30- μm -deep cavities, respectively, both with high linearity. The higher sensitivity with the 10- μm -cavity sensor is a reasonable outcome as the rate

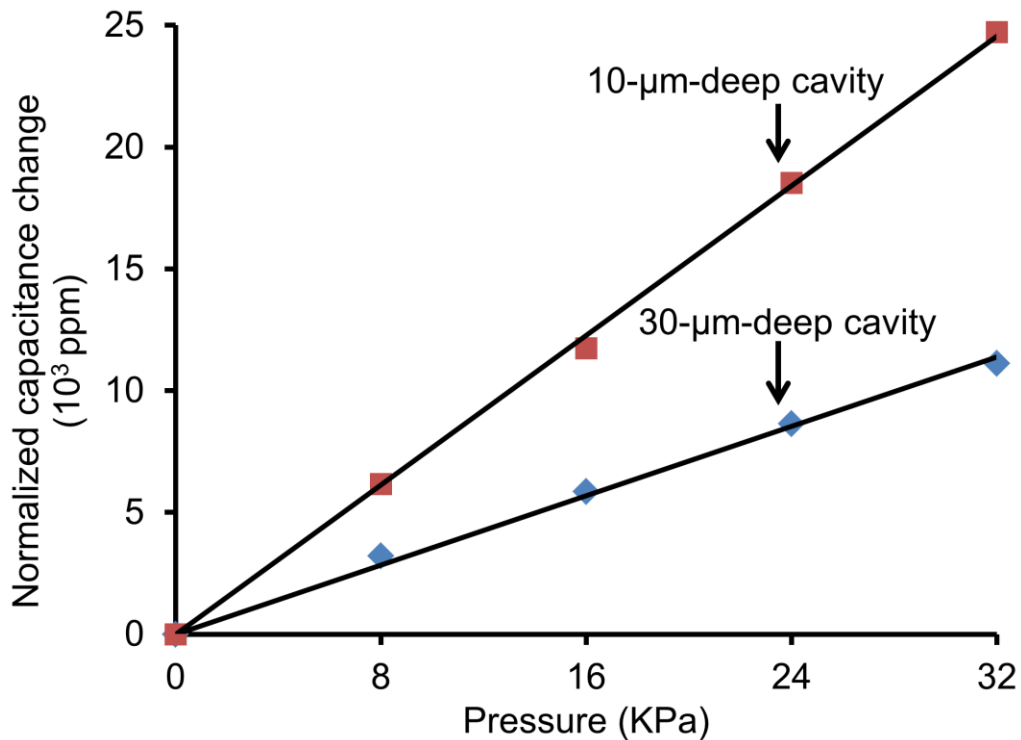


Figure A.9: Measured capacitive response of the fabricated sensors to applied pressure at room temperature

of capacitive change due to given changes in the gap is greater when the original gap is narrower. Capacitive pressure sensors exhibit generally nonlinear responses; however, those operated in the touch mode [100], [101] or with bossed diaphragms [102] are known to provide more linear responses. One possible reason of linear responses seen in the fabricated sensors might be related to the former condition, in which the membranes might have been indirectly touching the substrate through residual ferrofluid as discussed in Section II, potentially leading to the observed linear responses.

The temperature dependence of the sensor's base capacitance was also characterized by heating up the chamber as illustrated in Figure A.8 and repeating the measurements two times. During this measurement, the chamber was opened to atmosphere pressure in order to eliminate any pressure increase in it due to heating. Temperature of the sensor substrate was monitored using a thermocouple (HH802U, Omega, CT, USA). The measurement result is shown in Figure A.10,

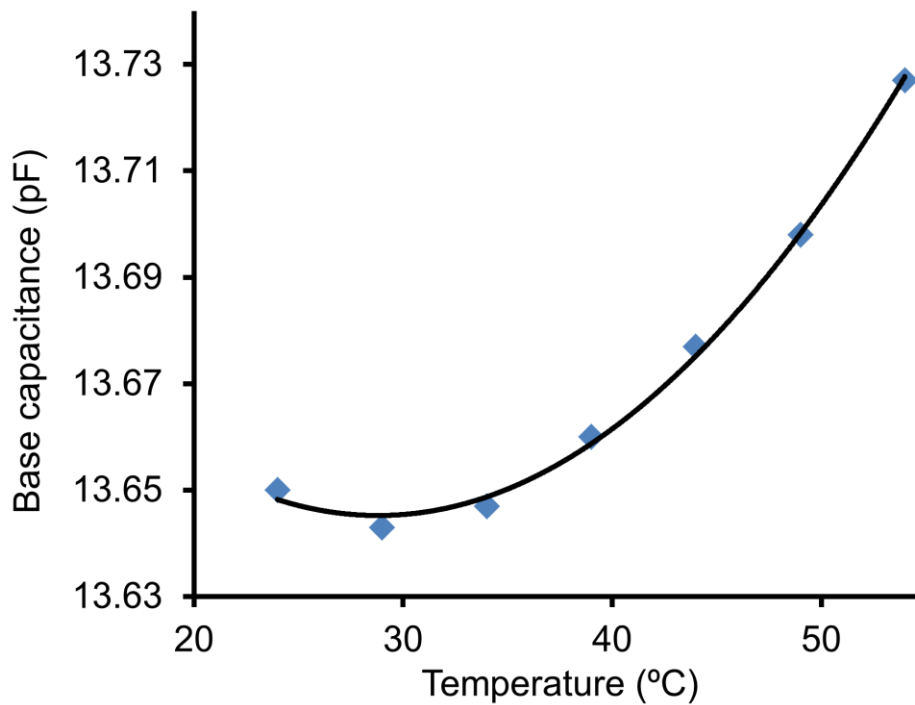


Figure A.10: Measured base capacitance of the developed sensor vs. ambient temperature.

indicates that the capacitance initially decreased with a small amount during heating up to ~ 29 °C and then started to rise, leading to steady increases until the maximum temperature tested (53 °C). The temperature coefficient of the capacitance is measured to be ~ 150 ppm/°C or less up to ~ 40 °C, and this coefficient increases to 330 ppm/°C on average beyond this temperature level. The initial decrease of the capacitance may be due to an increase of internal pressure in the capacitive cavity that can push the membrane up, resulting in a decrease of the capacitance. Although the exact source of the subsequent rise of capacitance is unclear, one possibility might be related to a temperature dependence of the permittivity of Parylene-C, which exhibits substantial increase with temperature (~ 4400 ppm/°C [103]). The impact of this potential source may be reduced using other types of Parylene that have dielectric constants with less thermal sensitivity (e.g. Parylene-N, with a 4× smaller coefficient [103]).

A.4 Conclusion

A novel microfabrication method that uses liquid-phase sacrificial layers based on ferrofluid and its application to a capacitive pressure sensor have been studied. The ferrofluid sacrificial layers were established in micromachined stainless-steel cavities to create Parylene-C membranes, which were successfully released and suspended by removing the fluid magnetically. The fabricated sensors were tested to exhibit highly linear responses with the maximum sensitivity of 766 ppm/KPa up to 32 KPa. The temperature dependence of the sensor's base capacitance was also characterized experimentally. The fabrication approach developed permits a capacitive pressure sensor to be constructed with all biocompatible materials, without needing any optical, chemical, or thermal step throughout the entire fabrication process. The process is not only simple but also potentially batch compatible with the use of a parallel μ EDM technique [80] for low-cost implementations. The results encourage further development and optimizations,

including those for ferrofluid injection and removal processes, toward achieving higher precision and integrity in the process. The developed method could be applied to the production of a variety of micro-scale capacitive and other transducers beyond the pressure sensor investigated in this study.